Redox poly(ferrocénylsilanes) et développement de (bio)interfaces : synthèse et applications

Tibor Halmagyi

Redox active poly(ferrocenylsilane)s for the development of (bio)interfaces: Synthesis and applications

Tibor Gergő Halmágyi

PhD Thesis

Université de Pau et des Pays de l'Adour

Supervisors:

Prof. Corinne Nardin

Prof. G. Julius Vancso

2023

Contents

1. General Introduction

1.1. Introduction

Poly(ferrocenylsilanes) (PFSs) consist of a main chain made of alternating ferrocene and silane units, generally obtained via the ring-opening polymerization of ferrocenophane precursors[1,2]. The ferrocene gives the polymer redox-active properties, whereas the side-chains of the silane unit can be modified in post-polymerization procedures, giving great versatility to this polymer family[3,4]. This versatility has made it possible to utilize PFS-based systems in (electro)catalysis[5–7], sensing[8,9], biomimetic[10,11] and antimicrobial[12] applications among other uses[11,13].

The structural and chemical properties of this family of polymers are wide-ranging and depend largely on the post-polymerization modification of side-chains attached to Si. PFSs can be deposited on substrates as thin films via physicochemical[14] or electrochemical[15] methods. PFS-containing hydrogels can also be formed[12,16] and used as stimulus-responsive materials for the synthesis and stabilization of metal nanoparticles (MNPs) in a phenomenon referred to as 'nanoparticle foundry'[7,12,17]. PFSs rendered water-soluble through the introduction of ionic groups into the structure can also exhibit the aforementioned 'nanoparticle foundry' property and electrosterically stabilize thus-formed colloidal nanoparticles[8]. By the introduction of azide groups, click reactions also become accessible to enable easy coupling of PFSs to other moieties[18]. We describe in this present work how we utilized this great variety of achievable structural properties through precise modification of the polymer structure to achieve various PFS-based systems for applications in sensing and biocorrosion.

Since there is an urgent need to propose alternatives to laboratory-based detection methods to monitor pollution and diagnose diseases, PFSs were considered in this thesis work as the

underlying building blocks of sensors and biosensors. Previous literature details the electrografting of PFSs to electrode surfaces[15]. We utilized this and the redox activity of ferrocene centres to create composite PFS-coated electrodes decorated with MNPs for sensing applications. By tuning the structural and chemical properties of PFSs, it also becomes possible to graft biomolecules to the polymer, enabling the construction of biosensors.

Microbially influenced corrosion (MIC) can be combatted by polymeric and redox-active materials such as chitosan-based films[19–22]. The protective layers can inhibit the growth of biofilms on the underlying surface through either bactericidal property[19,22], structural incompatibility with the bacterial colonies[23] or by forming a conductive polymer barrier between the bacteria and the metal[24,25]. We explored the use of PFSs with non-ionic side-chains for similar applications through the physicochemical deposition of PFS films on metal surfaces.

1.2. Summary of this thesis

The present work deals with the use of poly(ferrocenylsilanes) (PFSs), a class of redox-active metal-organic polymers, to develop functional biointerfaces for various applications. We expand upon various topics centered around the materials chemistry and applications of poly(ferrocenylsilane) based systems. The following topics will be presented in this thesis.

Chapter 2 summarizes prior art in the fields of materials chemistry of stimulus-responsive polymers, colloidal stability and stabilization, and biocorrosion protection, especially utilizing redox-responsive materials and polymers. We also provide detailed descriptions on how the research described in this thesis ties into existing literature.

In **Chapter 3**, colloid aptasensors (biochemical sensors utilizing aptamers as the sensing element) were considered as promising alternatives to chromatographic methods for the analysis of pollutants and biomarkers. Aptamers are short oligonucleotide sequences with

specific selectivity toward a given target molecule[26]. Aptasensors combine these aptamers with a transducer element, in our case gold nanoparticles, to enable colorimetric and particle size-based measurement[27–29]. The combination of PFS electrosteric stabilization and redox activity enabled the development of a model PFS-stabilized gold nanoparticle (AuNP) aptasensor. Synthesis and characterization of gold nanoparticles stabilized by an anionic PFS polyelectrolyte, denoted as PFS-AuNP, and subsequent functional grafting of anti-thrombin aptamers on the PFS-AuNPs was carried out, yielding an aptasensor denoted as aptamer-AuNP. Characterization of aptamer-AuNPs has shown that these nanoparticles exhibit excellent colloidal stability and redox sensitivity. We followed the thrombin-induced aggregation of aptamer-AuNPs with dynamic light scattering (DLS), and we found that the aptamers remain functional after grafting, creating a selective and sensitive thrombin sensor.

In **Chapter 4**, we summarize our investigations on the feasibility of using PFSs as stabilizing agents for colloidal systems. The redox responsiveness and the ability of PFS to electrosterically stabilize colloidal particles were investigated through its adsorption on latexes to sense antioxidants. Amidine latex (AL) nanoparticles carrying a positive surface charge were treated with an anionic polyelectrolyte poly(ferrocenylsilane), denoted as PFS^- to yield a negatively charged PFS-AL nanoparticle. The PFS-AL shows almost an order of magnitude higher stability in high ionic strength media than the bare AL, exhibiting the electrosteric stabilizing effect characteristic of PFS polyelectrolytes.

In **Chapter 5**, we describe our investigations on AuNP-PFS-gold electrode synthesis and application in electrochemical detection of antioxidants. Electrografted PFS layers at gold electrode surfaces were decorated with gold nanoparticles and the resulting composite electrodes were used to develop an electrochemical sensor for ascorbic acid. We successfully grafted PFSs on gold foil and gold-silicon substrates and characterized their electrochemical

properties and morphology. The deposition of gold nanoparticles on the redox-active polymer layer was carried out to further enhance the electrochemical activity of the samples. Electrochemical sensing of ascorbic acid with these electrodes was performed, and it was found that all samples significantly outperform the bare gold and gold-silicon electrodes, showing the utility of these redox-active polymers in electrochemical sensing.

Chapter 6 details our work on applying the redox activity of PFS coatings to combat microbially influenced corrosion by sulfate-reducing bacteria (SRB). The synthesis of iodopropyl-poly(ferrocenylsilane) (PFS-I) thin films on steel substrates and their application for biocorrosion protection is described in this chapter. A protective PFS-I layer was deposited on mechanically polished steel substrates via spin-coating and was utilized against biocorrosion in anoxic environments. This layer was characterized both before and after incubation with *Desulfovibrio vulgaris*, and the roughness of the underlying steel substrate was measured. It was found that the bacteria preferentially colonize the PFS-I layer compared to the bare steel and form FeS particles on the surface. The underlying steel surface, however, appeared unaffected, showing the protective qualities of the PFS-I layer.

Finally, in **Chapter 7**, we summarize our results on PFS-based biointerfaces and provide an outlook for further work. The redox activity and versatile post-polymerization modification of poly(ferrocenylsilanes) render these materials useful for the synthesis and application of novel biointerfaces. In this thesis, a wide range of such applications was explored, yielding results that will advance this field of science.

1.3. Bibliography

1. Manners, I. Poly(ferrocenylsilanes): novel organometallic plastics. Chemical Communications 857–865 (1999).
2. Ni, Y., Rulkens, R., Pudelski, J. K. & Manners, I. Transition metal catalyzed ring-opening polymerization of silicon-bridged [1]ferrocenophanes at ambient temperature. Macromol Rapid Commun 16, 637–641 (1995).

3. Hempenius, M. A., Brito, F. F. & Vancso, G. J. Synthesis and characterization of anionic and cationic poly(ferrocenylsilane) polyelectrolytes. Macromolecules 36, 6683–6688 (2003).
4. Hempenius, M. A. & Vancso, G. J. Synthesis of a polyanionic water-soluble poly(ferrocenylsilane) [8]. Macromolecules 35, 2445–2447 (2002).
5. Cheng, H., Hempenius, M. A., Sui, X. & Vancso, G. J. Catalytic Performance of Pd Nanoparticles Obtained by Direct Reduction in Cellulose–Poly(ferrocenylsilane) Hybrid Sponges. Adv Mater Interfaces 9, 2101664 (2022).
6. Cui, K., Song, Y. & Wang, L. Electrochemical and electrocatalytic behaviors of poly(ferrocenylsilane)/DNA modified glass carbon electrode. Electrochem commun 10, 1712–1715 (2008).
7. Halmagyi, T., Hao, J., Hempenius, M. A. & Vancso, G. J. Poly(ferrocenylsilane) Hydrogels as a Foundry for Metal Nanoparticle Synthesis by Direct Reduction of Electrolytes via a Catalytic Route. ACS Appl Nano Mater 5, 8868–8874 (2022).
8. Song, J. et al. Poly(ferrocenylsilane) electrolytes as a gold nanoparticle foundry: “two-in-one” redox synthesis and electrosteric stabilization, and sensing applications. Nanoscale 9, 19255–19262 (2017).
9. Sui, X., Feng, X., Song, J., Hempenius, M. A. & Vancso, G. J. Electrochemical sensing by surface-immobilized poly(ferrocenylsilane) grafts. J Mater Chem 22, 11261–11267 (2012).
10. Hempenius, M. A., Cirmi, C., Lo Savio, F., Song, J. & Vancso, G. J. Poly(ferrocenylsilane) Gels and Hydrogels with Redox-Controlled Actuation. Macromol Rapid Commun 31, 772–783 (2010).
11. Hempenius, M. A., Cirmi, C., Song, J. & Vancso, G. J. Synthesis of poly(ferrocenylsilane) polyelectrolyte hydrogels with redox controlled swelling. Macromolecules 42, 2324–2326 (2009).
12. Sui, X. et al. Poly(N -isopropylacrylamide)–poly(ferrocenylsilane) dual-responsive hydrogels: synthesis, characterization and antimicrobial applications. Polym Chem 4, 337–342 (2012).
13. Zhang, K., Feng, X., Sui, X., Hempenius, M. A. & Vancso, G. J. Breathing Pores on Command: Redox-Responsive Spongy Membranes from Poly(ferrocenylsilane)s. Angewandte Chemie International Edition 53, 13789–13793 (2014).
14. Feng, X., Wu, H., Sui, X., Hempenius, M. A. & Julius Vancso, G. Thin film hydrogels from redox responsive poly(ferrocenylsilanes): Preparation, properties, and applications in electrocatalysis. Eur Polym J 72, 535–542 (2015).
15. Feng, X., Sui, X., Hempenius, M. A. & Vancso, G. J. Electrografting of stimuli-responsive, redox active organometallic polymers to gold from ionic liquids. J Am Chem Soc 136, 7865–7868 (2014).
16. Wang, H., Huang, Y., Tan, Z. & Hu, X. Fabrication and characterization of copper nanoparticle thin-films and the electrocatalytic behavior. Anal Chim Acta 526, 13–17 (2004).
17. Feng, X., Hempenius, M. A. & Vancso, G. J. Metal Nanoparticle Foundry with Redox Responsive Hydrogels. Macromol Chem Phys 219, 1800223 (2018).
18. Kutnyánszky, E., Hempenius, M. A. & Vancso, G. J. Polymer bottlebrushes with a redox responsive backbone feel the heat: synthesis and characterization of dual responsive poly(ferrocenylsilane)s with PNIPAM side chains. Polym Chem 5, 771–783 (2013).
19. Rasheed, P. A. et al. Controlling the biocorrosion of sulfate-reducing bacteria (SRB) on carbon steel using ZnO/chitosan nanocomposite as an eco-friendly biocide. Corros Sci 148, 397–406 (2019).

20. Moaref, R., Shahini, M. H., Eivaz Mohammadloo, H., Ramezanzadeh, B. & Yazdani, S. Application of sustainable polymers for reinforcing bio-corrosion protection of magnesium implants–a review. Sustain Chem Pharm 29, 100780 (2022).
21. Guo, J. et al. Polymers for combating biocorrosion. Front Mater 5, 319706 (2018).
22. Mitra, D., Kang, E. T. & Neoh, K. G. Polymer-Based Coatings with Integrated Antifouling and Bactericidal Properties for Targeted Biomedical Applications. ACS Appl Polym Mater 3, 2233–2263 (2021).
23. Boulmedais, F. et al. Polyelectrolyte multilayer films with pegylated polypeptides as a new type of anti-microbial protection for biomaterials. Biomaterials 25, 2003–2011 (2004).
24. Rajasekar, A. & Ting, Y. P. Inhibition of biocorrosion of aluminum 2024 aeronautical alloy by conductive ladder polymer poly(o -phenylenediamine). Ind Eng Chem Res 50, 2040–2046 (2011).
25. Aguirre, J. et al. Study of poly(3,4-ethylendioxythiphene) as a coating for mitigation of biocorrosion of AISI 304 stainless steel in natural seawater. Prog Org Coat 113, 175–184 (2017).
26. Xiao, Z. & Farokhzad, O. C. Aptamer-functionalized nanoparticles for medical applications: Challenges and opportunities. ACS Nano 6, 3670–3676 (2012).
27. He, L. et al. Aptasensors for Biomarker Detection. Journal of Analytical Chemistry 2022 77:12 77, 1481–1496 (2022).
28. Erkmen, C., Aydoğdu Tığ, G., Marrazza, G. & Uslu, B. Design strategies, current applications and future perspective of aptasensors for neurological disease biomarkers. TrAC Trends in Analytical Chemistry 154, 116675 (2022).
29. Hosseinzadeh, L. & Mazloum-Ardakani, M. Advances in aptasensor technology. Adv Clin Chem 99, 237–279 (2020).

2. State of the Art

2.1. Poly(ferrocenylsilanes) and other stimulus-responsive polymers: Structure, properties, and applications

2.1.1. Introduction

Metallopolymers are a fascinating class of polymers that incorporate metal atoms, increasing the range of achievable material properties in polymer science[1]. Any polymer containing either main group metals, transition metals, lanthanides or actinides in either the main or the side-chains can be called a metallopolymer, thus this group covers a plethora of different materials with various properties[2]. By combining the versatility of organic polymers with the diverse applications of elements throughout the periodic table, one can imagine the opportunities posed by these materials. The majority of the first metallopolymers were based on metallocenes - compounds that consist of a transition metal atom sandwiched between two cyclopentadienyl rings. The best-known representative of this class of materials is ferrocene, an iron-containing metallocene. In 1992, Manners et al. reported the first successful synthesis of high-molecular weight poly(ferrocenylsilanes), hereinafter abbreviated as PFSs[3]. These polymers consist of a main chain of a ferrocene and a silane or an alkylsilane unit, as shown on Figure 2.1.

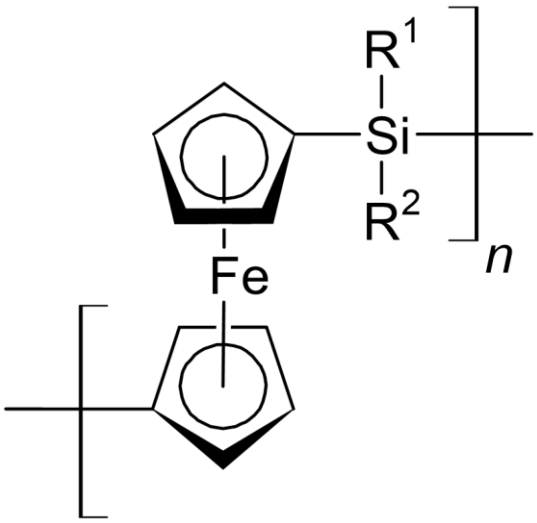

Figure 2.1. General structure of poly(ferrocenylsilanes). R^1 and R^2 side-chains can be a wide variety of ligands, such as alkyl chains, alkyl halogenides, sulfonates, etc.

By employing a then-novel method called thermal ring-opening polymerization (ROP) of silyl-ferrocenophanes, Manners' group was able to synthesize PFSs with number-average molecular weights above 500 kDa[3,4].

2.1.2. Structure and characteristics of poly(ferrocenylsilane)s

2.1.2.1. Post-polymerization side-chain modification

Depending on what alkylsilyl-ferrocenophane monomer is used in the ROP synthesis, the PFS polymer can feature side-chains that are relatively simple to modify, such as 3-halopropyl chains[5]. A wide array of very different PFS systems can be synthesized this way, such as polyelectrolytes[5] and cross-linkable materials[6,7].

2.1.2.2. PFS crosslinking

As the main chain silane groups hold two easily modifiable side-chains, PFSs can, and were, used as precursors for crosslinked polymeric systems[7–10]. It is possible to directly crosslink the

PFS chains with each other, for example via an azide-alkyne Huisgen reaction as was done by Vancso et al.[8] or through the hydrolysis of alkoxysilane side-chains, as shown by Manners et al.[11]. The latter process has the advantage that the ethoxysilane side-chains crosslink directly with each other without necessitating any crosslinking agent. In contrast, the former method relies on an alkynyl-group-containing crosslinker that then reacts with the azide groups on the side-chains of the PFS. By only converting a fraction of the side-chains this way, the researchers were able to tune the properties of the resulting gel. This approach carries with it the additional advantage of leaving some side-chains available for other modifications, such as the introduction of ionic groups to make the gel hydrophilic (hydrogel). The above result highlights another advantageous property of PFSs: if we can tune the stoichiometry of reactants in post-polymerization side-chain modification reactions, a simple homopolymer precursor can yield a statistical copolymer product along which the ferrocenylsilane repeat units carry different side-chains with different functionalities, thus making a wide spectrum of possible material properties available.

It is also possible to create block copolymer gels of PFS with for example poly(N-isopropylacrylamide) (PNIPAM), combining the advantageous properties of each block[9,12]. The ratio of the two polymers influences important properties of the resulting hydrogel, such as the lower critical solution temperature (LCST), swellability, as well as temperature and redox sensitivity.

2.1.2.3. Polyelectrolytes

Polyelectrolytes are polymer chains with a charge-bearing group on their repeat units[13,14]. Consequently, these polymers are electrostatically charged and generally dissolve well in highly polar solutions, such as water. Based on the charge of the ionic groups carried, a polyelectrolyte can be anionic, cationic, or polyampholyte if both anionic and cationic groups can be found in

the chain. The charge of the polyelectrolyte also defines its counterions: anionic polyelectrolytes often carry sodium or other alkali metal ions, or ammonium ions. Cationic polyelectrolytes on the other hand usually have halogen, nitrate or sulfate counterions, but of course a variety of other ions can also be used. The "strength" of the polyelectrolyte can also be defined: if the charge of the ionic groups is dependent on pH (e.g. carboxyl groups, the polymer is a weak polyelectrolyte - one that is only soluble in a specific pH range (in the case of carboxyl groups, generally in the basic regime). Conversely, if the ionic group does not lose its charge at any pH, like sulfate, then the polyelectrolyte is strong, as it will carry charge regardless of the pH of the solution.

The use of PFS polyelectrolytes is straightforward for applications in aqueous solutions. Researchers in Vancso's group have demonstrated the feasibility of polyelectrolyte synthesis from a PFS precursor with a 3-chloropropyl side-chain[5,15]. The substitution of the chlorine to the much better leaving group iodine allows for a great variety of reaction pathways towards both anionic and cationic side-chains. As demonstrated by the same group, the materials available through this synthetic route include strong and weak polyelectrolytes alike[16] and can remain stable in solution even at very high salt concentrations. The possibility of creating water-soluble PFSs can also be applied for solubilizing other polymeric materials such as polystyrene[17] as block copolymers with PFS polyelectrolytes.

2.1.2.4. Stimuli responsiveness of poly(ferrocenylsilane)s

2.1.2.4.1. Redox response

PFSs are innately redox active due to the ferrocene moieties in their main chain. In a neutral state, the iron is in the Fe^{II} oxidation state, and can serve as a reducing agent, losing an electron to yield a ferricenium cation (Fc^{+}) with a Fe^{III} core. This oxidation half reaction has a redox

potential of 400 mV vs. the standard hydrogen electrode[10], which is enough to reduce noble metal salts[18]. The color change from amber to dark green associated with the oxidation of PFS chains signals opportunities for applications in colorimetric sensing[9,19].

2.1.2.4.2. Electrochemical properties of PFS-based systems

As redox active polymers, poly(ferrocenylsilane) containing systems exhibit electrochemical responsiveness. This property of PFSs has been well studied[20,21]. One immediately recognizable electrochemical feature of these polymers is the two pairs of redox peaks of equal intensity on the cyclic voltammogram[20,22]. The exact position of these peaks varies with system parameters as well as the exact structure of the polymer chain, but the phenomenon is almost always observable. The reason behind this characteristic is that the oxidation of the chain is a two-step process. As any iron center is oxidized, the ones immediately next to them become more difficult to oxidize. Thus, in the first step on average every second ferrocene is oxidized, then in the next step, the rest.

Cross-linkable PFSs can be spun into electroactive polymer fibers, which exhibit electro-actuation even at relatively low voltages (1.5-2 V) due to the redox activity inherent to the polymer[11]. Thin films of crosslinked PFS hydrogels were also synthesized and their metal nanoparticle composites exhibit electrocatalytic activity in redox reactions such as ethanol oxidation[23].

The electrochemical properties of PFSs depend heavily on the side-chains, the oxidation state of the main chain as well as potential doping agents. As an example, I_2 doping enables the development of PFS-based p-type semiconductors, which open the door for photoelectrochemical applications[24,25].

2.1.2.4.3. Metal nanoparticle (MNP) foundry

PFS-based systems, owing to their redox activity, tunable solubility and the possibility to crosslink, have been widely researched as promising candidates for metal nanoparticle synthesis and stabilization. Most often, PFS-containing hydrogels are used to stabilize *in situ* reduced metal nanoparticles[10,18,26–29]. Of course, this approach is not specific to polyferrocenylsilanes, rather the idea of using hydrogels to stabilize nanoparticles is a field of its own[26]. PFS-based hydrogels are rather unique, however, in that the polymer gel acts both as reductant and stabilizer to the MNPs[10,18,28,29]. This system was named, by Vancso et al, "metal nanoparticle foundry"[10].

Hydrogels are of course not the only viable approach to PFS-mediated nanoparticle synthesis. Another option is to use PFS-based polyelectrolytes, that is, water-soluble polyferrocenylsilane polymers as reductants and stabilizers for colloidal metal nanoparticles. Gold nanoparticles synthesized this way show excellent stability and the aggregation-induced color change of the localized surface plasmon resonance (LSPR) effect of the gold nanoparticles can act as a signal element in sensors built around the reversible redox activity of PFS chains[16].

A recent study of ours sheds further light on the mechanism of the reduction of gold salts with water-soluble PFS[30]. According to the findings, PFS polymer hydrogels are capable of reducing gold salts far beyond their expected ability, i.e. the stoichiometric 1:3 Au^{III}:Fc ratio. This result hints at a possible catalytic mechanism involving another redox pair such as, for example, the O_2 / H_2O couple. This idea is further reinforced by the fact that salts with redox potentials below that of water oxidation do not exhibit this super-stoichiometric metal formation.

2.1.2.4.4. Thermal response

PNIPAM-PFS block copolymer hydrogels were reported to have dual responsiveness[9,19,31]: aside from the redox sensitivity characteristic of PFS-based systems, these crosslinked networks also exhibit thermal responsivity as can be expected from a PNIPAM-containing

hydrogel. Structural changes in such systems can be induced by varying the two parameters to which the two blocks are responsive. The PFS-PNIPAM hydrogels, aside from the dual responsiveness, exhibit high swellability, dependent on temperature as well as on the amount of PFS poly(ionic liquid) moieties[19].

2.1.3. Applications of poly(ferrocenylsilane)s

The characteristics of PFSs outlined above open the door for numerous applications both for the polymer class itself as well as its composites with metal nanoparticles, hydrogels, and thin film electrodes.

PFS-based hydrogel metal nanoparticle foundries' ability to stabilize and fix in place MNPs reduced from any metal salt with a redox potential below 400 mV makes these systems promising substrates for applications in (electro)catalysis as well as in biomedicine. Vancso et al. made use of these properties to synthesize silver nanoparticles in PFS-PNIPAM hydrogels with 2 % PFS content and to test their antimicrobial activity[18]. While the PNIPAM hydrogels used for the control measurements exhibited no appreciable toxicity towards *Escherichia coli*, the silver nanoparticle-containing PFS-PNIPAM gels developed a clearly noticeable zone of inhibition towards the bacteria. The same article also details the biocompatibility of this same system, and it was found that neither the hydrogel nor the silver nanoparticles exhibited significant cytotoxicity towards the murine fibroblastic cell line MC-3T3 used in the study.

2.1.3.1. Applications in catalysis and electrocatalysis

The noble metals stabilized by PFS hydrogels often have catalytic activity of their own. A good example of this is palladium, a metal widely used in catalysis, which is readily reduced from its salt and stabilized on the surface of PFS nanospheres, as shown by Dou et al[32]. The palladium nanoparticles (PdNPs) stabilized this way exhibited over 95 % conversion rate of 4-

nitrophenol (4-NP) to 4-aminophenol (4-AmP) with $NaBH_4$ as reductant. Over five cycles, the conversion rate did not change, but the rate constant, which was measured as an indicator of catalytic activity, dropped significantly after the first cycle, then remained stable.

Vancso et al. also showed the application of PdNP-PFS composites in catalysis[28]. By uniformly dispersing a PFS polyionic liquid over a cellulose support, the researchers created a substrate and reducing platform for PdNPs. The in situ reduced and stabilized nanoparticles were then applied in the same 4-NP to 4-AmP model reaction. Over 60 minutes, complete conversion was achieved. The composite material also retained its catalytic activity over at least five cycles.

The same group showed the synthesis stabilization of PdNPs in crosslinked PFS hydrogels and the application of this system in the electrocatalytic oxidation of ethanol[33]. By spin-coating the semi-crosslinked polymer onto an indium tin oxide (ITO) electrode, then letting the crosslinking finish on the substrate, uniform thin films of PFS hydrogels could be created. In situ synthesis of PdNPs was then performed to yield PdNP / PFS / ITO composite electrodes. Cyclic voltammetry was used for the model reaction with 1.0 M NaOH and 0.5 M ethanol as electrolyte and reactant, respectively, and the coated ITO as working electrode. A peak appeared at -70 mV, attributed to the electrooxidation of ethanol. The PFS / ITO electrodes did not show electrocatalytic activity by themselves, but the films loaded with PdNPs did, with the oxidation peak doubling over the first 15 cycles and then remaining constant. The system also shows high tolerance to catalyst poisoning.

Manners et al. showed that polystyrene-block-PFS (PS-b-PFS) systems can be used as catalytic precursors for the synthesis of single-walled carbon nanotubes (SWCNTs) with highly controlled structures[34]. Iron acts as a catalyst for the CNT formation, while the PS blocks were used as the nanotube precursors. In thin films, the polymer self-assembled into the desired

structure of PFS chains embedded in the PS matrix. These films were then thermolyzed to 700 °C in air, then at 900 °C in hydrogen gas in order to form iron nanoparticles (FeNPs) from the PFS, then a methane-ethylene gas mixture flow was used to induce the chemical vapor deposition of SWCNTs. In ten minutes, CNTs with diameters around 700 nm formed a uniform pattern over the substrate.

2.1.3.2. Sensing

Ferrocene-containing metallopolymers in general have recently garnered attention in various fields, owing to the vast array of their possible applications[35]. In particular, PFSs have been used as components in redox sensors, as will be detailed in the following.

2.1.3.2.1. Electrochemical sensing

The electroactivity of PFSs can not only be utilized in MNP-assisted electrocatalysis, but also in electrochemical sensing. Vancso et al. have shown the applicability of electrodeposited PFS films on Au-Si electrodes as redox sensors[36]. The polymer was deposited from a polyionic liquid, making use of the previously described formation of Au^- ions and its complexes in such media[37]. The polymer-coated electrode shows good stability and a high degree of resistance towards electrochemical degradation: a 2-hour oxidation at 600 mV (vs silver-silver chloride (Ag/AgCl) reference electrode) induced just 15 % material loss. The sensor also performed well in detecting ascorbic acid (AA) as a model redox analyte, with a limit of detection at 900 nM. This limit, which translates to 0.16 mg AA per kilogram, is well suited for the analysis of the ascorbic acid content of fruits and vegetables[38] as well as of processed products[39].

2.1.3.2.2. Optical sensing

PFS-stabilized gold nanoparticles are promising candidates for colorimetric sensing. The change with nanoparticle size of the wavelength of LSPR-induced absorbance of AuNPs was

used by Vancso et al. to detect redox active analytes[16]. The PFS stabilizing agent, bearing anionic side-chains, on the surface of the nanoparticles was first oxidized with ferric chloride. This prompted the aggregation of the AuNPs, as the charge of the side-chains was now neutralized by the ferricinium cations in the main chain. This aggregation could then be reversed by the addition of ascorbic acid as the PFS chains regained their overall negative charge, again rendering the AuNP surfaces charged. This reversible aggregation-based method has a limit of detection at 10 μM for ascorbic acid. As before, this detection limit is suitable for the analysis of real products containing ascorbic acid[38,39].

2.1.4. Oligonucleotides as stimulus responsive polymers: the curious case of aptamers

Aside from the versatile redox responsive poly(ferrocenylsilane) family, this thesis touches on another group of stimulus responsive polymers: aptamers. These macromolecules consist of a short deoxyribonucleic or ribonucleic acid (DNA or RNA) strand with generally fewer than 30 nucleotides[40] (although aptamers of more than 80 bases are also known[41]) and show a structural affinity towards a particular molecule, protein or even bacteria. Their specific sensitivity has made aptamers attractive candidates as bioreceptors. Although the definition allows for oligopeptide aptamers, in the following "aptamer" will refer solely to oligonucleotide aptamers. With an *in vitro* procedure called systematic evolution of ligands by exponential enrichment (SELEX), oligonucleotide aptamers can be developed for almost any target molecule. During the SELEX process, the oligonucleotide with the highest target affinity is selected and amplified from a random library of 10^9-10^{15} initial sequences[42,43]. The process consists of several selection steps in which the oligonucleotide mixture is exposed to solid substrate-bound instances of the target molecule. Those oligonucleotides which have an affinity

toward the target bind to these molecules with varying strength, depending on the magnitude of affinity of the given oligonucleotide. The aptamer-target complexes are then separated from the unbound oligonucleotides with a separation method tailored for the target and the solid support. This method can be the magnetic separation of paramagnetic support beads[44], affinity chromatography[43], membrane separation[42], etc. Enzymatic amplification such as polymerase chain reaction (PCR) is then used to multiply the bound nucleotide strands. The new library of significantly less varied oligonucleotides obtained after amplification is then used in the next round of selection. A typical SELEX procedure consists of about 12 rounds of different conditions and results in one or a couple of aptamers with high target affinity[42].

The primary signal given off by aptamer bioreceptors is the structural change induced by their binding to the target. Several such aptamer-target binding modes are known. Perhaps the best-researched aptamers, those that bind to the human thrombin protein, form so called G-quadruplexes (Figure 2.2) that interact with an anion binding site of the protein.[45]

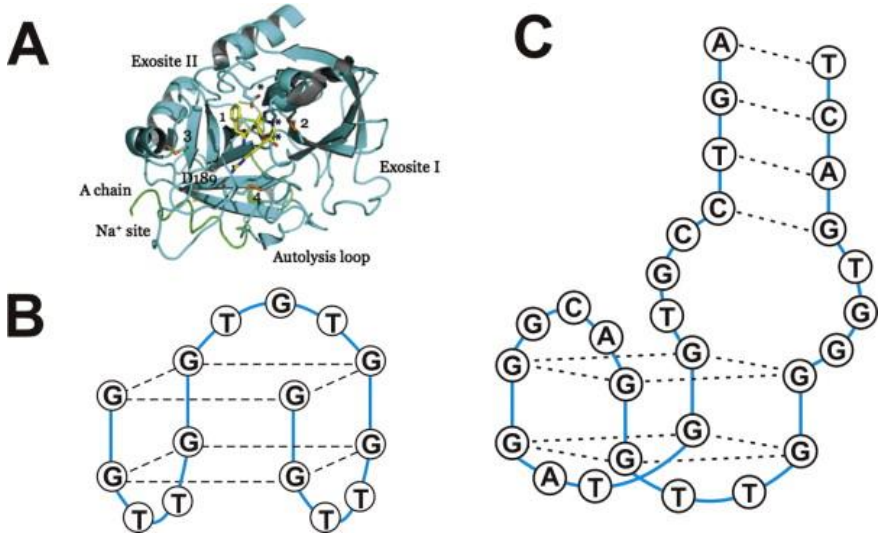

Figure 2.2. Thrombin protein (A) and two frequently used thrombin-specific aptamers (B, C) showing G-quadruplex conformations[45].

Aptamers can also have one (e.g. in the case of the ATP-specific aptamer) or multiple (e.g. the so-called RsmZ sRNA aptamer) loops in their secondary structures[40]. These loops, also called hairpin structures[46], may increase the rigidity of the nucleotide chain and thus induce a conformation that can couple to the target molecule in a "lock and key"-type interaction. Often, aptasensors utilize more than one aptamer strand for the detection of large targets such as proteins or other macromolecules. In the case of the severe acute respiratory syndrome coronavirus 2 (SARS-CoV-2), the pathogen of the recent Coronavirus disease 2019 (COVID-19) pandemic, the spike protein antigen of the virus has multiple aptamer binding sites[47]. This allows for a so-called sandwich-style detection in which one oligonucleotide, the capture aptamer, is bound to a solid support. This aptamer specifically binds to and fixes the antigen in place, then another oligonucleotide strand, named the detection aptamer because it is coupled to a signal transducer system, is introduced. The structural change of the detection aptamer upon binding to the now fixed-in-place antigen induces a color reaction in the transducer system, thus indicating the presence of the antigen[47].

2.1.4.1. Aptamer immobilization on nanoparticles

A frequently used colorimetric transducer in biosensors and in aptasensors in particular is the size-dependent color change of gold nanoparticles (AuNPs)[48]. Colloidal AuNPs– and some other metal nanoparticles– exhibit localized surface plasmon resonance (LSPR) when irradiated with light of significantly longer wavelength than the nanoparticle's size. Due to LSPR, the absorbance spectrum of gold nanoparticle colloids is dependent on their size, with larger nanoparticles absorbing longer wavelengths of light. As Figure 2.3 shows, this results in the AuNP colloidal solution's color changing from red to violet and then to blue as the nanoparticle size increases[49] (Figure 2.3).

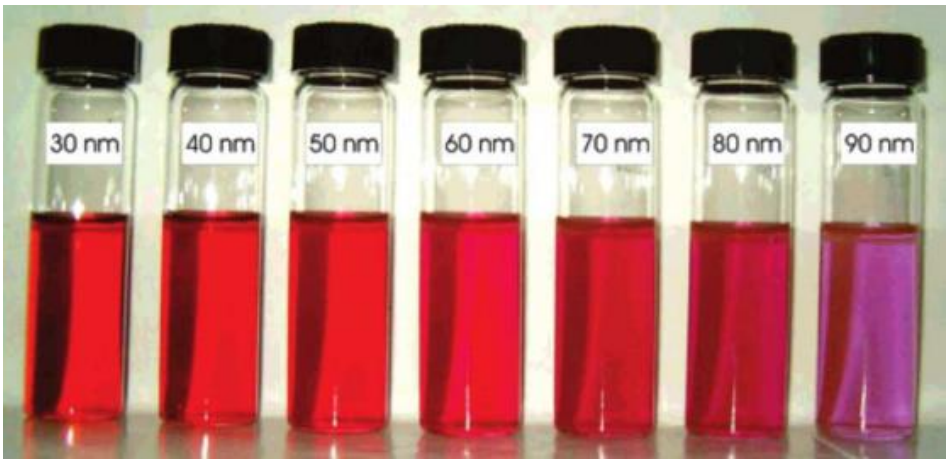

Figure 2.3. Color of colloidal solutions of nanoparticles of different sizes[49].

Colorimetric gold nanoparticle transducers generally include a way for the aptamer-target interaction to induce a size change in the AuNPs. Most often, the aptamer is therefore immobilized on the gold nanoparticles. Covalent coupling of one end of the oligonucleotide strand, either directly to the gold surface or to the capping agent of the nanoparticle, is a widely used method to achieve immobilization[50]. Thiol-terminated aptamers in particular are widely used for AuNP and gold substrate coatings. As a "soft" metal, gold has a high affinity to sulfur, making thiolation an attractive method for aptamer immobilization. A long list of publications on sensors for a wide variety of targets shows that thiol modified aptamers have good utility in aptasensing[51–57].

Aptamer immobilization via peptide-type amide bonds is well-researched on a wide variety of substrates, including gold[58–61]. This method involves an aptamer modified with either an amine or a carboxylic acid group on either its 3' or 5' terminus. The substrate, in turn, is modified with the other functional group. This usually involves an activation step in order for the bond formation to occur, such as the N-ethyl-N′-(3-(dimethylamino)propyl) carbodiimide / N-hydroxysuccinimide (EDC/NHS) mediated coupling reaction[62]. This reaction converts the

carboxylic acid functional group into an NHS-ester, which then reacts with primary amines to form an amide, linking the two molecules–- or a molecule and a solid substrate–- together.

Another aptamer immobilization method, not requiring chemical modification of neither the gold support nor the aptamer strand, is the electrostatic adsorption of the oligonucleotide onto the AuNP. This, however, makes the system susceptible to nonspecific interactions such as salt-induced desorption of the aptamer strands from the nanoparticle, and subsequent aggregation of the AuNPs even without the presence of the target molecule.

Oligonucleotides–- similarly to polymeric DNA and RNA–- carry a negative charge on each nucleotide, due to the phosphate groups in the main chain. This property makes them anionic polyelectrolytes that are, as such, attracted to positively charged surfaces. This has been exploited for aptasensor fabrication, as Zhao et al. have shown[63]. In this paper, the authors simply mixed PCB-77-specific aptamers with a colloidal AuNP solution and have found that after a 10-minute incubation period the aptamers were adsorbed on the gold surface and contributed significantly to the stabilization of the nanoparticles, which could then be utilized for sensing purposes.

2.1.4.1.1. Immobilization via click reactions

Click reactions, which represent an important field within modern organic chemistry[64], have been widely used for bioconjugation applications. The [3+2] dipolar azide-alkyne cycloaddition, first described and subsequently named after Rolf Huisgen[65], was later further developed by the group of Barry Sharpless[66]. The original Huisgen cycloaddition requires the use of a Cu^{I} catalyst, but a catalyst-free, strain-promoted version (SPAAC) was later developed by Bertozzi's group[67]. The two reactions are compared in Scheme 2.1[67]. As can be seen, the Cu^{I}-catalyzed Huisgen cycloaddition uses a linear alkyne, while in the case of the strain-promoted version, the triple bond is contained inside a cyclooctyne ring. This eight-membered

carbon ring remains intact in the reaction, resulting in a bicyclic product. One of the most frequently used cycloalkynes for SPAAC is dibenzocyclooctine (DBCO)[68–70].

Scheme 2.1. Huisgen cycloaddition (a). Strain-promoted azide-alkyne cycloaddition (SPAAC) (b)[67].

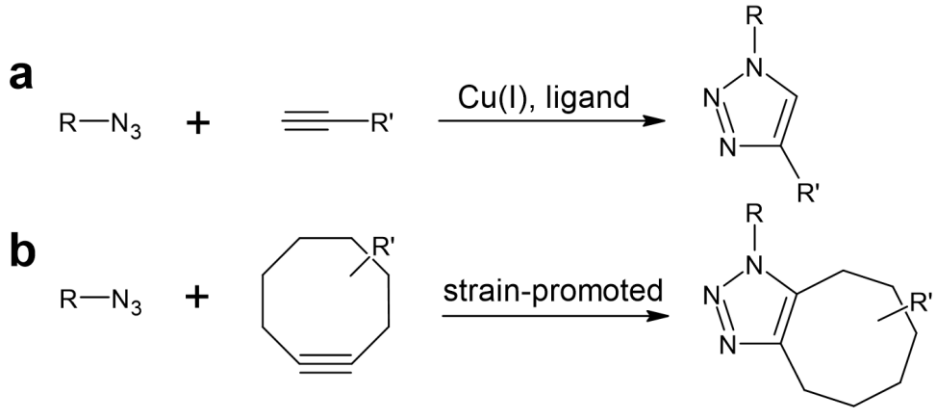

Click cycloaddition reactions have been used for conjugation of DNA strands with other molecules and supports[71–74] as well as for, immobilization before DNA polymerization[75], and linkage of several nanoparticles via a single DNA strand[76]. Well-developed protocols exist for the copper-catalyzed reaction, with a Cu^{II} catalyst precursor activated by reduction with sodium ascorbate[72]. The SPAAC reaction has also been widely studied[77] and used for linkage[68] and fluorescent labeling[78] of aptamers as well as their immobilization on solid surfaces[73]. Other polymers have also been modified with dibenzocyclooctyne for the purposes of functional copolymer formation[69].

The advantage – and one of the main reasons for this wide variety of uses – of the Huisgen cycloaddition and SPAAC is the fact that these reactions are biocompatible, i.e. the end-functionalized biomolecules do not lose their bioactivity, therefore these reactions can be conducted directly *in vivo* without harm to the living organism[73].

2.1.4.2. Colorimetric aptasensors for biomarker detection

Human health is threatened by pollutants and other factors, such as diseases and biological disorders. The onset of these conditions can often be predicted via the monitoring of a variety of indicators called biomarkers. The Biomarker Working Group of the Food and Drug Administration (FDA) and the National Institutes of Health (NIH) of the United States defines biomarkers as "A defined characteristic that is measured as an indicator of normal biological processes, pathogenic processes, or biological responses to an exposure or intervention, including therapeutic interventions"[79]. These materials can further be categorized as susceptibility, diagnostic, monitoring, prognostic, predictive, response, and safety biomarkers depending on the medical utility of a given marker[79,80]. Due to their importance in medicine, biomarker monitoring is an important area of modern biosensor development. Thrombin, an enzyme that converts fibrinogen to fibrin, is a part of the coagulation cascade (the process by which blood clots are formed) and an important biomarker, used in thrombin coagulation assays to determine the risk of thrombosis, hemophilia and other cardiovascular diseases[81,82]. In the field of aptasensor development, thrombin is often used as a model analyte due to the well-defined and characterized nature of the interaction between thrombin and thrombin-binding aptamers via the G-quadruplex structure[81,83] (see Figure 2.2).

Colorimetric aptasensors have been applied for biomarker detection, yielding good selectivity and sensitivity for a variety of targets, such as cancer biomarkers, hormones, enzymes – including thrombin – and small molecules such as adenosine and adenosine triphosphate (ATP). Table 2.1 summarizes literature data on colorimetric aptasensors for biomarker detection, with special attention to thrombin as the model target applied in our own research.

Table 2.1. Literature data on colorimetric aptasensors for biomarker detection.

Analyte	Biomarker	Limit of detection (LOD)	Reference
Adenosine	Cardiovascular diseases	0.1 mM	[84]
ATP	Hepatitis B	0.1 μM	[85]
Dopamine	Parkinson's disease	0.36 μM	[86]
Thrombin	Cardiovascular diseases	0.83 nM	[87]
		0.1 nM	[88]
		20 pM	[89]
		0.40 fM (electrochemical-colorimetric)	[90]
		0.16 nM (fluorescence-colorimetric)	[91]
		1.5 pM	[92]
		2.6 nM	[93]
		1 nM	[94]

8-oxo-7,8-dihydro-2′-deoxyguanosine	Oxidative stress	N.A.	[95]
Clusterin	Alzheimer's and other diseases	5.37 pg mL^{-1}	[96]
PSA	Cancer	20 pg mL^{-1}	[97]
MUC1	Cancer	10 U mL^{-1}	[98]
Nucleolin	Cancer	10 cells mL^{-1}	[99]
Exosomes	Cancer	6.4 μg mL^{-1}	[100]
pLDH	Malaria	8.3-8.7 pM	[101]

2.2. Colloidal stability of nanoparticles

Between the worlds of "true" solutions and heterogeneous mixtures (macroscopic dispersions) "intermediate" colloidal systems exist. Colloids are mixtures consisting of a dispersed (nanoparticles, micelles, macromolecules etc) and a continuous phase (the solvent)[102]. It is important to note that the term "colloid" can sometimes refer to the colloidal dispersion as a whole, or just to the dispersed phase. Going forward, "colloid" will refer to the system as a whole and further distinctions will be clarified where necessary. Furthermore, this theoretical overview deals exclusively with aqueous colloids, as, even though colloidal systems also exist in other solutions, aqueous colloids are the most relevant to the subject of this thesis.

The moieties making up the dispersed phase are of a size between 1 nm and 1 μm, giving rise to properties that are not present in either solutions nor in heterogeneous mixtures. Similarly to

heterogeneous mixtures, the particles of a colloid possess a surface area, enabling – and in fact necessitating – the discussion of surface phenomena[102,103]. Such discussion is also necessary in the present chapter before moving on to the application of polymers and especially PFSs and aptamers for colloidal stabilization.

Due to the small size of the particles making up the colloidal dispersed phase, a relatively much larger fraction of the atoms or molecules making up the particles are at an interface, i.e. the specific surface area of colloidal particles is significantly greater than that of particles in macroscopic dispersions. It can therefore be postulated that surface forces such as surface tension, surface charge etc. have a much greater effect on colloids than on heterogeneous mixtures. These effects will be discussed through the example of nanoparticle (NP) colloids, as the present thesis deals with such systems.

2.2.1. Nanoparticles in colloidal dispersions

As discussed above, nanoparticles can be dispersed in a continuous phase to yield a colloidal system. A variety of forces acts on such systems. Attractive van der Waals forces arising from interactions of individual atoms of separate particles are always present in colloidal systems and drive the aggregation of NPs[104]. This can be counteracted especially in polar solvents by the inherent or induced (for example via the immobilization of charged species on the NP surface) surface charge of the nanoparticles. When discussing colloids, the stability of the system describes the resistance of the system towards aggregation. As surface tension would drive the minimization of particle surfaces – and therefore aggregation – the thermodynamically favored state of colloids will usually be the aggregation of the dispersed phase[103]. This can be kinetically counteracted by the electrostatic repulsion mentioned above, or thermodynamically by steric effects to be described later.

Van der Waals and electrostatic interactions are described by the Derjaguin-Landau-Verwey-Overbeek (DLVO) theory[105,106]. Further interactions such as steric and electrosteric repulsions, polymer bridging and depletion, etc. necessitate discussion beyond this theory.

2.2.1.1. DLVO theory

The DLVO theory describes the interaction between two colloidal particles in a simplified manner, by subsuming every interaction, attractive and repulsive, into a single colloidal total or pair potential (V_T) the magnitude and sign of which determines the overall stability of the colloid. Attractive forces have negative, while repulsive forces a positive sign. The pair potential is the simple sum of the attractive (V_A) and repulsive (V_R) potentials, as seen in Equation 2.1[102]:

$$V_T = V_A + V_R \text{ (Equation 2.1)}$$

V_A and V_T are in turn described in the core DLVO model as the potentials describing Van der Waals and electrostatic forces, respectively.

2.2.1.1.1. Omnipresent attraction: the van der Waals forces

Discussions of van der Waals interactions conventionally deal with three main components: the Keesom, Debye and London forces. The Keesom force originates from the interaction of two permanent dipoles, such as polar molecules or particles. In this case, the alignment of the two particles will be such that their opposite poles will face each other, exerting an attractive force. In contrast, the Debye force necessitates the presence of only one permanent dipole, with which the other particle interacts through its polarizability.

When discussing colloidal systems, the most important van der Waals interaction is the dispersion or London force. This interaction is always active regardless of the presence of dipoles in the system. The motion of electrons in an atom will induce the rapid appearance and

disappearance of minute dipoles, resulting in the appearance of the London attractive force as atoms act on each other through these fluctuating dipoles. In larger particles, this non-directional interaction means that all atoms of one particle attract all atoms of any other particle. The dispersion interaction remains a significant attractive force at distances comparable to the size of colloidal nanoparticles. The DLVO theory then describes the attractive van der Waals effects – and primarily the London force – in the attraction potential, V_A[102]:

$$V_A = -\frac{H}{12}\left[\frac{1}{x(x+2)} + \frac{1}{(x+1)^2} + 2ln\frac{x(x+2)}{(x+1)^2}\right] \text{ where } x = \frac{h}{2r} \text{ (Equation 2.2)}$$

In Equation 2.2, h is the distance between two uniform particles, and r is the radius of those particles. H (denoted in some sources as A) is the Hamaker constant, its magnitude for any system is dependent on the Hamaker constants of the material of the NPs, and of the continuous phase, which are usually in the range of 10^{-20} J[102]:

$$H = \left(\sqrt{H_{NP}} - \sqrt{H_{solvent}}\right)^2 \text{ (Equation 2.3)}$$

At small enough particle separations, where the NP diameter is much greater than the interparticle distance, Equation 2.2 can be simplified:

$$V_A = -\frac{Hr}{12h} \text{ (Equation 2.4)}$$

Equation 2.4 is the form of the attractive potential that is conventionally used in the DLVO theory for the calculation of V_T.

2.2.1.1.2. The electrical double layer (EDL) and electrostatic repulsion

As water is a strongly polar solvent, materials dissolved in it are usually polar or even ionic. Thus, aqueous colloidal particle dispersions can be stabilized by the introduction of surface charges. The location of these charges is perhaps most accurately described by the Stern-Gouy-Chapman model[102,103], which describes the charged nanoparticle-medium interface as a so-

called electrical double layer (EDL). The precise characteristics of the EDL are dependent on a variety of factors such as particle size, charge density, electrolyte concentration, etc[102,107], but certain general considerations can be made. On a surface carrying charges, counterions arrange themselves in two regions[102]. Ions of the inner layer are strongly adsorbed on the surface, there hydration shell is broken; they are "touching" the surface. The Inner Helmholtz Plane (IHP) passes through the center of these ions. The beginning of the outer diffuse layer is determined by the Outer Helmholtz Plane (OHP), passing through the center of those ions closes to the surface which are completely solvated, i.e. their hydration shell is intact. Surface potential decays exponentially in the diffuse layer. The thickness of the EDL is indicated by the Debye length (L_D), defined as the distance from the surface where the electric potential is 37 % of that on the particle surface. The Debye length is described by Equation 2.5.

$$L_D = \left(\frac{\varepsilon\varepsilon_0 k_B T}{2N_A e^2 I}\right)^{\frac{1}{2}} \quad \text{(Equation 2.5)}$$

In Equation 2.5, ε is the dielectric constant, ε_0 is the vacuum permittivity, k_B is Boltzmann's constant, N_A is Avogadro's constant, and I is the ionic strength. The double layer as explained above is presented on Figure 2.4.

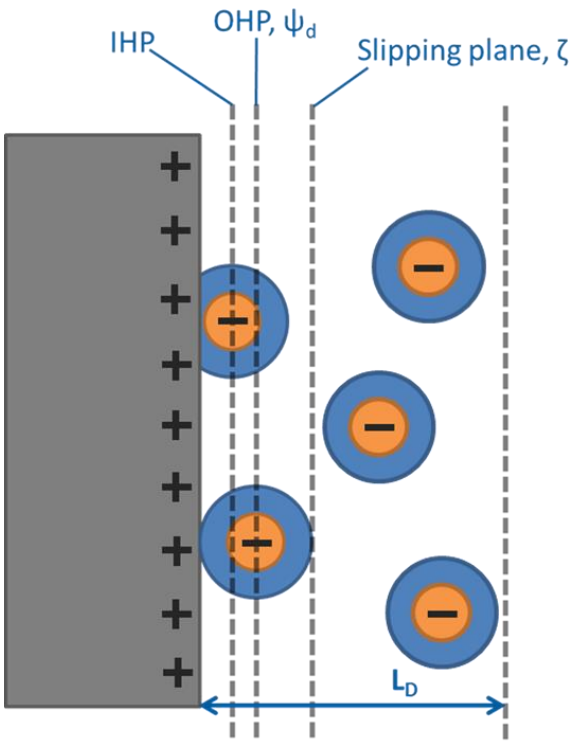

Figure 2.4. Schematic ilustration of the electric double layer forming around a positively charged surface. The IHP is the Inner Helmholtz Plane, OHP is the Outer Helmholtz Plane. The slipping or shear plane is the point where the zeta potential is defined, to be explained below. L_D is the Debye length, determining the thickness of the EDL.

The overlap of the EDLs of two similarly charged particles results in the emergence of a repulsive force between the two NPs. The magnitude of this force can be described using the Debye-Hückel approximation[104,107]. V_R is defined for cases where $\kappa h < 3$ in Equation 2.6.

$$V_R = 2\pi\varepsilon\varepsilon_0 r\psi_d e^{-\kappa h} \text{ where } \kappa = \frac{1}{L_D} \quad \text{(Equation 2.6)}$$

Here, ε is the dielectric constant, ε_0 is the vacuum permittivity, and ψ_d is the electric potential in the diffuse layer, defined at the OHP.

2.2.1.1.3. Colloidal stability in the DLVO theory

With both V_A and V_R defined, the pair potential can now be expanded from Equation 2.1 using Equations 2.4 and 2.6.:

$$V_T = -\frac{Hr}{12h} + 2\pi\varepsilon\varepsilon_0 r\psi_d^2 e^{-\kappa h} \text{ (Equation 2.7)}$$

The pair potential can be visualized as a function of normalized interparticle distance $V_T(\kappa h)$ as shown on Figure 2.5[108].

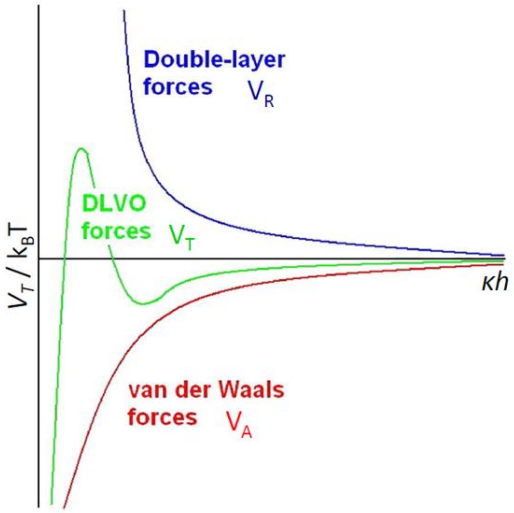

Figure 2.5. Visual representation of the pair potential (green) as a function of the normalized interparticle distance. The component potentials V_R (blue) and V_A (red) are also shown.

As can be expected, V_A and V_R have opposite signs and both tend towards infinity as the interparticle distance approaches zero. At very low distances, V_T tends to negative infinity, reinforcing the notion that aggregation of colloidal NPs is thermodynamically favorable. If V_R is large enough however, there exists an energy barrier that can essentially be considered the "activation energy" necessary for aggregation. If the magnitude of this barrier is much greater than 1.5 k_BT – roughly the energy of Brownian collisions – then this barrier can be considered as largely impassable, and the colloidal nanoparticles as kinetically stabilized.

Such kinetic stabilization of nanoparticles via the introduction of surface charges is extremely ubiquitous in colloid science. NPs of such great variety of materials have been stabilized in colloid with the help of surface charges that listing all would be a futile endeavor. Perhaps the most ubiquitous among all materials in such colloidal systems are metal nanoparticles (MNPs)[109–111], but NPs of other materials such as metal oxides, silica, latexes, etc. can also be stabilized in aqueous media through the introduction of a surface charge.

One limitation of surface charge-based stabilization is that it is by definition dependent on the thickness of the EDL, in other words the magnitude of L_D. The Debye length, as Equation 2.5 shows, decreases with increasing ionic strength, i.e. with the introduction of higher-charge or higher concentration electrolytes. In sufficiently high ionic strength conditions, all charges are screened by the electrolyte, and the EDL becomes too thin to stabilize the NPs as the energy barrier of aggregation disappears. This electrolyte concentration is referred to as the critical coagulation concentration (CCC)[107,112], marking the boundary between slow and fast aggregation.

2.2.1.2. Measuring surface charge

As shown above, surface charge is an essential property of aqueous colloidal nanoparticles. Its measurement is equally important, but is complicated by the fact that ψ_d, the electric potential of the diffuse layer, which is the surface charge-related quantity used in the DLVO theory, cannot be measured directly[102]. To quantify the surface charge of colloidal nanoparticles, another quantity needs to be defined. This is the zeta (ζ) potential, or the electric potential on the slipping plane. The advantage of ζ versus ψd is that the former can be measured by laser Doppler electrophoresis (LDE), a DLS-based technique that determines the surface charge of a particle from its electrophoretic velocity[113,114].

The slipping or shear plane (see Figure 2.4) is the limit within which the counterions and other moieties move together with the nanoparticle[113,114]. Conversely, ions beyond the slipping plane move independently from the NP and can therefore be separated from it with the application of an electric field. The Henry equation (Equation 2.8) defines μ_E, the electrophoretic mobility as a function of the zeta potential.

$$\mu_E = \frac{2\varepsilon\varepsilon_0\zeta}{3\eta} f(\kappa r) \text{ (Equation 2.8.)}$$

Here ε is the dielectric constant, ε_0 is the vacuum permittivity, η is solvent viscosity, and f(κr) is the Henry-function, introduced to make the Henry equation valid for non-point charges. In Smoluchowski's approximation (valid when the particle size is much greater than the EDL thickness), f(κr) = 1.5, thus Equation 2.8 is simplified:

$$\mu_E = \frac{\varepsilon\varepsilon_0\zeta}{\eta} \text{ (Equation 2.9.)}$$

By using LDE to measure the electrophoretic mobility of particles in a known electrolyte and a known electric field, the zeta potential can be calculated using Equations 2.8 and 2.9, providing invaluable information on the surface charge of the NPs and therefore the stability of the colloid.

2.2.1.3. Non-DLVO interactions

The DLVO theory describes only van der Waals and electrostatic forces. Many other interactions can exist in a real colloidal system which are not included in this theory. It is especially difficult to describe the stability and behavior of colloids that contain polymers, either in dispersion or immobilized on nanoparticle surfaces.

Polymers, both dissolved and immobilized, behave differently from solid particles. Their solution behavior is strongly dependent on their conformation, which is in turn influenced by

solvent-polymer interactions and thus the material qualities of both the polymer repeat units and the solvent.

Below we summarize the interactions not covered by the DLVO theory with special attention to those that are relevant to polymer-containing colloids.

2.2.1.3.1. Steric repulsion

Polymers immobilized on nanoparticle surfaces can assume different conformations depending on the density of immobilized strands and on solvent-polymer interactions. If the coverage of the NP surface is dense and in a good solvent for the polymer, steric stabilization of the nanoparticles becomes possible. If such nanoparticles approach each other, the overlapping polymer layers can either interpenetrate akin to the teeth of two combs or brushes, or both polymer layers can be compressed[102,104]. These phenomena are illustrated on Figure 2.6.

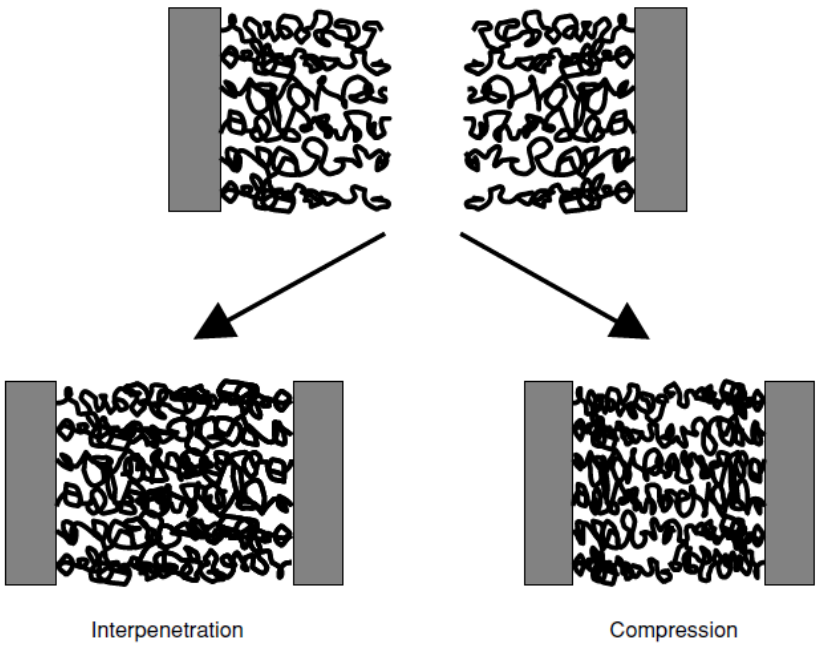

Figure 2.6. Possible scenarios upon the approach of interfaces densely covered with well-soluble polymer[102].

Both interpenetration and compression are thermodynamically unfavorable, therefore the premise established for DLVO-type systems – that aggregation is thermodynamically favored – is often invalid for polymer-stabilized nanoparticles[115].

Steric stabilization of nanoparticles has attracted great scientific interest. Since the earliest use of sterically stabilized particles by the Egyptians 4000 years ago[116], a wide variety of materials have been stabilized in colloidal systems through interfacial polymer immobilization. Materials such as silica[117], titania[118], metallic composite materials[119], AuNPs[119,120] and even nanomaterials for biomedical applications[121,122] have been synthesized using steric effects for stabilization.

Remarkably, Elbert et al. have demonstrated the application of PFSs with nonpolar side-chains for the stabilization of polystyrene nanoparticles (PSNPs) through the *in situ* polymerization of the PFS on the PSNP surface[123]. The anionic polymerization method resulted in a 4 nm thick PFS layer around the PSNPs. This layer stabilizes the particles in tetrahydrofuran (THF), presumably via steric stabilization, as evidenced by dynamic light scattering measurements showing similar hydrodynamic diameters for the PSNPs without and with PFS coating (247 nm for bare PSNPs, 209 to 239 nm for PFS-coated PSNPs, depending on sample).

2.2.1.3.2. Depletion interaction

Described by the Asakura-Oosawa model[124,125], depletion in this context refers to the destabilizing effects of well-soluble but non-adsorbing polymers on colloidal particles. The physical background of this interaction is illustrated on Figure 2.7.

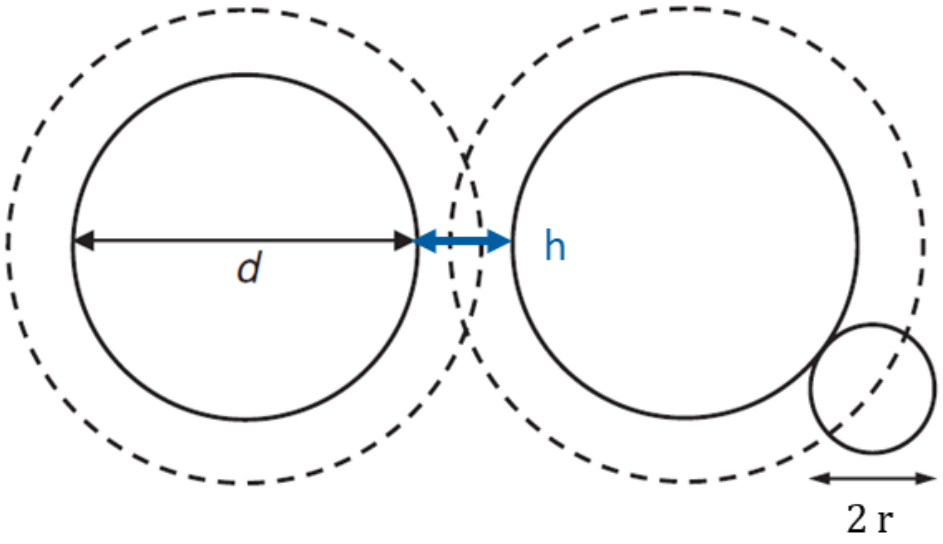

Figure 2.7. Illustration of the depletion interaction. The large circles represent nanoparticles of size d at distance h, while the smaller circle is a non-adsorbing polymer globule of size 2r.

As shown, an exclusion zone or so-called depletion layer develops around the particles. Since the polymer globules "bounce off" the particles, the presence of polymer in this depletion layer is energetically unfavorable. Thermodynamics thus dictates that the overall volume of depletion layers of all particles in the system is minimized, i.e. the particles are "pushed" towards each other by the polymer globules, causing the overlap of depletion layers.

2.2.1.3.3. Bridging

Long enough polymer chains may attach to more than one nanoparticle at a time, causing bridging interaction, where the polymer binds two or more particles together, driving aggregation[102] (Figure 2.8). This may be useful in certain applications, as ABA block copolymers whose A segments, which adsorb well to the NP surface, are separated by non-adsorbing B segments have been utilized as flocculants[126]. This technique has its utilities in wastewater treatment[127], as well as in the food[128] and mineral processing[129,130] industries for the

removal of undesirable particulate materials. In these applications, filtration of the aggregate is usually necessary to complete the treatment[126].

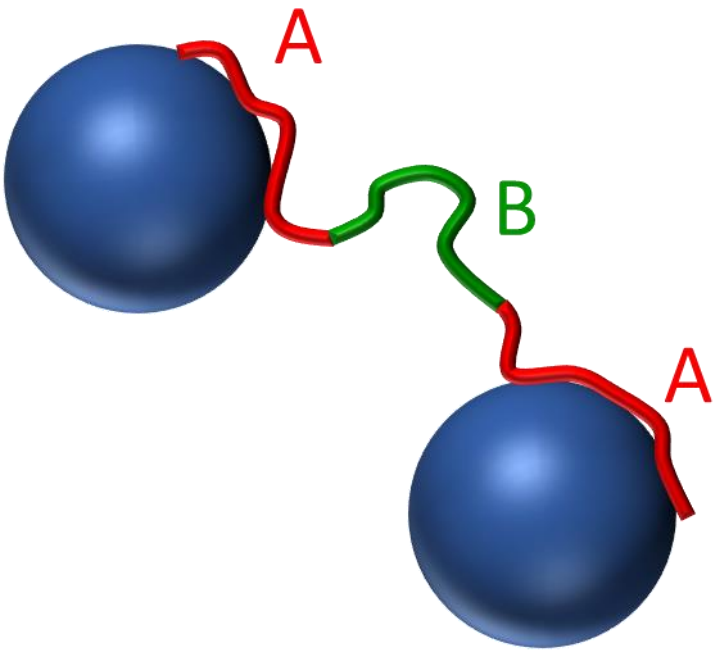

Figure 2.8. Illustration of bridging interactions with ABA copolymers, where only the A segments adsorb well on the nanoparticle surface.

2.2.2. Polyelectrolytes for colloid stabilization

As described previously, polyelectrolytes are polymer molecules with dissociated ionic groups either in their main chain, or on pendant side-chains[131]. The "strength" of a polyelectrolyte, i.e. the solubility of the molecule at different pH values, is determined by the quality and density of the charge-bearing groups. Both anionic (e.g. sulfonate[16], carboxylate[132]) and cationic (e.g. quaternary amine[5]) groups can be incorporated in the polymer to render it a polyelectrolyte.

2.2.2.1.1. Electrosteric repulsion

Polyelectrolytes, when immobilized on the surface of a particle, can exhibit both electrostatic and steric effects at the same time, in a so-called electrosteric stabilization[16,107,131,133–135]. Electrosterically stabilized particles retain the energy barrier caused by the electrostatic repulsion of the charged polyelectrolyte moieties, but, akin to sterically stabilized NPs, the polymer layer on the surface also causes interpenetration -or compression-based repulsion. Polyelectrolytes exhibiting electrosteric effects are popular for stabilizing aqueous colloids, as it is often true that electrosterically-stabilized NPs are more stable than electrostatically stabilized ones[135,136].

2.2.2.1.2. Poly(ferrocenylsilanes) as colloid stabilizers

PFS polyelectrolytes have been widely utilized as electrosteric stabilizing agents for nanoparticles of various materials. Vancso, Manners and others have done pioneering work in the field, utilizing different approaches for the preparation of PFS-stabilized colloids.

PFS-based polyelectrolytes can form colloids by themselves, as demonstrated by Zoetebier et al., who synthesized poly(ferrocenylsilane)-poly(ethylene glycol) (PFS-PEG) copolymers via the grafting of the PEG moieties to 10 to 25 % of the PFS side-chains[137]. These polymers, which also bore quaternary amine side groups, were then coupled with DNA to form PFS/DNA coacervate polyplexes. Upon addition of the polymer to the DNA, the zeta potential of the latter changed from -10 to -20 mV to high positive values at +40 to +55 mV, indicating successful complex formation. These particles have a hydrodynamic diameter of 110 nm.

You et al. have utilized redox-active PFS-containing micelles to synthesize and stabilize Pd nanoparticles[32] (PdNPs). The PFS/Pd nanocomposites, synthesized at different Pd concentrations by simply tuning the concentration of the Pd salt precursor, were electrosterically stabilized by the anionic polyelectrolyte. In this same paper, the PdNPs were

utilized as catalysts for the reduction of 4-nitrophenol and showed catalytic activity comparable with other similar catalysts.

Vancso et al. have combined the "nanoparticle foundry" phenomenon of PFSs, originally developed for PFS-containing hydrogels[8,10,18], with the ability of PFSs to form polyelectrolytes of various types[5]. This combination was used for the in situ synthesis and stabilization of PFS-stabilized gold nanoparticles of positive (PFS^{+}AuNP) and negative (PFS^{-}AuNP) surface charge with PFS polyelectrolytes containing quaternary amine and sulfonate side groups, respectively. The resulting particles showed different properties depending on PFS-to-gold ratio and on which PFS was used. To identify differences in the colloidal behavior of diverse systems, stability tests were performed in high ionic strength conditions. Remarkably, the PFS^{-}AuNPs have shown signs of electrosteric stabilization. As evidenced by transmission electron microscopy and UV-visible spectroscopy, the PFS^{-}AuNPs did not aggregate substantially even upon addition of 3 M NaCl electrolyte. In contrast, PFS^{+}AuNPs aggregated even at NaCl concentration of 0.1 M. Additionally, the redox activity of PFS was employed to tune the reversible aggregation and disaggregation of PFS-AuNPs. In these tests, the anionic polyelectrolyte was first oxidized with $FeCl_3$, inducing positive charges in the ferrocene centres, counteracting the negative charges of the side-chains and inducing aggregation. Then ascorbic acid was added to reverse the process, and upon reduction of the ferrocene centres, de-aggregation of the particles was observed. In addition to highlighting the importance of structural properties and electrolytic groups, this paper also provided data about an antioxidant sensor, utilizing the reversible aggregation method to detect ascorbic acid at concentrations as low as 10 μM.

2.2.2.1.3. Electrosteric effect of surface-bound aptamers

Aptamers, being composed of nucleotides the phosphate groups of which carry a negative charge in physiological conditions, are anionic polyelectrolytes. This property and their chain-like structure grant aptamers and other oligonucleotides electrosteric stabilizing properties[138,139]. This helps protect aptamer-coated nanoparticles from aggregation in high ionic strength environments. However, in the presence of the aptamer's target molecule this electrosteric stabilization is often lost either due to desorption of the aptamer[63] or, in the case of covalently immobilized oligonucleotides, due to the changes induced by the target in the secondary structure of the aptamer[140].

This effect has been widely utilized in colorimetric aptasensors and especially those exploiting the size-dependent LSPR effect of gold nanoparticles[138]. A vast variety of target materials can be detected with such systems, from heavy metal ions[141,142], persistent organic pollutants (POPs)[63,143], antibiotics[140,144] and pesticides[145–147] to biomarkers[148,149] and more[58,138].

2.3. Biocorrosion

Some microorganisms exhibit the ability to induce corrosion of metal substrates in processes generally known as biocorrosion or microbially influenced corrosion (MIC).

Corrosion is the phenomenon arising when a metal surface is immersed in an electrolyte solution and two points in close proximity on the metal surface have different potentials[150,151]. Alternatively, the same effect can arise from the contact of two dissimilar metals. In both cases, the point with the lowest potential acts as the anode, inducing metal dissolution:

$$M \rightarrow M^{z+} + ze^{-}$$ (Equation 2.10)

At the same time, a reduction half-reaction occurs on the cathode, generally oxygen reduction in aqueous media:

$$4e^{-} + O_2 + 4H^{+} \rightarrow 2H_2O; E° = 1.229\ V$$ (Equation 2.11)

It needs to be noted that all potentials are shown against the standard hydrogen electrode (SHE) unless indicated otherwise. The long-term result of these processes is widespread solubilization of the metal surface, often coupled with the deposition of metal ion compounds such as rust (a mix of $Fe_2O_3 \cdot nH_2O$, FeO(OH), and $Fe(OH)_3$) in the case of iron corrosion. This damages the metal and worsens its mechanical properties.

Biocorrosion or microbially influenced corrosion (MIC) is any process of corrosion driven by microorganisms, usually bacteria. Biofilms formed by organisms such as sulfur reducing bacteria (SRBs), iron-oxidizing, iron reducing bacteria and others induce a wide variety of interactions between the bacteria and the metal surface such that drive corrosion[152]. This section will focus on biocorrosion by SRBs and the prevention thereof. SRBs grow in a pH range between mildly acidic (pH 4.0) to mildly basic (pH 9.5) conditions and operate under anaerobic conditions where they reduce sulfate to sulfide while oxidizing organic substances into organic acids and carbon dioxide[153]. Both the carbon source and the sulfur source varies by genus[154]: *Desulfotomaculum* strains, for example, are acetate oxidizing, while *Desulfovibrio*, a very well-known genus, does not use acetate.

Sulfur reduction occurs in a multistep reaction, where organic matter, such as acetate is oxidized[155]:

$$CH_3COO^- + SO_4^{2-} \rightarrow 2HCO_3^- + HS^-; E° = 0.062\ V \text{ (Equation 2.12)}$$

Alternatively, hydrogen produced on the cathodic biofilm substrate may be the electron donor for the reduction of sulfate[153,155]:

$$4H_2 + H^+ + SO_4^{2-} \rightarrow HS^{2-} + 4H_2O; E° = 0.197\ V \text{ (Equation 2.13)}$$

Thus, the anaerobic reduction of one sulfate ion yields one sulfide with the electrons for the reaction being supplied from the surrounding medium, including the hydrogen produced in the biofilm. On metal surfaces, this results in corrosive phenomena, such as cathodic

depolarization[151,153]. Cathodic depolarization refers to a process where the surface-adsorbed hydrogen on the cathode of a corrosion cell is scavenged. As the H_2 is the result of proton reduction on the cathode, the reaction equilibrium is shifted with the consumption of the product. Thus, SRBs increase the reaction rate on the cathode by its depolarization. Of course, this in turn increases oxidation (metal dissolution) on the anode, driving its corrosion.

2.3.1. Biocorrosion protection

The prevention of biocorrosion and other biofouling processes is easiest to achieve by keeping metal equipment clean. Depending on the type of surface deposit, mechanical and chemical cleaning procedures have been developed[153,156]. Pigging, a method wherein a special device is pushed through a pipe, taking deposited material with itself, is a widely used way of pipeline cleaning. The tool is called a pig, and several different variations are in use depending on the pipe and the contaminant[153].

More relevant to this discussion are the chemical and biochemical methods for biocorrosion protection. These can either be biocides[153,156], chemicals which outright kill the film-forming bacteria thereby reducing the size and thickness of the biofilm, or by the application of antimicrobial coatings[156]. These layers either have biocidal effects themselves or hinder the adhesion and reactivity of the biofilm. They have the advantage of being able to be applied in situations where biocides cannot be used, such as in marine environments[157] and in implants[158,159] on which antifouling formulations have widespread applications.

2.3.1.1. Antimicrobial protective coatings

When designing an antimicrobial coating material, mechanical properties like stiffness and surface topology are paramount in determining the adhesion-hindering effect of said coating. The desired properties also depend on the bacteria against which the coating is targeted.

According to Lichter et al., the adhesion and colony formation of *Staphylococcus epidermidis* on polyelectrolyte coated polymer substrates is dependent on the elastic modulus of the surface[160]. Higher elastic modulus (that is, greater stiffness) increases *S. epidermidis* viability, while it is independent from surface roughness. Vallée Réhel et al. have determined the dependence of cell adhesion viability of two marine bacteria, a *Bacillus* and a *Pseudoalteromonas* strain depending on the surface stiffness of agarose hydrogel substrates. It was found that the *Bacillus* strain's adhesion did not depend on surface stiffness, but the *Pseudoalteromonas* adhered better to stiffer surfaces.

In 2015, a review by Ren et al. was published summarizing the effect of material properties on the adhesion and biofilm forming ability of bacteria[161]. As the discussed systems exist in aqueous media, surface charge plays a role in biofilm adhesion. The negatively charged bacteria are repelled from negatively charged surfaces, thus these are more resistant to biofilm formation, while positively charged surfaces increase it. Stiffness, as discussed above, also plays a role, with bacteria usually, but not always, growing better on surfaces with higher elastic modulus. Roughness and the surface topology also have an influence. Rougher surfaces increase the contact area between biofilm and substrate, thus it is beneficial to design smooth surfaces or coatings.

Polymers have widely been used for adhesion prevention, as a review by Pehkonen et al. shows[157]. Anionic polyelectrolytes in particular are interesting due to imparting negative surface charge to the substrate, repelling most bacteria[161]. However, Skorb et al. have investigated the dependence of the biofilm forming ability of *Escherichia coli* depending on surface charge, controlled by polyelectrolyte coatings[162] and it was found that polycation coatings hinder biofilm spreading while polyanions have no influence. In addition, since weak

polyelectrolytes' charge is dependent on pH, the bacterial adhesion properties of these materials were also pH sensitive.

Kim et al. have investigated bacterial adhesion on porous poly(vinyl acetate) (PVAc) coated magnesium alloys[159]. Dichlorometane-treated polymer coatings were found to hinder biocorrosion and exhibited uniform degradation of the substrate. Yazdani et al. have published a review on the use of sustainable polymers as biocorrosion protective layers on magnesium implants[158]. A plethora of natural polymers such as poly(lactic acid) (PLA), polycaprolactone (PCL), polydopamine (PDA) etc. are targets of intense research due to their biocompatibility, price and mechanical-biochemical properties that make them suitable for use in living systems.

2.3.1.2. Bactericidal coatings

The mechanical prevention of adhesion is not the only way of hindering biofilm formation with a coating material. Many materials exist which are capable of killing film-forming bacteria. Kaur et al. have utilized bishexadecylpyridinium hafnium hexachlorate (HfCPC), a Hf containing cationic surfactant against two halophilic bacteria, *Halobacterium salinarium* and *Halococcus morrhuae*[163]. The coating had a 95.9 % inhibition efficiency in saline media and 76.5 % in a bacteria-inoculated sea medium. Additionally, the surfactant exhibits electrochemical passivation properties on iron substrates, inhibiting both biochemical and chemical corrosion.

Gold-containing cetyltrimethylammonium bromide (AuCTAB) surfactants have been shown to infer biocorrosion resistance on galvanized steel substrates in simulated marine conditions by Kaur et al[164]. The film formed a passive layer towards electron transfer on the surface, hindering corrosion, while also being toxic and antiadhesive towards *Halobacterium salinarium* and *Halococcus morrhuae* strains. The coating was found to protect the substrate for over a week.

Polymers are logical targets of researching the development of biocidal coatings owing to their variability and ability to incorporate other materials such as antibiotics in their matrix. Chen et al. have created a system wherein polyelectrolyte coatings were loaded with antibiotics which they then released under specific conditions[165]. The authors have immobilized gentamicin (GS) in a poly(acrylic acid)-poly(ethylenimine) (PAA-PEI) films. The resulting composite released the drug at physiological pH over 120 hours to 14 days. Thus, the layer provided antibiotic activity over a long time period as tested against *Staphylococcus aureus*, while the viability of human lymphatic endothelial cells (HLECs) has not been affected.

Similar research was conducted by Palecek et al. who have incorporated antimicrobial β-peptidomimetics (peptide-mimicking short amino acid chains) in chitosan-hyaluronic acid polyelectrolyte films on Ti surfaces and tested the resulting antibiotic activity on *S. aureus*[166]. It was found that the peptide-loaded films have prevented biofilm formation for up to 24 days with good selectivity against the bacteria while leaving mammalian model cells viable.

Teo et al. have reviewed different methods of using polymer brushes against biofouling in marine applications[167]. As discussed previously, anionic polyelectrolytes and hydrophilic polymers can resist biofilm adhesion. At the same time, modification of polymer brushes with antimicrobial agents confers antibiotic activity to the protective layer.

The same group has published an article about layer-by-layer (LBL) deposition of alternating polyethylenimine-β-cyclodextrin and ferrocene-modified chitosan layers[168]. The coating was created by simple alternating immersion of the substrate in solutions of the two materials. The resulting multilayer composite was resistant to adhesion of bacteria of several strains.

Metal nanoparticles, especially AgNPs, have been targets of research for their antimicrobial properties. Gu et al. have shown that a ferrocene-containing polymer, which can both act as a crosslinker for gelatin and reducing agent for in situ AgNP formation can be used to form an

antimicrobial hydrogel-AgNP composite. The researchers have used ring-opening methatesis polymerization (ROMP) to generate the tetrablock copolymer with ferrocene being present in the side-chains of one block. This Fc was used as the reductant for the $AgNO_3$ to Ag reduction reaction in gelatin, and the resulting hydrogel was tested against *Escherichia coli* and *Staphylococcus aureus*. It was found that the composite had antimicrobial activity against both bacteria, the exact magnitude of which depended on composition and preparation method.

2.3.2. Polymer thin film coatings

As seen above, polymer films are useful both in themselves and in composites as biocorrosion inhibitors. The exact method of synthesis of these films is always dependent on the materials used, and falls into one of several groups. Electrochemical methods are feasible if the substrate is conductive, which is often the case as metals are the main targets of biocorrosion[169]. *In situ* electropolymerization[170,171], electrospinning[172] and electrochemical surface modification[36] are all possible for the electrodeposition of polymers. For composite coatings, LBL deposition with alternating immersion in solutions of different coating materials can also be applied[168,173].

Physicochemical methods for coating deposition are very widespread. Dip coating is used when uniform layers are desired, often for LBL deposition[168,173]. The process is mostly used for sol-gel deposition[174], and starts with the immersion of the substrate into a precursor solution at a constant speed, then leaving it there for a given time. Then the substrate is pulled out, also at constant speed. This deposits a uniform amount of precursor solution on the surface. Then, the solution is dried either at room temperature or in an oven.

Drop casting, perhaps the simplest physicochemical coating method consists in the deposition of a droplet onto the substrate and letting it dry, usually under inert gas flow[175]. The main draws of this method are its simplicity and suitability for practically every substrate, solvent and coating material. However, in applications where uniform coatings are desired, drop casting is

less useful as there is little control over the drying process. In addition, a marked «coffee ring» appears during the drying as the solute migrates outward. This is due to the edge of the solvent droplet being pinned in place by surface tension, preventing further spreading. At this thinner and fixed part of the droplet, relative solvent evaporation is faster, inducing outward flow - and with it, solute transport - from the center of the droplet. The result is a macroscopic ring of thicker coating at the edge of the layer.

Spin-coating is widely used for the mechanical deposition of thin, uniform layers from volatile solvents. In this method, a sample is placed on a rotating holder and immobilized there usually by vacuum. Then, the solution or suspension containing the material we intend to deposit is dropped onto the surface, which is standing still (static spin-coating) or already rotating (dynamic spin-coating). After this, the rotation speed is set to a constant value for a given time, then the substrate is stopped again. As seen on Scheme 2.2[176], many different processes occur during this time, which act together to create a uniform layer. The thickness can also be influenced by changing these parameters. For spin-coating, it is important to use a solvent in which suspension or dissolution of the material is adequate, and which has a low enough boiling point, as non-volatile solvents are simply spun off of the substrate, not leaving a layer behind. The substrate also needs to be reasonably flat and perfectly dust-free, otherwise regions with thinner and thicker coatings will develop.

Table 2.2 summarizes literature data on anticorrosion polymer layer deposition processes.

Scheme 2.2. Forces and effects acting on a spinning sample during spin-coating deposition.

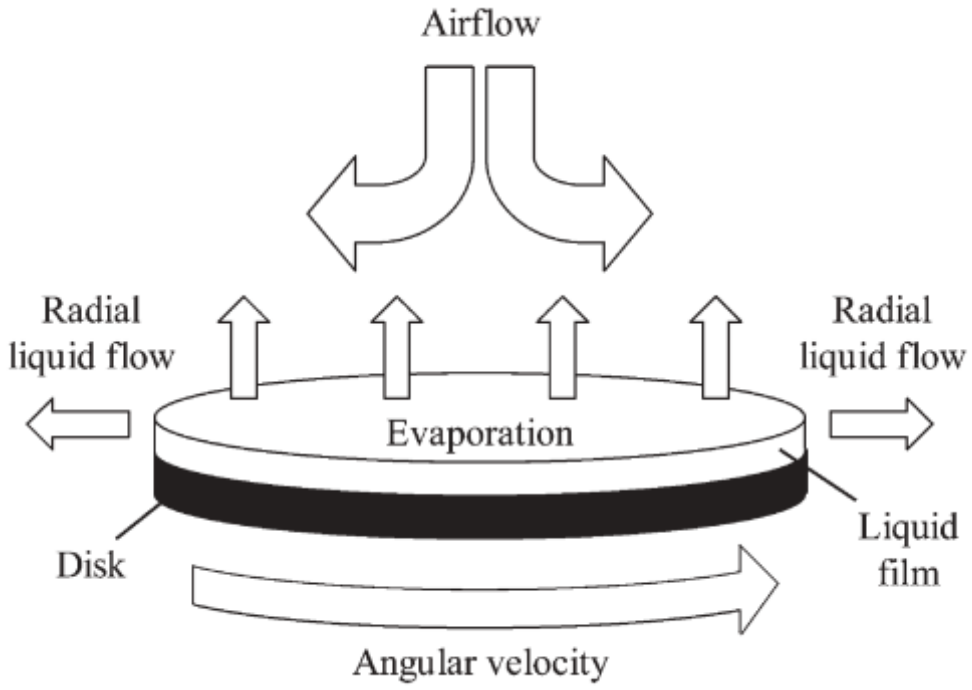

Table 2.2 Summary of literature on polymer deposition methods for corrosion inhibition applications.

Type	Material	Substrate	Method	Ref.	Notes
Electro-chemical	PEDOT*	Stainless steel	In situ electropolymerization	171	*Poly (ethoxydioxythiophene)
	PEDOT	Mg	In situ electropolymerization	170	
	PLA*	Mg alloy	Electrospinning	177	Poly(lactic acid)
	PVC	Al, Steel, Brass	Electrospinning	178	

	PFDA-co-AA-b-PAN*	Al	Electrospinning	[179]	*:poly (heptadecafluoro-decylacrylate-co-acrylic acid)-block-polyacrylonitrile
	PVA	Al	Electrospinning	[180]	
	PoPD*	Al alloy	Cyclic voltammetric deposition	[181]	*: poly(o-phenylenediamine)
Dip coating	PEI-β-CD, Fc-CHT*	Stainless steel	Immersion LBL coating	[168]	*: polyethylenimine-β-cyclodextrin, ferrocene-modified chitosan
	P4VP*	Stainless steel	LBL sol-gel deposition, SI-ATRP***	[173]	*: poly(4-vinylpyridine) **: surface-initiated atom transfer radical polymerization
	PVAc	Mg alloy	Immersion coating	[159]	
	PLA	Mg alloy	Immersion coating	[177]	
Drop casting	PMBTS2MA-co-PTFEM*	Steel		[182]	*: poly(bi-2-mercaptobenzothiazole methacrylate)-co-poly(2,2,2-trifluoroethyl methacrylate)
	PMMA-PSF-CNFs*	Slide glass		[183]	*: poly(methyl methacrylate)-polysulfone-carbon nanofibers
Spin-coating	PLLA, PCL*	Mg	Static spin-coating	[184]	*: poly-L-lactic acid, poly(ε-caprolactone)
	PEI	Mg alloy		[185]	

PANI-PAA/PEI*	Stainless steel	Static spin-coating	[186]	*:polyaniline-poly(acrylic acid)/poly(ethylene imine)
ZrO2-PMMA	Stainless steel	Sol-gel spin-coating	[187]	

2.4. Bibliography

1. Bellas, V. & Rehahn, M. Polyferrocenylsilane-based polymer systems. *Angewandte Chemie - International Edition* **46**, 5082–5104 (2007).
2. Whittell, G. R. & Manners, I. Metallopolymers: New Multifunctional Materials. (2007) doi:10.1002/adma.200702876.
3. Foucher, D. A., Tang, B. Z. & Manners, I. Ring-Opening Polymerization of Strained, Ring-Tilted Ferrocenophanes: A Route to High Molecular Weight Poly (ferrocenylsilanes). *J Am Chem Soc* **114**, 6246–6248 (1992).
4. Kulbaba, K. & Manners, I. Polyferrocenylsilanes: Metal-Containing Polymers for Materials Science, Self-Assembly and Nanostructure Applications. *Macromol. Rapid Commun* **22**, 711–724 (2001).
5. Hempenius, M. A., Brito, F. F. & Vancso, G. J. Synthesis and characterization of anionic and cationic poly(ferrocenylsilane) polyelectrolytes. *Macromolecules* **36**, 6683–6688 (2003).
6. Wang, J. J. *et al.* Preparation of polyferrocenylsilane via thermal ROP, synthesis of polyferrocenylsilane with methacrylate side chain and its photochemical cross-linking properties. *Mater Lett* **60**, 1416–1419 (2006).
7. Wu, J. *et al.* Ferrocene-based redox-responsive polymer gels: Synthesis, structures and applications. *J Organomet Chem* **828**, 38–51 (2017).
8. Zoetebier, B., Hempenius, M. A. & Vancso, G. J. Redox-responsive organometallic hydrogels for in situ metal nanoparticle synthesis. *Chemical Communications* **51**, 636–639 (2014).
9. Sui, X. *et al.* Poly(N-isopropylacrylamide)-poly(ferrocenylsilane) dual-responsive hydrogels: Synthesis, characterization and antimicrobial applications. *Polym Chem* **4**, 337–342 (2013).
10. Feng, X., Hempenius, M. A. & Vancso, G. J. Metal Nanoparticle Foundry with Redox Responsive Hydrogels. *Macromol Chem Phys* **219**, 1800223 (2018).
11. McDowell, J. J., Zacharia, N. S., Puzzo, D., Manners, I. & Ozin, G. A. Electroactuation of alkoxysilane-functionalized polyferrocenylsilane microfibers. *J Am Chem Soc* **132**, 3236–3237 (2010).
12. Zhang, M. *et al.* Modular synthesis of polyferrocenylsilane block copolymers by Cu-catalyzed alkyne/azide 'click' reactions. *Macromolecules* **46**, 1296–1304 (2013).
13. Koetz, J. & Kosmella, S. *Polyelectrolytes and Nanoparticles*. *Polyelectrolytes and Nanoparticles* (Springer Berlin Heidelberg, 2007). doi:10.1007/978-3-540-46382-5.
14. Meka, V. S. *et al.* A comprehensive review on polyelectrolyte complexes. *Drug Discov Today* **22**, 1697–1706 (2017).
15. Zhang, K., Zhang, M., Feng, X., Hempenius, M. A. & Vancso, G. J. Switching Light Transmittance by Responsive Organometallic Poly(ionic liquid)s: Control by Cross Talk of Thermal and Redox Stimuli. *Adv Funct Mater* **27**, 1–8 (2017).
16. Song, J. *et al.* Poly(ferrocenylsilane) electrolytes as a gold nanoparticle foundry: 'two-in-one' redox synthesis and electrosteric stabilization, and sensing applications. *Nanoscale* **9**, 19255–19262 (2017).

17. Ahmed, R., Patra, S. K., Chabanne, L., Faul, C. F. J. & Manners, I. Hierarchical organometallic materials: Self-assembly of organic-organometallic polyferrocenylsilane block polyelectrolyte-surfactant complexes in bulk and in thin films. *Macromolecules* **44**, 9324–9334 (2011).
18. Sui, X. *et al.* Poly(N -isopropylacrylamide)–poly(ferrocenylsilane) dual-responsive hydrogels: synthesis, characterization and antimicrobial applications. *Polym Chem* **4**, 337–342 (2012).
19. Feng, X. *et al.* Highly Swellable, Dual-Responsive Hydrogels Based on PNIPAM and Redox Active Poly(ferrocenylsilane) Poly(ionic liquid)s: Synthesis, Structure, and Properties. *Macromol Rapid Commun* **37**, 1939–1944 (2016).
20. Chen, T. *et al.* Electrochemical Behavior of Poly(ferrocenyldimethylsilane-b-dimethylsiloxane) Films. *Journal of Physical Chemistry B* **109**, 4624–4630 (2005).
21. Khan, A. *et al.* Research advances in the synthesis and applications of ferrocene-based electro and photo responsive materials. *Appl Organomet Chem* **32**, e4575 (2018).
22. Hailes, R. L. N., Oliver, A. M., Gwyther, J., Whittell, G. R. & Manners, I. Polyferrocenylsilanes: synthesis, properties, and applications. *Chem Soc Rev* **45**, 5358–5407 (2016).
23. Feng, X., Wu, H., Sui, X., Hempenius, M. A. & Julius Vancso, G. Thin film hydrogels from redox responsive poly(ferrocenylsilanes): Preparation, properties, and applications in electrocatalysis. *Eur Polym J* **72**, 535–542 (2015).
24. Cyr, P. W., Tzolov, M., Manners, I., Sargent, E. H. & Rogers, E. S. Photooxidation and photoconductivity of polyferrocenylsilane thin films. *Macromol Chem Phys* **204**, 915–921 (2003).
25. Masson, G., Beyer, P., Cyr, P. W., Lougv, A. J. & Manners, L. Synthesis and reversible redox properties of an electron-rich polyferrocenylsilane with tert-butyl substituents on the cyclopentadienyl ligands. *Macromolecules* **39**, 3720–3730 (2006).
26. Thoniyot, P. *et al.* Nanoparticle–Hydrogel Composites: Concept, Design, and Applications of These Promising, Multi-Functional Materials. *Advanced Science* **2**, 1400010 (2015).
27. Al-Kharusi, H. N., Wu, L., Whittell, G., Harniman, R. & Manners, I. Synthesis, thin-film self-assembly, and pyrolysis of ruthenium-containing polyferrocenylsilane block copolymers. *Polym Chem* **9**, 2951–2963 (2018).
28. Cheng, H., Hempenius, M. A., Sui, X. & Vancso, G. J. Catalytic Performance of Pd Nanoparticles Obtained by Direct Reduction in Cellulose–Poly(ferrocenylsilane) Hybrid Sponges. *Adv Mater Interfaces* **9**, 2101664 (2022).
29. Wang, H., Wang, X., Winnik, M. A. & Manners, I. Redox-mediated synthesis and encapsulation of inorganic nanoparticles in shell-cross-linked cylindrical polyferrocenylsilane block copolymer micelles. *J Am Chem Soc* **130**, 12921–12930 (2008).
30. Halmagyi, T., Hao, J., Hempenius, M. A. & Vancso, G. J. Poly(ferrocenylsilane) Hydrogels as a Foundry for Metal Nanoparticle Synthesis by Direct Reduction of Electrolytes via a Catalytic Route. *ACS Appl Nano Mater* **5**, 8868–8874 (2022).
31. Hailes, R. L. N., Oliver, A. M., Gwyther, J., Whittell, G. R. & Manners, I. Polyferrocenylsilanes: Synthesis, properties, and applications. *Chem Soc Rev* **45**, 5358–5407 (2016).
32. You, J., Manners, I. & Dou, H. In Situ Preparation of Composite Redox-Active Micelles Bearing Pd Nanoparticles for the Reduction of 4-Nitrophenol. *Langmuir* **37**, 9089–9097 (2021).

33. Feng, X., Wu, H., Sui, X., Hempenius, M. A. & Julius Vancso, G. Thin film hydrogels from redox responsive poly(ferrocenylsilanes): Preparation, properties, and applications in electrocatalysis. *Eur Polym J* **72**, 535–542 (2015).
34. Lu, J. Q. *et al.* High-quality single-walled carbon nanotubes with small diameter, controlled density, and ordered locations using a polyferrocenylsilane block copolymer catalyst precursor. *Chemistry of Materials* **17**, 2227–2231 (2005).
35. Gallei, M. & Rüttiger, C. Recent Trends in Metallopolymer Design: Redox-Controlled Surfaces, Porous Membranes, and Switchable Optical Materials Using Ferrocene-Containing Polymers. *Chemistry – A European Journal* **24**, 10006–10021 (2018).
36. Feng, X., Sui, X., Hempenius, M. A. & Vancso, G. J. Electrografting of stimuli-responsive, redox active organometallic polymers to gold from ionic liquids. *J Am Chem Soc* **136**, 7865–7868 (2014).
37. Ghilane, J., Fontaine, O., Martin, P., Lacroix, J. C. & Randriamahazaka, H. Formation of negative oxidation states of platinum and gold in redox ionic liquid: Electrochemical evidence. *Electrochem commun* **10**, 1205–1209 (2008).
38. Mieszczakowska-Frąc, M., Celejewska, K. & Płocharski, W. Impact of Innovative Technologies on the Content of Vitamin C and Its Bioavailability from Processed Fruit and Vegetable Products. *Antioxidants* **10**, 54 (2021).
39. Kabasakalis, V. Ascorbic acid content of commercial fruit juices and its rate of loss upon storage. *Food Chem* **70**, 325–328 (2000).
40. Hasegawa, H. *et al.* Methods for Improving Aptamer Binding Affinity. *Molecules 2016, Vol. 21, Page 421* **21**, 421 (2016).
41. Berkal, M. A. *et al.* Glyphosate–Exonuclease Interactions: Reduced Enzymatic Activity as a Route to Glyphosate Biosensing. *Macromol Biosci* 2200508 (2023)
42. Gopinath, S. C. B. Methods developed for SELEX. *Anal Bioanal Chem* **387**, 171–182 (2007).
43. Jo, M. *et al.* Development of single-stranded DNA aptamers for specific bisphenol A detection. *Oligonucleotides* **21**, 85–91 (2011).
44. Stoltenburg, R., Schubert, T. & Strehlitz, B. In vitro Selection and Interaction Studies of a DNA Aptamer Targeting Protein A. *PLoS One* **10**, e0134403 (2015).
45. Deng, B. *et al.* Aptamer binding assays for proteins: The thrombin example—A review. *Anal Chim Acta* **837**, 1–15 (2014).
46. Goda, T. & Miyahara, Y. A hairpin DNA aptamer coupled with groove binders as a smart switch for a field-effect transistor biosensor. *Biosens Bioelectron* **32**, 244–249 (2012).
47. Svobodova, M. *et al.* Aptamer Sandwich Assay for the Detection of SARS-CoV-2 Spike Protein Antigen. *ACS Omega* **6**, 35657–35666 (2021).
48. Charbgoo, F., Soltani, F., Taghdisi, S. M., Abnous, K. & Ramezani, M. Nanoparticles application in high sensitive aptasensor design. *TrAC Trends in Analytical Chemistry* **85**, 85–97 (2016).
49. Subara, D. & Jaswir, I. Gold nanoparticles: Synthesis and application for Halal authentication in meat and meat products. *Int J Adv Sci Eng Inf Technol* **8**, 1633–1641 (2018).
50. Balamurugan, S., Obubuafo, A., Soper, S. A. & Spivak, D. A. Surface immobilization methods for aptamer diagnostic applications. *Anal Bioanal Chem* **390**, 1009–1021 (2008).

51. Shu, H., Wen, W., Xiong, H., Zhang, X. & Wang, S. Novel electrochemical aptamer biosensor based on gold nanoparticles signal amplification for the detection of carcinoembryonic antigen. *Electrochem commun* **37**, 15–19 (2013).
52. Zhang, X. & Yadavalli, V. K. Surface immobilization of DNA aptamers for biosensing and protein interaction analysis. *Biosens Bioelectron* **26**, 3142–3147 (2011).
53. Wang, J., Munir, A., Li, Z. & Zhou, H. S. Aptamer–Au NPs conjugates-enhanced SPR sensing for the ultrasensitive sandwich immunoassay. *Biosens Bioelectron* **25**, 124–129 (2009).
54. Sun, C., Zhao, S., Qu, F., Han, W. & You, J. Determination of adenosine triphosphate based on the use of fluorescent terbium(III) organic frameworks and aptamer modified gold nanoparticles. *Microchimica Acta* **187**, 1–9 (2020).
55. Su, Z. *et al.* Effective covalent immobilization of quinone and aptamer onto a gold electrode via thiol addition for sensitive and selective protein biosensing. *Talanta* **164**, 244–248 (2017).
56. Balamurugan, S., Obubuafo, A., Soper, S. A., McCarley, R. L. & Spivak, D. A. Designing highly specific biosensing surfaces using aptamer monolayers on gold. *Langmuir* **22**, 6446–6453 (2006).
57. Xie, Y. *et al.* Sensitive colorimetric detection for lysozyme based on the capture of a fixed thiol-aptamer on gold nanoparticles. *New Journal of Chemistry* **43**, 4531–4538 (2019).
58. Wu, W. *et al.* An Aptamer-Based Biosensor for Colorimetric Detection of Escherichia coli O157:H7. *PLoS One* **7**, e48999 (2012).
59. Liss, M., Petersen, B., Wolf, H. & Prohaska, E. An aptamer-based quartz crystal protein biosensor. *Anal Chem* **74**, 4488–4495 (2002).
60. Clark, S. L. & Remcho, V. T. Electrochromatographic Retention Studies on a Flavin-Binding RNA Aptamer Sorbent. *Anal Chem* **75**, 5692–5696 (2003).
61. Potyrailo, R. A., Conrad, R. C., Ellington, A. D. & Hieftje, G. M. Adapting Selected Nucleic Acid Ligands (Aptamers) to Biosensors. *Anal Chem* **70**, 3419–3425 (1998).
62. Wang, C., Yan, Q., Liu, H. B., Zhou, X. H. & Xiao, S. J. Different EDC/NHS activation mechanisms between PAA and PMAA brushes and the following amidation reactions. *Langmuir* **27**, 12058–12068 (2011).
63. Cheng, R., Liu, S., Shi, H. & Zhao, G. A highly sensitive and selective aptamer-based colorimetric sensor for the rapid detection of PCB 77. *J Hazard Mater* **341**, 373–380 (2018).
64. Press release: The Nobel Prize in Chemistry 2022 - NobelPrize.org. https://www.nobelprize.org/prizes/chemistry/2022/press-release/.
65. Huisgen, R. 1,3-Dipolar Cycloadditions. Past and Future. *Angewandte Chemie International Edition in English* **2**, 565–598 (1963).
66. Rostovtsev, V. V., Green, L. G., Fokin, V. V. & Sharpless, K. B. A Stepwise Huisgen Cycloaddition Process: Copper(I)-Catalyzed Regioselective "Ligation" of Azides and Terminal Alkynes. *Angewandte Chemie* **41**, 2596–2599 (2002).
67. Agard, N. J., Prescher, J. A. & Bertozzi, C. R. A strain-promoted [3 + 2] azide-alkyne cycloaddition for covalent modification of biomolecules in living systems. *J Am Chem Soc* **126**, 15046–15047 (2004).

68. Li, J., Hu, K., Zhang, Z., Teng, X. & Zhang, X. Click DNA cycling in combination with gold nanoparticles loaded with quadruplex DNA motifs enable sensitive electrochemical quantitation of the tuberculosis-associated biomarker CFP-10 in sputum. *Microchimica Acta* **186**, 1–7 (2019).
69. Kardelis, V., Chadwick, R. C. & Adronov, A. Click Functionalization of a Dibenzocyclooctyne-Containing Conjugated Polyimine. *Angew Chem Int Ed Engl* **55**, 945–949 (2016).
70. Yang, X. *et al.* Well-defined dibenzocyclooctyne end functionalized polymers from atom transfer radical polymerization. *Polymer (Guildf)* **55**, 1128–1135 (2014).
71. Gramlich, P. M. E., Wirges, C. T., Manetto, A. & Carell, T. Postsynthetic DNA Modification through the Copper-Catalyzed Azide–Alkyne Cycloaddition Reaction. *Angewandte Chemie International Edition* **47**, 8350–8358 (2008).
72. Hong, V., Presolski, S. I., Ma, C. & Finn, M. G. Analysis and Optimization of Copper-Catalyzed Azide–Alkyne Cycloaddition for Bioconjugation. *Angewandte Chemie* **121**, 10063–10067 (2009).
73. Eeftens, J. M., van der Torre, J., Burnham, D. R. & Dekker, C. Copper-free click chemistry for attachment of biomolecules in magnetic tweezers. *BMC Biophys* **8**, 1–7 (2015).
74. Lallana, E., Riguera, R. & Fernandez-Megia, E. Reliable and Efficient Procedures for the Conjugation of Biomolecules through Huisgen Azide–Alkyne Cycloadditions. *Angewandte Chemie International Edition* **50**, 8794–8804 (2011).
75. Fan, W. *et al.* Click Chemical Ligation-Initiated On-Bead DNA Polymerization for the Sensitive Flow Cytometric Detection of 3′-Terminal 2′-O-Methylated Plant MicroRNA. *Anal Chem* **90**, 5390–5397 (2018).
76. Fischler, M. *et al.* Chain-like assembly of gold nanoparticles on artificial DNA templates via ‘click chemistry’. *Chemical Communications* 169–171 (2007).
77. Lutz, J. F. Copper-Free Azide–Alkyne Cycloadditions: New Insights and Perspectives. *Angewandte Chemie International Edition* **47**, 2182–2184 (2008).
78. Oishi, M., Nakao, S. & Kato, D. Enzyme-free fluorescent-amplified aptasensors based on target-responsive DNA strand displacement via toehold-mediated click chemical ligation. *Chemical Communications* **50**, 991–993 (2013).
79. FDA-NIH Biomarker Working Group. *BEST (Biomarkers, EndpointS, and other Tools) Resource*. (Food and Drug Administration (US): National Institutes of Health (US), 2016).
80. Califf, R. M. Biomarker definitions and their applications. **243**, 213–221 (2018). doi:10.1177/1535370217750088
81. Tripodi, A. Thrombin Generation Assay and Its Application in the Clinical Laboratory. *Clin Chem* **62**, 699–707 (2016).
82. Binder, N. B. *et al.* Clinical use of thrombin generation assays. *Journal of Thrombosis and Haemostasis* **19**, 2918–2929 (2021).
83. Pagano, B., Martino, L., Randazzo, A. & Giancola, C. Stability and Binding Properties of a Modified Thrombin Binding Aptamer. *Biophys J* **94**, 562–569.
84. Li, F. *et al.* Adenosine detection by using gold nanoparticles and designed aptamer sequences. *Analyst* **134**, 1355–1360 (2009).
85. Mao, Y. *et al.* A simple and sensitive aptasensor for colorimetric detection of adenosine triphosphate based on unmodified gold nanoparticles. *Talanta* **168**, 279–285 (2017).

86. Zheng, Y., Wang, Y. & Yang, X. Aptamer-based colorimetric biosensing of dopamine using unmodified gold nanoparticles. *Sens Actuators B Chem* **156**, 95–99 (2011).
87. Wei, H., Li, B., Li, J., Wang, E. & Dong, S. Simple and sensitive aptamer-based colorimetric sensing of protein using unmodified gold nanoparticle probes. *Chemical Communications* 3735–3737 (2007).
88. Chen, Z. *et al.* Real Colorimetric Thrombin Aptasensor by Masking Surfaces of Catalytically Active Gold Nanoparticles. *ACS Appl Mater Interfaces* **8**, 102–108 (2016).
89. Zhao, Y. *et al.* Microfluidic chip-based silver nanoparticles aptasensor for colorimetric detection of thrombin. *Talanta* **150**, 81–87 (2016).
90. Zhang, Y., Xia, J., Zhang, F., Wang, Z. & Liu, Q. A dual-channel homogeneous aptasensor combining colorimetric with electrochemical strategy for thrombin. *Biosens Bioelectron* **120**, 15–21 (2018).
91. Duan, W., Wang, X., Wang, H. & Li, F. Fluorescent and colorimetric dual-mode aptasensor for thrombin detection based on target-induced conjunction of split aptamer fragments. *Talanta* **180**, 76–80 (2018).
92. Huang, Y. *et al.* Label-free colorimetric aptasensor based on nicking enzyme assisted signal amplification and DNAzyme amplification for highly sensitive detection of protein. *Anal Chem* **85**, 4423–4430 (2013).
93. Zheng, C. *et al.* One-pot synthesized DNA-templated Ag/Pt bimetallic nanoclusters as peroxidase mimics for colorimetric detection of thrombin. *Chemical Communications* **50**, 13103–13106 (2014).
94. Zhang, Z., Wang, Z., Wang, X. & Yang, X. Magnetic nanoparticle-linked colorimetric aptasensor for the detection of thrombin. *Sens Actuators B Chem* **147**, 428–433 (2010).
95. Choodet, C. *et al.* Combined in silico and in vitro study of an aptasensor based on citrate-capped AuNPs for naked-eye detection of a critical biomarker of oxidative stress. *RSC Adv* **9**, 17592–17600 (2019).
96. Wen, L. *et al.* Colorimetric Aptasensor for the Visual and Microplate Determination of Clusterin in Human Urine Based on Aggregation Characteristics of Gold Nanoparticles. *ACS Omega* **8**, 16000–16008 (2023).
97. Shayesteh, O. H. & Ghavami, R. A novel label-free colorimetric aptasensor for sensitive determination of PSA biomarker using gold nanoparticles and a cationic polymer in human serum. *Spectrochim Acta A Mol Biomol Spectrosc* **226**, 117644 (2020).
98. Li, N. *et al.* A SERS-colorimetric dual-mode aptasensor for the detection of cancer biomarker MUC1. *Anal Bioanal Chem* **412**, 5707–5718 (2020).
99. Borghei, Y. S. *et al.* Visual detection of cancer cells by colorimetric aptasensor based on aggregation of gold nanoparticles induced by DNA hybridization. *Anal Chim Acta* **904**, 92–97 (2016).
100. Jiang, Y. *et al.* Aptamer/AuNP Biosensor for Colorimetric Profiling of Exosomal Proteins. *Angewandte Chemie - International Edition* **56**, 11916–11920 (2017).
101. Jeon, W., Lee, S., Dh, M. & Ban, C. A colorimetric aptasensor for the diagnosis of malaria based on cationic polymers and gold nanoparticles. *Anal Biochem* **439**, 11–16 (2013).
102. Hughes, R. *et al. Colloid Science: Principles, Methods and Applications, 2nd Edition*. (Wiley, 2010).
103. Israelachvili, J. N. *Intermolecular and Surface Forces*. (Elsevier, 2011). doi:10.1016/C2011-0-05119-0.
104. Russel, W. B., Saville, D. A. & Schowalter, W. R. *Colloidal Dispersions*. (Cambridge University Press, 1989). doi:10.1017/CBO9780511608810.
105. Verwey, E. J. W. Theory of the stability of lyophobic colloids. *Journal of Physical and Colloid Chemistry* **51**, 631–636 (1947).

106. Derjaguin, B. & Landau, L. Theory of the stability of strongly charged lyophobic sols and of the adhesion of strongly charged particles in solutions of electrolytes. *Prog Surf Sci* **43**, 30–59 (1993).
107. Szilagyi, I., Trefalt, G., Tiraferri, A., Maroni, P. & Borkovec, M. Polyelectrolyte adsorption, interparticle forces, and colloidal aggregation. *Soft Matter* **10**, 2479–2502 (2014).
108. Boinovich, L. DLVO forces in thin liquid films beyond the conventional DLVO theory. *Curr Opin Colloid Interface Sci* **15**, 297–302 (2010).
109. Zhou, J., Ralston, J., Sedev, R. & Beattie, D. A. Functionalized gold nanoparticles: Synthesis, structure and colloid stability. *J Colloid Interface Sci* **331**, 251–262 (2009).
110. Jia, C. J. & Schüth, F. Colloidal metal nanoparticles as a component of designed catalyst. *Physical Chemistry Chemical Physics* **13**, 2457–2487 (2011).
111. Polte, J. Fundamental growth principles of colloidal metal nanoparticles – a new perspective. *CrystEngComm* **17**, 6809–6830 (2015).
112. Takács, D., Tomšič, M. & Szilagyi, I. Effect of Water and Salt on the Colloidal Stability of Latex Particles in Ionic Liquid Solutions. *Colloids and Interfaces 2022, Vol. 6, Page 2* **6**, 2 (2021).
113. Tucker, I. M. *et al.* Laser Doppler Electrophoresis applied to colloids and surfaces. *Curr Opin Colloid Interface Sci* **20**, 215–226 (2015).
114. Smith, M. C., Crist, R. M., Clogston, J. D. & McNeil, S. E. Zeta potential: a case study of cationic, anionic, and neutral liposomes. *Anal Bioanal Chem* **409**, 5779–5787 (2017).
115. Zhulina, E. B., Borisov, O. V. & Priamitsyn, V. A. Theory of steric stabilization of colloid dispersions by grafted polymers. *J Colloid Interface Sci* **137**, 495–511 (1990).
116. Napper, D. H. Steric stabilization. *J Colloid Interface Sci* **58**, 390–407 (1977).
117. Worthen, A. J., Tran, V., Cornell, K. A., Truskett, T. M. & Johnston, K. P. Steric stabilization of nanoparticles with grafted low molecular weight ligands in highly concentrated brines including divalent ions. *Soft Matter* **12**, 2025–2039 (2016).
118. Elbasuney, S. Sustainable steric stabilization of colloidal titania nanoparticles. *Appl Surf Sci* **409**, 438–447 (2017).
119. Ning, Y. *et al.* Spatially Controlled Occlusion of Polymer-Stabilized Gold Nanoparticles within ZnO. *Angewandte Chemie* **131**, 4346–4351 (2019).
120. Heller, W. & Pugh, T. L. "Steric" stabilization of colloidal solutions by adsorption of flexible macromolecules. *Journal of Polymer Science* **47**, 203–217 (1960).
121. Illum, L., Davis, S. S., Müller, R. H., Mak, E. & West, P. The organ distribution and circulation time of intravenously injected colloidal carriers sterically stabilized with a blockcopolymer - poloxamine 908. *Life Sci* **40**, 367–374 (1987).
122. Schiffelers, R. M. *et al.* Cancer siRNA therapy by tumor selective delivery with ligand-targeted sterically stabilized nanoparticle. *Nucleic Acids Res* **32**, e149–e149 (2004).
123. Elbert, J. *et al.* Surface-Initiated Anionic Polymerization of [1]Silaferrocenophanes for the Preparation of Colloidal Preceramic Materials. *Macromol Rapid Commun* **36**, 597–603 (2015).
124. Asakura, S. & Oosawa, F. On Interaction between Two Bodies Immersed in a Solution of Macromolecules. *J Chem Phys* **22**, 1255–1256 (1954).

125. Asakura, S. & Oosawa, F. Interaction between particles suspended in solutions of macromolecules. *Journal of Polymer Science* **33**, 183–192 (1958).
126. Hogg, R. Bridging Flocculation by Polymers. *KONA Powder and Particle Journal* **30**, 3–14 (2013).
127. Wang, T. *et al.* Roles of functional microbial flocculant in dyeing wastewater treatment: Bridging and adsorption. *J Hazard Mater* **384**, 121506 (2020).
128. Zhai, H., Gunness, P. & Gidley, M. J. Depletion and bridging flocculation of oil droplets in the presence of β-glucan, arabinoxylan and pectin polymers: Effects on lipolysis. *Carbohydr Polym* **255**, (2021).
129. Owen, A. T. *et al.* Using turbulent pipe flow to study the factors affecting polymer-bridging flocculation of mineral systems. *Int J Miner Process* **87**, 90–99 (2008).
130. Zhou, L., Han, Y., Li, W. & Zhu, Y. Study on polymer-bridging flocculation performance of ultrafine specular hematite ore and its high gradient magnetic separation behavior: Description of floc microstructure and flocculation mechanism. *Sep Purif Technol* **276**, 119304 (2021).
131. Koetz, J. & Kosmella, S. *Polyelectrolytes and Nanoparticles*. (Springer Berlin Heidelberg, 2007). doi:10.1007/978-3-540-46382-5.
132. Hayakawa, K., Santerre, J. P. & Kwak, J. C. T. Study of Surfactant-Polyelectrolyte Interactions. Binding of Dodecyl- and Tetradecyltrimethylammonium Bromide by Some Carboxylic Polyelectrolytes. *Macromolecules* **16**, 1642–1645 (1983).
133. Romero-Cano, M. S., Martín-Rodríguez, A. & De las Nieves, F. J. Electrosteric stabilization of polymer colloids with different functionality. *Langmuir* **17**, 3505–3511 (2001).
134. Fritz, G., Schädler, V., Willenbacher, N. & Wagner, N. J. Electrosteric Stabilization of Colloidal Dispersions. *Langmuir* **18**, 6381–6390 (2002).
135. Einarson, M. B. & Berg, J. C. Electrosteric Stabilization of Colloidal Latex Dispersions. *J Colloid Interface Sci* **155**, 165–172 (1993).
136. Alsharif, N. B. *et al.* Dual functionality of ferrocene-based metallopolymers as radical scavengers and nanoparticle stabilizing agents. *Nanoscale* (2023).
137. Zoetebier, B. *et al.* PEG stabilized DNA – poly(ferrocenylsilane) polyplexes for gene delivery. *Chemical Communications* **52**, 7707–7710 (2016).
138. Zhao, W., Brook, M. A. & Li, Y. Design of Gold Nanoparticle-Based Colorimetric Biosensing Assays. *ChemBioChem* **9**, 2363–2371 (2008).
139. Huo, Y. *et al.* A sensitive aptasensor for colorimetric detection of adenosine triphosphate based on the protective effect of ATP-aptamer complexes on unmodified gold nanoparticles. *Biosens Bioelectron* **78**, 315–320 (2016).
140. Shayesteh, O. H. & Ghavami, R. Two colorimetric ampicillin sensing schemes based on the interaction of aptamers with gold nanoparticles. *Microchimica Acta* **186**, 1–10 (2019).
141. Wu, Y., Liu, L., Zhan, S., Wang, F. & Zhou, P. Ultrasensitive aptamer biosensor for arsenic(III) detection in aqueous solution based on surfactant-induced aggregation of gold nanoparticles. *Analyst* **137**, 4171–4178 (2012).
142. Wang, Y., Yang, F. & Yang, X. Colorimetric biosensing of mercury(II) ion using unmodified gold nanoparticle probes and thrombin-binding aptamer. *Biosens Bioelectron* **25**, 1994–1998 (2010).
143. Lee, E. H., Lee, S. K., Kim, M. J. & Lee, S. W. Simple and rapid detection of bisphenol A using a gold nanoparticle-based colorimetric aptasensor. *Food Chem* **287**, 205–213 (2019).

144. Song, K. M., Jeong, E., Jeon, W., Cho, M. & Ban, C. Aptasensor for ampicillin using gold nanoparticle based dual fluorescence-colorimetric methods. *Anal Bioanal Chem* **402**, 2153–2161 (2012).
145. Bai, W. *et al.* Gold nanoparticle-based colorimetric aptasensor for rapid detection of six organophosphorous pesticides. *Environ Toxicol Chem* **34**, 2244–2249 (2015).
146. Bala, R., Sharma, R. K. & Wangoo, N. Development of gold nanoparticles-based aptasensor for the colorimetric detection of organophosphorus pesticide phorate. *Anal Bioanal Chem* **408**, 333–338 (2016).
147. Bala, R. *et al.* Detection of organophosphorus pesticide – Malathion in environmental samples using peptide and aptamer based nanoprobes. *Chemical Engineering Journal* **311**, 111–116 (2017).
148. Bini, A., Minunni, M., Tombelli, S., Centi, S. & Mascini, M. Analytical performances of aptamer-based sensing for thrombin detection. *Anal Chem* **79**, 3016–3019 (2007).
149. He, L. *et al.* Aptasensors for Biomarker Detection. *Journal of Analytical Chemistry 2022 77:12* **77**, 1481–1496 (2022).
150. Hamilton, W. A. & Lee, W. Biocorrosion. *Sulfate-Reducing Bacteria* 243–264 (1995).
151. Geesey, G. What is Biocorrosion? *Biofouling and Biocorrosion in Industrial Water Systems* 155–164 (1991).
152. Beech, I. B. & Sunner, J. Biocorrosion: towards understanding interactions between biofilms and metals. *Curr Opin Biotechnol* **15**, 181–186 (2004).
153. Chandrasatheesh, C. & Jayapriya, J. Biocorrosion. *Bioelectrochemical Interface Engineering* 77–90 (2019).
154. Hao, O. J., Chen, J. M., Huang, L. & Buglass, R. L. Sulfate-reducing bacteria. *Critical Reviews in Environmental Science and Technology* **26**, 155–187 (2009).
155. Zhang, Z. *et al.* A review of sulfate-reducing bacteria: Metabolism, influencing factors and application in wastewater treatment. *J Clean Prod* **376**, 134109 (2022).
156. Videla, H. A. Prevention and control of biocorrosion. *Int Biodeterior Biodegradation* **49**, 259–270 (2002).
157. Guo, J. *et al.* Polymers for combating biocorrosion. *Front Mater* **5**, 10 (2018).
158. Moaref, R., Shahini, M. H., Eivaz Mohammadloo, H., Ramezanzadeh, B. & Yazdani, S. Application of sustainable polymers for reinforcing bio-corrosion protection of magnesium implants–a review. *Sustain Chem Pharm* **29**, 100780 (2022).
159. Abdal-Hay, A., Dewidar, M. & Lim, J. K. Biocorrosion behavior and cell viability of adhesive polymer coated magnesium based alloys for medical implants. *Appl Surf Sci* **261**, 536–546 (2012).
160. Lichter, J. A. *et al.* Substrata mechanical stiffness can regulate adhesion of viable bacteria. *Biomacromolecules* **9**, 1571–1578 (2008).
161. Song, F., Koo, H. & Ren, D. Effects of Material Properties on Bacterial Adhesion and Biofilm Formation. *Journal of Dental Research* **94**, 1027–1034 (2015).
162. Ryzhkov, N. V., Nikitina, A. A., Fratzl, P., Bidan, C. M. & Skorb, E. V. Polyelectrolyte Substrate Coating for Controlling Biofilm Growth at Solid–Air Interface. *Adv Mater Interfaces* **8**, 2001807 (2021).
163. Mehta, H., Kaur, G., Chaudhary, G. R. & Prabhakar, N. Assessment of bio-corrosion inhibition ability of Hafnium based cationic metallosurfactant on iron surface. *Corros Sci* **179**, 109101 (2021).
164. Mehta, H., Kaur, G., Chaudhary, G. R. & Batra, U. Evaluation of bio corrosion-resistant and antifouling properties of gold metallosurfactant monolayer on galvanised steel in simulated sea media inoculated with halophiles. *Corros Sci* **179**, 109102 (2021).

165. Wang, B. *et al.* Direct Loading and Tunable Release of Antibiotics from Polyelectrolyte Multilayers to Reduce Bacterial Adhesion and Biofilm Formation. *Bioconjug Chem* **27**, 1305–1313 (2016).
166. Rodríguez López, A. de L. *et al.* Preventing S. aureus biofilm formation on titanium surfaces by the release of antimicrobial β-peptides from polyelectrolyte multilayers. *Acta Biomater* **93**, 50–62 (2019).
167. Yang, W. J., Neoh, K. G., Kang, E. T., Teo, S. L. M. & Rittschof, D. Polymer brush coatings for combating marine biofouling. *Prog Polym Sci* **39**, 1017–1042 (2014).
168. Xu, G. *et al.* Antifouling, Antimicrobial, and Antibiocorrosion Multilayer Coatings Assembled by Layer-by-layer Deposition Involving Host-Guest Interaction. *Ind Eng Chem Res* **55**, 10906–10915 (2016).
169. Beck, F. Electrodeposition of polymer coatings. *Electrochim Acta* **33**, 839–850 (1988).
170. Luo, X. & Cui, X. T. Electrochemical deposition of conducting polymer coatings on magnesium surfaces in ionic liquid. *Acta Biomater* **7**, 441–446 (2011).
171. Aguirre, J. *et al.* Study of poly(3,4-ethylendioxythiphene) as a coating for mitigation of biocorrosion of AISI 304 stainless steel in natural seawater. *Prog Org Coat* **113**, 175–184 (2017).
172. Rivero, P. J., Redin, D. M. & Rodríguez, R. J. Electrospinning: A Powerful Tool to Improve the Corrosion Resistance of Metallic Surfaces Using Nanofibrous Coatings. *Metals 2020, Vol. 10, Page 350* **10**, 350 (2020).
173. Yuan, S. J., Pehkonen, S. O., Ting, Y. P., Neoh, K. G. & Kang, E. T. Inorganic-organic hybrid coatings on stainless steel by layer-by-layer deposition and surface-initiated atom-transfer-radical polymerization for combating biocorrosion. *ACS Appl Mater Interfaces* **1**, 640–652 (2009).
174. Brinker, C. J. Dip coating. *Chemical Solution Deposition of Functional Oxide Thin Films* **9783211993118**, 233–261 (2013).
175. Kaliyaraj Selva Kumar, A., Zhang, Y., Li, D. & Compton, R. G. A mini-review: How reliable is the drop casting technique? *Electrochem commun* **121**, 106867 (2020).
176. Norrman, K., Ghanbari-Siahkali, A. & Larsen, N. B. 6 Studies of spin-coated polymer films. *Annual Reports Section 'C' (Physical Chemistry)* **101**, 174–201 (2005).
177. Abdal-hay, A., Barakat, N. A. M. & Lim, J. K. Influence of electrospinning and dip-coating techniques on the degradation and cytocompatibility of Mg-based alloy. *Colloids Surf A Physicochem Eng Asp* **420**, 37–45 (2013).
178. Org, W. E. *et al.* A Novel Electrospinning Application for Polyvinyl Chloride Nanofiber Coating Deposition as a Corrosion Inhibitor for Aluminum, Steel, and Brass in Chloride Solutions. *International Journal of Int. J. Electrochem. Sci* **7**, 5962–5976 (2012).
179. Grignard, B. *et al.* Electrospinning of a functional perfluorinated block copolymer as a powerful route for imparting superhydrophobicity and corrosion resistance to aluminum substrates. *Langmuir* **27**, 335–342 (2011).
180. Firouzi, A., Del Gaudio, C., Lamastra, F. R., Montesperelli, G. & Bianco, A. Electrospun polymeric coatings on aluminum alloy as a straightforward approach for corrosion protection. *J Appl Polym Sci* **132**, (2015).
181. Rajasekar, A. & Ting, Y. P. Inhibition of biocorrosion of aluminum 2024 aeronautical alloy by conductive ladder polymer poly(o -phenylenediamine). *Ind Eng Chem Res* **50**, 2040–2046 (2011).
182. Yimyai, T., Thiramanas, R., Phakkeeree, T., Iamsaard, S. & Crespy, D. Adaptive Coatings with Anticorrosion and Antibiofouling Properties. *Adv Funct Mater* **31**, 2102568 (2021).

183. Wang, H., Sun, F., Wang, C., Zhu, Y. & Wang, H. A simple drop-casting approach to fabricate the super-hydrophobic PMMA-PSF-CNFs composite coating with heat-, wear- and corrosion-resistant properties. *Colloid Polym Sci* **294**, 303–309 (2016).
184. Xu, L. & Yamamoto, A. Characteristics and cytocompatibility of biodegradable polymer film on magnesium by spin coating. *Colloids Surf B Biointerfaces* **93**, 67–74 (2012).
185. Conceicao, T. F., Scharnagl, N., Blawert, C., Dietzel, W. & Kainer, K. U. Corrosion protection of magnesium alloy AZ31 sheets by spin coating process with poly(ether imide) [PEI]. *Corros Sci* **52**, 2066–2079 (2010).
186. Ali Syed, J., Lu, H., Tang, S. & Meng, X. Enhanced corrosion protective PANI-PAA/PEI multilayer composite coatings for 316SS by spin coating technique. *Appl Surf Sci* **325**, 160–169 (2015).
187. Norouzi, M. & Afrasiabi Garekani, A. Corrosion protection by zirconia-based thin films deposited by a sol–gel spin coating method. *Ceram Int* **40**, 2857–2861 (2014).

3. Functional grafting of thrombin sensitive aptamer to highly stable poly(ferrocenylsilane)-gold nanoparticles

This section details the results of the synthesis and characterization of gold nanoparticles stabilized by anionic polyelectrolyte $PFS^{-}N_{3(20\ \%)}$, denoted as PFS-AuNP, and subsequent grafting of anti-thrombin aptamers on the PFS-AuNPs. The final assembly is denoted as aptamer-AuNP. An article manuscript based on the results presented in this chapter is currently in preparation and will be submitted for peer review.

Aptamers are widely used in biosensing due to their specific sensitivity toward a plethora of targets. Gold nanoparticle (AuNP) aptasensors are subject to intense research due to the complementary properties of aptamers as sensing elements and AuNPs as transducers. We present herein a novel method for functional coupling of thrombin-specific aptamers to AuNPs via an anionic, redox active poly(ferrocenylsilane) (PFS) polyelectrolyte. The polymer acts as a co-reductant and stabilizer for the AuNPs, provides grafting sites for the aptamer and can be used as a redox sensing element, making the aptamer-PFS-AuNP composite (aptamer-AuNP) a promising model system for future multifunctional sensors. Synthesis of each element of the assembly is described, and the colloidal stability, redox responsiveness, thrombin sensitivity and specificity have been evaluated.

3.1. Introduction

Aptamer-based systems are an important angle of research in the biosensing community[1,2]. Aptamers are single-stranded DNA (ssDNA) sequences of generally 30 or fewer[3] nucleic acid units (although aptamers of as many as 84 units are known[4], particularly when the sequence is not optimized) with a specific sensitivity towards a given target molecule. Usually developed with the method known as systematic evolution of ligands by exponential enrichment (SELEX)[5], these custom-made biomolecules are widely used as bioreceptors for a vast variety of targets such as proteins[6–8], pesticides[9–11], drugs[12–24], heavy metal ions[25–27], and others[28–33].

One of the most frequently studied aptamers is the thrombin-specific oligonucleotide strand. The active conformation of these aptamers is a G-quadruplex[6,34] structure made possible by the abundance of guanine bases in the oligonucleotide chain. The thrombin protein can interact with this structure, forming a strong connection via H-bonds which induces conformational changes of the aptamer chain[6]. Due to this well-understood interaction between the aptamer and its target, thrombin is useful as a model target for the testing of novel aptasensor platforms.

Aptamers are particularly effective when coupled with a simple and relatively cheap transducer like gold nanoparticles (AuNPs)[11,26,35–38]. AuNPs are well-known for the size-dependent absorbance they exhibit due to the localized surface plasmon resonance (LSPR) effect[39]. A very large number of biosensors utilize such an effect in systems based on target-induced aggregation of AuNPs[8,10–14,20,22,25,26,28,32,33,37,38,40–50]. Usually, the detection method in these biosensors is colorimetry, following the red-blue color change upon aggregation of AuNPs, or UV-visible spectroscopy if the nanoparticle concentration is too low to detect the color change with the naked eye.

Biomolecules are known to stabilize metal nanoparticles in colloidal dispersions. It has been shown for both enzymes[51] and aptamers[52–56] that these macromolecules exhibit repulsive steric

effects[57] making colloidal stabilization possible even at very high electrolyte concentrations, at which electrostatic effects are screened. To make full use of such electrosteric stabilization, covalent grafting of the aptamer to the AuNPs is preferred to simple adsorption[28,53]. Coupled with the capacity of anionic PFS polyelectrolytes to provide additional electrosteric stabilization to AuNPs[58], aptamer-PFS-gold nanoparticle hybrids show promise as highly stable colloidal systems even at electrostatic screening conditions.

Poly(ferrocenylsilane)s have been shown to reduce metal salts and stabilize thus-formed metal NPs (MNPs) in electrolyte[58] and in hydrogel matrices[59–61]. The variety of PFS side-chains and the metals used makes these PFS-MNPs potentially useful in several fields for biological[61] and redox sensing[59,62] applications. In this article, we show the synthesis and characterization of an assembly of aptamers and PFS-AuNPs that shows remarkable colloidal stability as well as redox sensitivity owing to the poly(ferrocenylsilane) and thrombin sensitivity through the covalently surface-immobilized aptamer, representing a model of novel multifunctional colloidal sensing platforms.

3.2. Synthesis and characterization

3.2.1. Synthesis of polymers

^{1}H NMR spectra up to and including PFS-I / $N_{3(20\,\%)}$ are in line with previous literature data[5], as shown in the Supplementary Information (Figures 8.1 to 8.3). For the water-soluble polymer $PFS^{-}N_{3(20\,\%)}$, a full peak assignment is presented in the "poly(ferrocenylsilane) synthesis" part of the Materials and Methods section. Additional proof of synthesis is provided by the lack of doubled 1-CH_2 and 2-CH_2 peaks (which would indicate remaining PFS-I repeat units), which, together with the water-solubility of the polymer, indicate full conversion of the iodopropyl moieties.

3.2.2. Gold nanoparticle synthesis

Gold nanoparticles were characterized by UV-visible spectroscopy and transmission electron microscopy (TEM). Results of these experiments are shown on Figure 3.1.

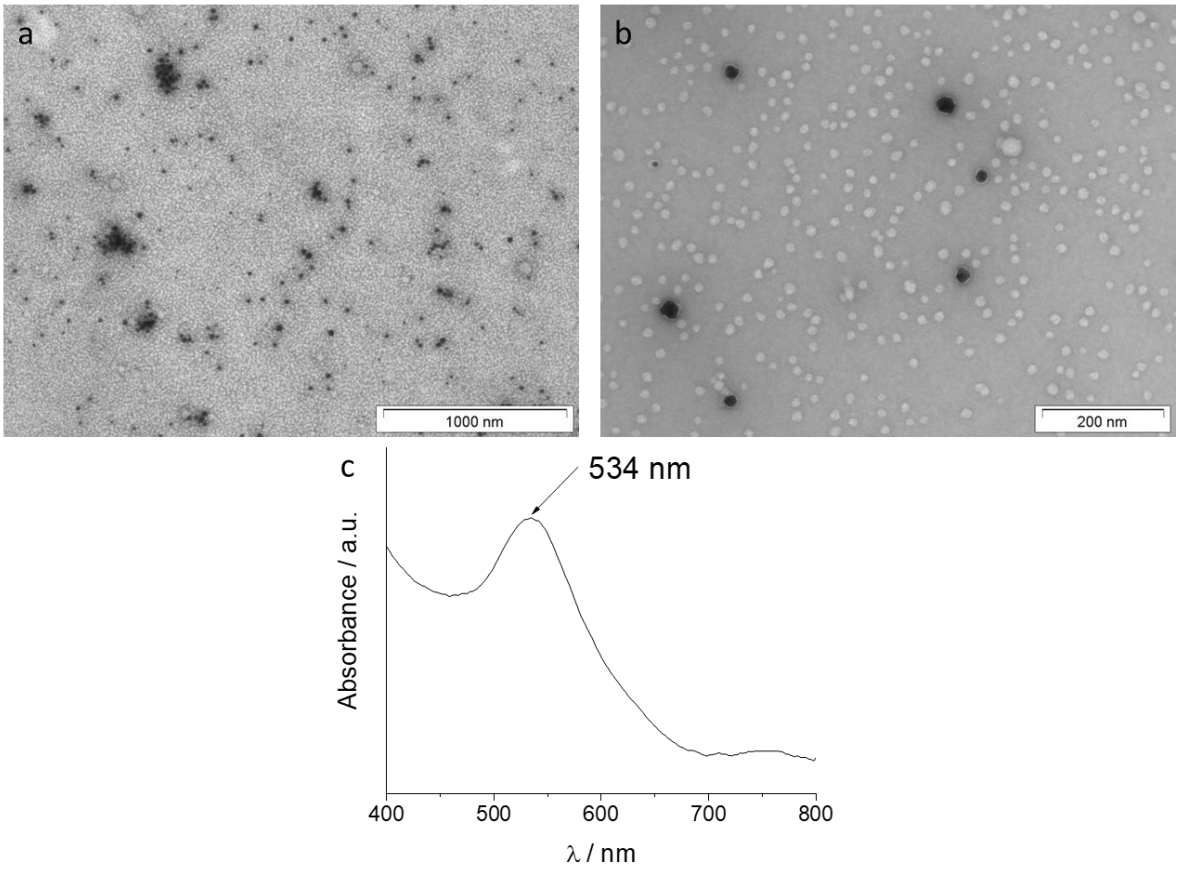

Figure 3.1. TEM images of PFS-AuNPs (a, b). UV-visible spectrum of gold nanoparticle suspension I. The LSPR peak characteristic of gold nanoparticles is indicated with an arrow.

As seen on the TEM images (Figure 3.1. a and b), AuNPs of (27 ± 4.0) nm diameter were successfully synthesized. On Figure 3.1. b, an approximately. 1-2 nm thick PFS-$N_{3(20\,\%)}$ coating is faintly visible around the black gold nanoparticles. Figure 3.1. c shows that the absorbance peak of the AuNPs is at 534 nm, within the expected regime for sub-50 nm gold nanoparticles[63].

3.2.3. Polymer grafting to the anionic poly(ferrocenylsilane) polyelectrolyte

In order to ascertain the applicability of the strain-promoted azide-alkyne cycloaddition for our purposes, we used m-dPEG$_{12}$-DBCO oligomer in a grafting reaction to PFS^{-}N$_{3\ (20\ \%)}$ polymer. The products of this reaction were investigated with ^{1}H and ^{13}C NMR (see Chapter 8, Figures 8.4-8.7), as well as with ATR-FTIR. The results of these experiments are presented in Figure 3.2.

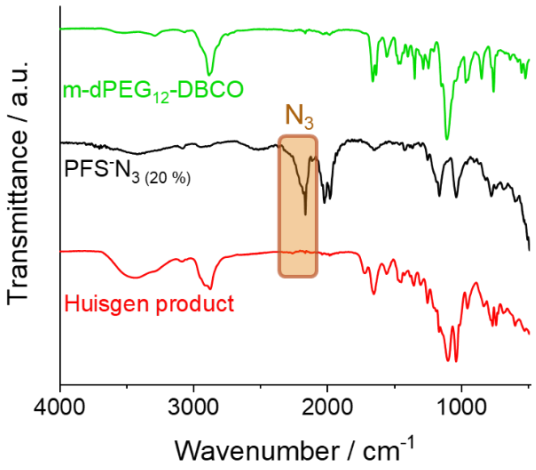

Figure 3.2. ATR-FTIR spectroscopy results on PFS-N$_{3(20\ \%)}$ + m-dPEG$_{12}$-DBCO oligomer grafting experiments. The location of the azide band at 2200 cm^{-1}, the absence of which is used to determine the success of the grafting, is highlighted in orange on the relevant spectra.

As Figure 3.2 shows, the characteristic band of the azide moiety at 2200 cm^{-1} is clearly present in the original polymer, but after reaction with m-dPEG$_{12}$-DBCO either in water or in DMSO, it disappears. This points to successful grafting, a result confirmed by ^{1}H and ^{13}C NMR (See Chapter 8: Supplementary Information, Figures 8.4-8.7). As seen on the ^{1}H NMR spectrum of the reaction product (Figure 8.6), the peaks of the polymer and the m-dPEG$_{12}$-DBCO are

present, but significant changes (widening of peaks, appearance of new ones at 7.90 and 6.65 ppm) can be observed in the DBCO aromatic region (6.5-8 ppm). Additionally, the blue highlighted area of the ^{13}C NMR comparison on Figure 8.7 indicates changes in the aromatic region of the m-dPEG$_{12}$-DBCO, as the azide-alkyne cycloaddition induces changes in the chemical environments of the benzene rings (carbon atoms marked with “a” on Scheme 8.1). Peaks of the newly formed 1,2,3-triazole ring also appear in this region.

3.2.4. Aptamer grafting to the anionic poly(ferrocenylsilane) polyelectrolyte

Grafting of the aptamer to PFS$^{-}N_{3\ (20\ \%)}$ followed a similar principle as the experiments with m-dPEG$_{12}$-DBCO oligomer. However, due to the lower synthesis scale, a different characterization method was necessary.

3.2.5. Enzymatic digestion

Exonucleases, 5’ → 3’ (RecJf) and 3’ → 5’ (Exonuclease I) digestion activity were used for the testing of the Huisgen grafting of the aptamer to PFS or to PFS-AuNP. The premise of this experiment was that both the RecJf and the Exonuclease I enzyme could fully digest aptamer strands that are not attached to the polymer (Scheme 3.1 a), but after the grafting, the 5’ end of the aptamer becomes inaccessible to the RecJf enzyme, thereby hindering digestion, while the 3’ → 5’ digestion activity of the Exonuclease I enzyme remains unaffected (Scheme 3.1 b). By using a fluorescent dye such as SYBR Gold, undigested ssDNA strands become visible in fluorescence spectroscopy measurements (Scheme 3.1 c). The single nucleotides or very short oligomers that remain after a successful enzymatic degradation, however, do not intercalate with SYBR Gold, and thus fluorescence is not observed (Scheme 3.1 d).

Scheme 3.1. Illustration of the dual enzymatic digestion method used to confirm the grafting of the aptamer to PFS and PFS / AuNP samples. Enzymatic digestion of the free aptamer (a). Enzymatic digestion of aptamer-PFS hybrid, hindered at the 5' end (b). Aptamers form fluorescent complexes with SYBR Gold dye (c). Digested fragments do not form fluorescent complexes with SYBR Gold fluorescent dye (d).

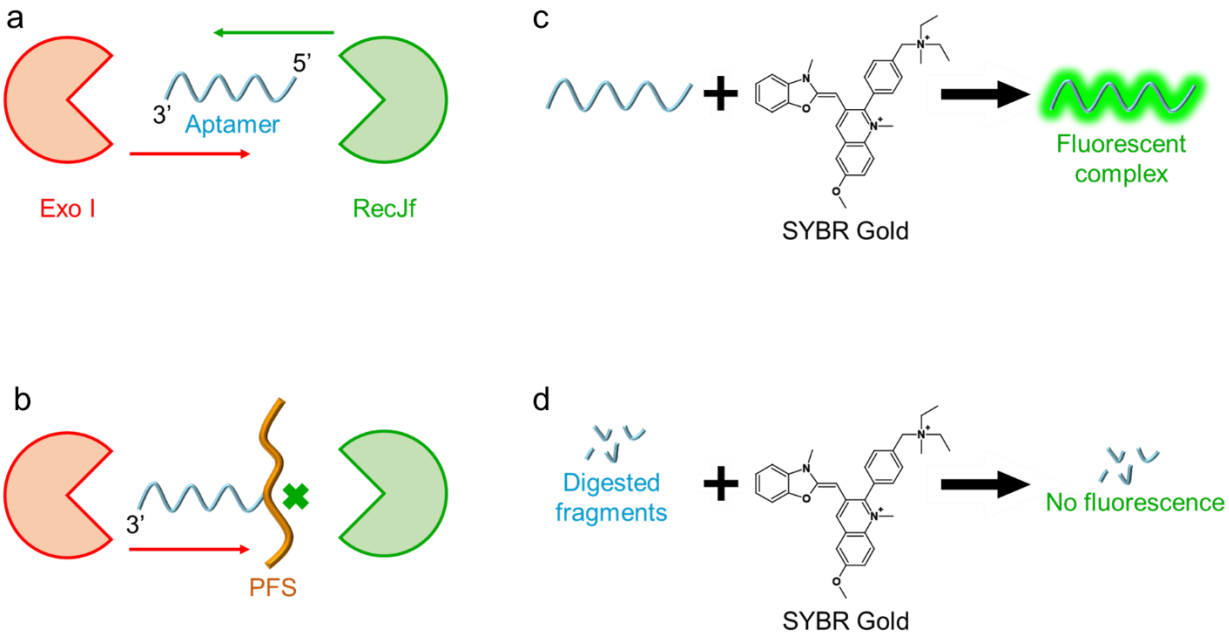

Testing of this principle yielded the data in Figure 3.3. As seen, both the aptamer and the aptamer-PFS samples exhibit high fluorescence, which disappears in both cases upon addition of the Exonuclease I enzyme. However, the fluorescence only decreases upon addition of RecJf to the aptamer sample and remains high upon the enzyme's addition to the PFS-grafted aptamer. This points to successful grafting, as the loss of the RecJf's activity is indicative of the Huisgen-reaction-induced inaccessibility of the 5' end of the aptamer.

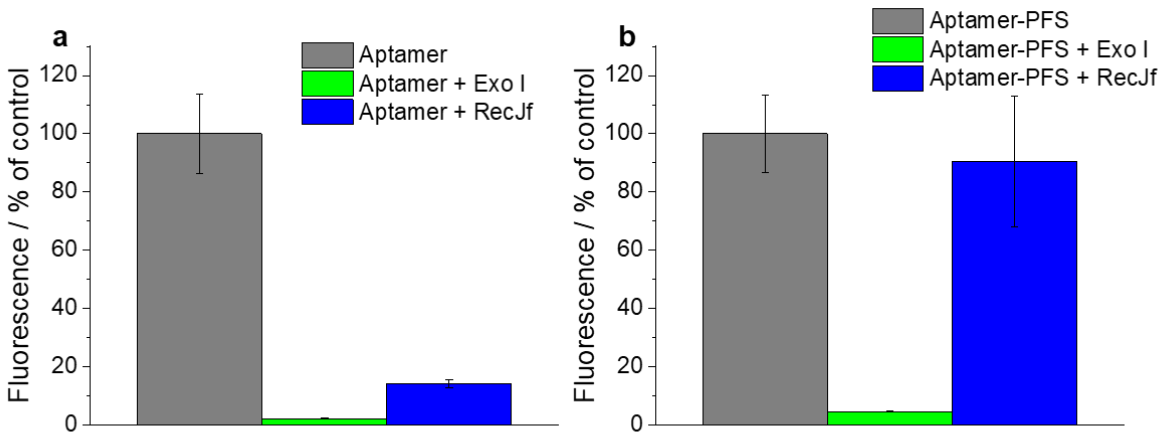

Figure 3.3. Results of the fluorescence measurements of aptamer samples after dual enzymatic digestion without the presence of PFS (a) and with it (b).

3.2.6. Aptamer grafting to poly(ferrocenylsilane)-gold nanoparticles

The process of both the grafting of the aptamer to the PFS-coated AuNPs and the testing of the grafting is akin to the procedures described above, in the aptamer grafting to PFS-$N_{3\ (20\ \%)}$ section. Results obtained from these experiments are shown in Figure 3.4.

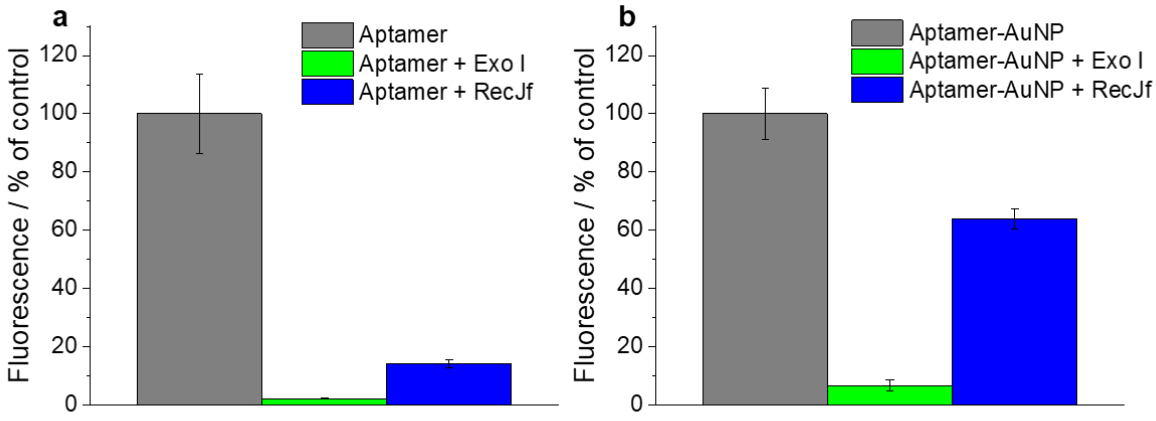

Figure 3.4. Results of fluorescence spectroscopy after dual enzymatic digestion without the presence of PFS-AuNPs (a) and with (b).

As previously observed, the high fluorescence exhibited by the enzyme-free samples disappears upon addition of Exonuclease I. When the aptamer is either grafted to polymers or to AuNPs, hindered digestion in the case of RecJf is observed, indicating successful grafting.

3.3. Colloidal characterization

3.3.1. Colloidal stability of gold nanoparticles

Colloidal stability of PFS-N_3 (20 %) stabilized gold nanoparticles and aptamer-grafted versions thereof (PFS-AuNPs and aptamer-AuNPs, respectively) was assessed by preparing nanoparticle suspensions of different concentrations in 1 M NaCl (Figure 3.5 a). The particle concentrations ranged from 0.2 ppm (1.0 µM Au) to 10 ppm (50.6 µM Au).

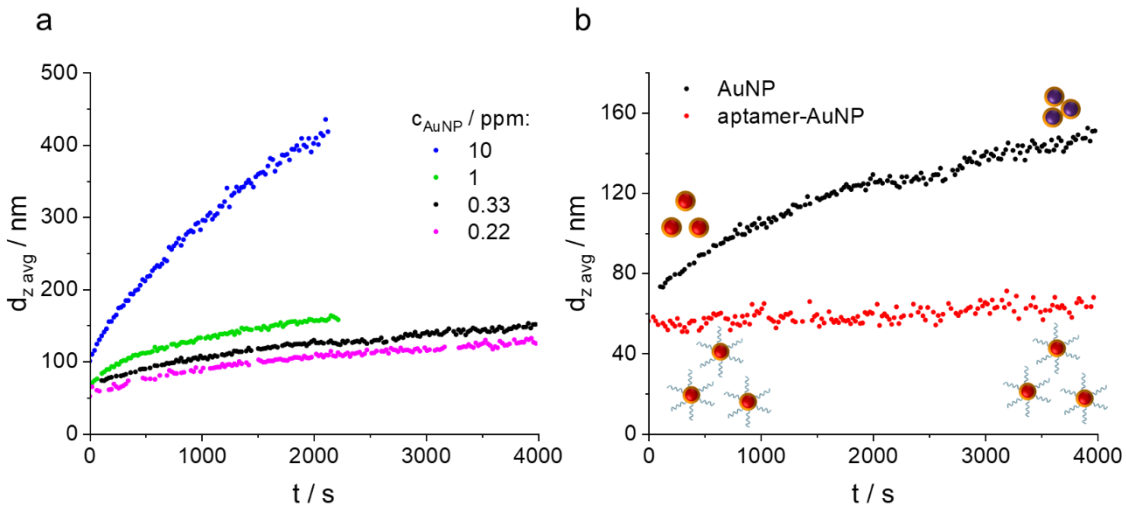

Figure 3.5. Results of DLS stability measurements over time of PFS-AuNPs in 1 M NaCl (a). Comparison of stability of 0.33 ppm aptamer-AuNPs & PFS-AuNPs in 1 M NaCl (b).

Note that under these experimental conditions, the electrostatic repulsion is screened by the dissolved ions and the particles undergo rapid aggregation due to dispersion forces in case of the absence of repulsion of non-electrostatic origin such as steric interaction[64]. It is evident from the data that in concentrations up to at least 1 ppm, diffusion-limited aggregation is significantly slower, with only a twofold increase in diameter over 2000 s in a high ionic-strength dispersion (Figure 3.5 a). This is in line with previous results[62]. Literature data indicate that the aptamer grafting would improve this stability even further via steric effects[55,56]. To test this, we compared the stability of aptamer-grafted PFS-AuNPs to that of PFS-AuNPs without aptamer (Figure 3.5 b). The concentration for these measurements was chosen to be 0.33 ppm (1.67 µM Au, 1 µM aptamer), the same as in the thrombin sensing experiments.

The stability of the nanoparticles was greatly enhanced by the modification of the AuNP surface with aptamers. After 4000 s, 5 times lower size increase was observed in the presence of aptamer than without it. This is explained by the fact that the grafted aptamers are pointing outwards from the AuNP core, forming a steric barrier around the particles.

3.3.2. Redox activity of poly(ferrocenylsilane) and its effects on colloidal stability

In order to probe the redox activity of PFS, we tested the effect of 50 µM $FeCl_3$ on 10 µM PFS-AuNP as well as on 10 µM aptamer-AuNP. As shown on Figure 3.6, the expected aggregation occurred in both cases, but the size of the aptamer-AuNP aggregates (Figure 3.6 b) was an order of magnitude higher than that of the PFS-AuNPs (Figure 3.6 a). This is probably due to the bridging effect of the ssDNA strands. After adding 100 µM vitamin C to the particles, no reduction-driven disaggregation was observed, with the perceived size decrease in the case of the aptamer-AuNPs due to sedimentation (Figure 8.10). These results indicate that the redox activity of the particles is unaffected by the aptamer grafting, rendering the aptamer-AuNPs dual-responsive and opening the door to improving the limit of detection by tuning the oxidation state of PFS.

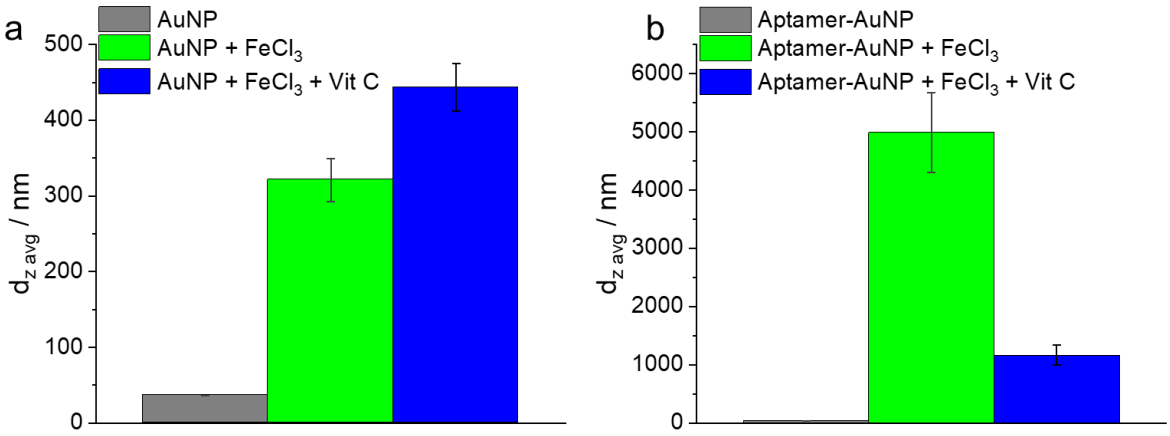

Figure 3.6. Results of redox activity tests on PFS-AuNPs (a) and aptamer-AuNPs (b). c_{Au} = 10 µM in each measurement. In the redox tests, c_{FeCl3} = 50 µM and c_{VitC} = 100 µM.

UV-visible spectrophotometry measurements confirm the results above, as shown in Figure 3.7. The characteristic peak of AuNPs at 540 nm disappears for AuNPs (Figure 3.7 a) as well as for aptamer-AuNPs (Figure 3.7 b).

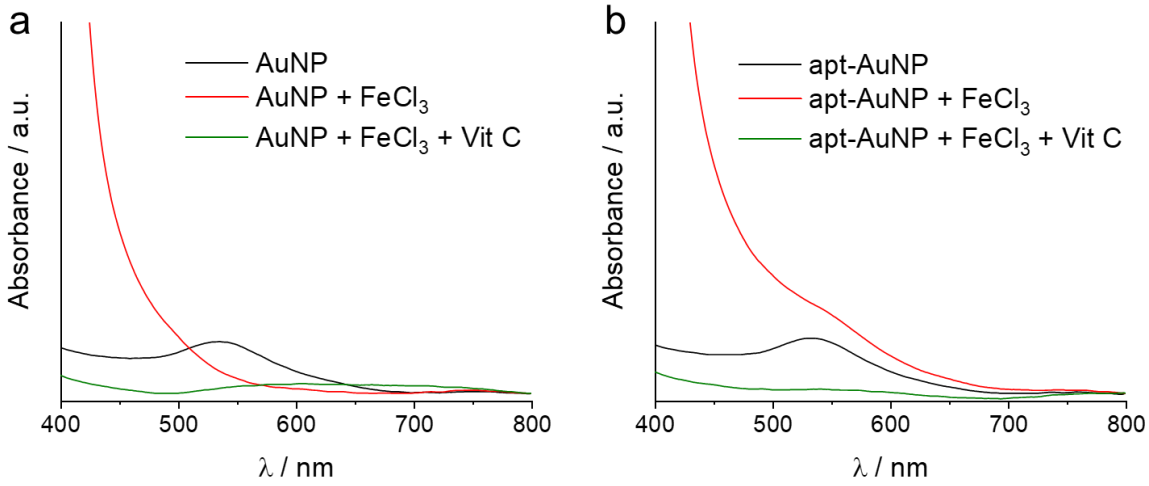

Figure 3.7. UV-visible spectra of redox tests with AuNPs (a) and with aptamer-AuNPs (b).

Stability of the aptamer-AuNPs was also determined against thrombin. Proteins are notorious for adhering to surfaces, and thrombin in particular shows affinity toward polar surfaces[65]. Thus, investigations of the interaction between thrombin and the AuNPs were necessary. In these experiments, the structuring of the aptamer was not performed in order to avoid aptamer-thrombin interaction. Results are shown in Figure 3.8.

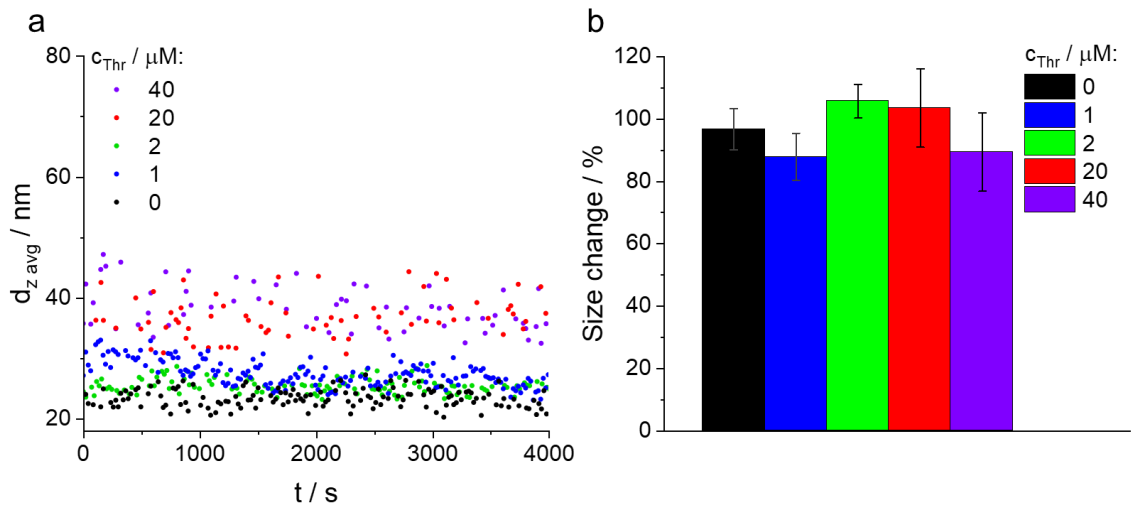

Figure 3.8. Stability tests over time of aptamer-AuNPs as measured by DLS in 1 x interaction buffer (a). Ratio of mean nanoparticle diameter at the end and at the beginning of the measurement (b) (c_{Au} = 0.33 ppm in all samples).

The aptamer-AuNPs were stable in up to at least 40 µM thrombin (Figure 3.8 a), as no significant size change was observed over 4000 s (Figure 3.8 b). As this is beyond the concentrations necessary for the sensing measurements (conducted with c_{Thr} between 0.5-20 µM), the stability of the nanoparticles vs thrombin dose was determined to be suitable for our purposes.

3.4. Characterization of functional grafting

The interaction of the aptamer-AuNPs with thrombin is illustrated on Scheme 3.2. In the first step, the aptamers are straightened by annealing so that they provide maximum steric stabilization to the polymer and to ensure the right conformation for specific interaction with the target[4]. Then the addition of the interaction buffer induces the formation of the active, G-quadruplex conformation. In the last step, thrombin is introduced which destabilizes the nanoparticles by hindering the steric stabilization effect of the aptamers. At high enough

electrolyte concentrations, this results in the aggregation of the aptamer-AuNPs, which can be followed by DLS, UV-visible spectroscopy or by the naked eye, depending on aptamer-AuNP concentration. This interaction, and thus the collapse of the colloidal stability of the AuNPs is specific to thrombin and cannot be induced by other proteins.

Scheme 3.2. Schematic representation of the working principle of the thrombin-specific aptamer-AuNP nanosensor.

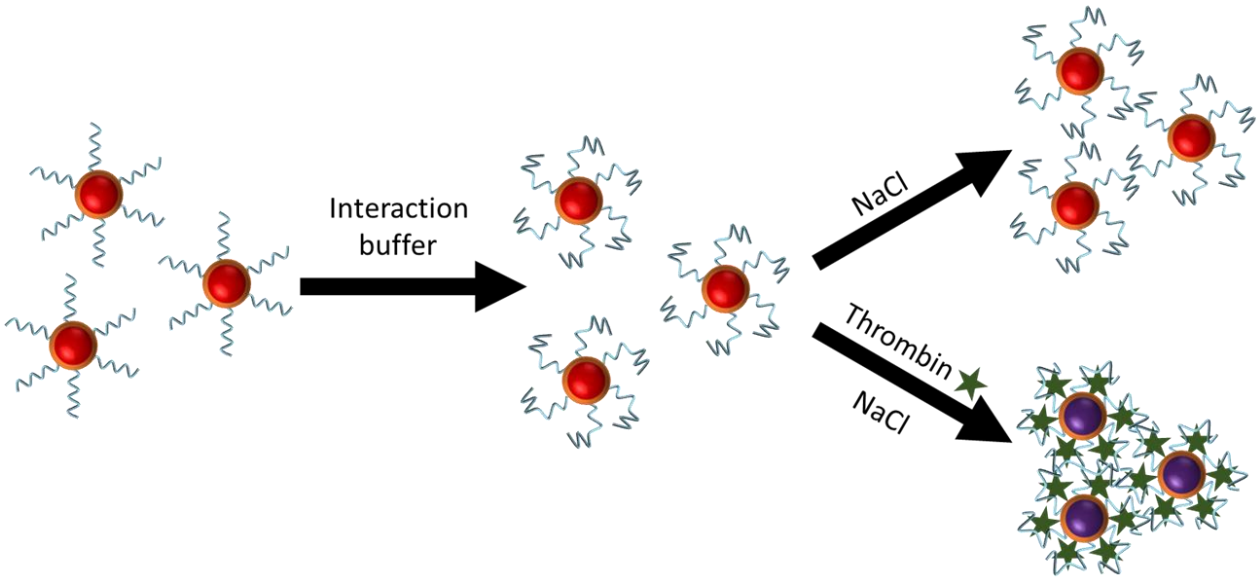

Thrombin interaction experiments were followed by DLS, via the protocol outlined in material and methods. After the structuring of the aptamer in the interaction buffer and thrombin-aptamer interaction, 1 M NaCl was added to the solution and the mixture was left to stand for an hour. Figure 3.9 shows DLS measurement results after this aggregation time.

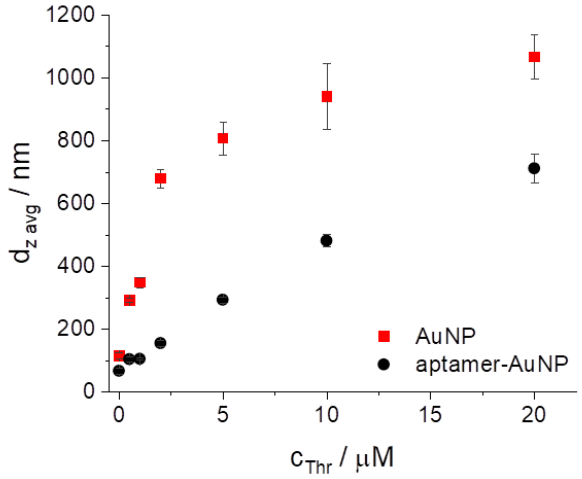

Figure 3.9. DLS results (hydrodynamic diameter) versus thrombin concentration in 1 x buffer and 1 M NaCl (c_{Au} = 0.33 ppm in all samples).

As shown, both the AuNP and the aptamer-AuNP aggregate upon the addition of thrombin. For both systems, an LOD ≤ 0.5 µM was found. The AuNP response was not linear, but for the aptamer-AuNP a linear range between 0 – 10 µM was found.

To demonstrate that the aptamer remains functional after grafting, proof of selectivity was further required. To this end, we repeated the above experiment with beta-lactoglobulin instead of thrombin. This protein does not interact with the thrombin-specific aptamer, thus it can be used as target protein in a control experiment. The LOD and the LOQ of the aptamer-AuNP system for thrombin (0.5 and 2 µM, respectively) were chosen as beta-lactoglobulin concentrations. The results are presented in Figure 3.10.

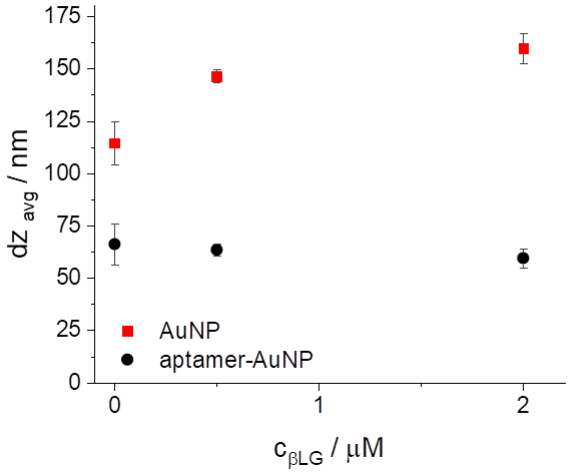

Figure 3.10. Results of beta-lactoglobulin response by DLS in the presence of 1 x buffer and 1 M NaCl. (c_{Au} = 0.33 ppm in all samples)

Accordingly, the non-aptamer-grafted AuNPs show significantly increased diameters in 1 M NaCl if beta-lactoglobulin is present in the system, while the colloidal stability of the aptamer-AuNPs is unaffected. This is probably due to the fact that the aptamers continue providing steric stabilization to the nanoparticles, as they do not interact with this protein. This shows that the aptamer-AuNP system is functional.

3.5. Conclusion

A novel way of functional grafting of aptamers to gold nanoparticles, exhibiting multiple activity (steric stabilization, redox sensitivity, and specific sensitivity to the aptamer target) is described. Water soluble anionic poly(ferrocenylsilane), whose synthesis is also described in detail, plays the role of co-reductant and stabilizer in the AuNP synthesis as well as the grafting site of the aptamer via strain-promoted azide-alkyne cycloaddition. This grafting was thoroughly tested and characterized by multiple methods. The system shows outstanding colloidal stability owing to the steric stabilization provided by the aptamer ssDNA strands.

Redox activity of the poly(ferrocenylsilane) remains after grafting and provides further possibilities for increasing the sensitivity of a future sensor based on this method. The thrombin aptamer remains functional after grafting, and the gold nanoparticles make detection of the aptamer-target interaction possible.

3.6. Materials and Methods

3.6.1. Materials

Potassium tetrachloroaurate ($KAuCl_4$, 99.995 %), dicyclohexano-18-crown-6 (98 %), 1-iodopropane (99 %), dimethyl sulfoxide (DMSO, 99.9 %), potassium azide (KN_3, 99.9 %), sodium chloride (NaCl, 99.5 %), ethylenediaminetetraacetic acid disodium salt dihydrate (EDTA, 99.0 %), deuterium oxide (D_2O, 99.9 % D), dimethyl sulfite (Me_2SO_3, 99 %), tetraethylammonium hydroxide (Et_4NOH, 35 % (w/w) in water), discrete 12-mer polyethylene glycol-dibenzocyclooctyne (m-dPEG$_{12}$-DBCO) and dialysis hoses (benzoylated cellulose, cut-off: 14 kDa) were purchased from Sigma-Aldrich (Saint-Quentin-Fallavier, France). Tetrahydrofuran (THF, anhydrous), methanol (MeOH, technical), magnesium chloride hexahydrate ($MgCl_2$ x 6 H_2O, 99.0 %) and potassium chloride (KCl, 99.5 %) were procured from VWR (Rosny-sous-Bois, France). Deuterated solvents DMSO-d6 (99.8 % D) and benzene-d6 (99.5 % D) were purchased from Eurisotop (Saint-Aubin, France). L-ascorbic acid (vitamin C, 99.5 %) was purchased from Apollo Scientific (Stockport, United Kingdom). Potassium iodide (KI, 99.0 %) was procured from Fluka (Charlotte, USA). Ethanol (EtOH, absolute) was purchased from Merck (Darmstadt, Germany). Tris hydrochloride (Tris-HCl, 98.0 %) was purchased from TCI (Tokyo, Japan). The aptamer sequences (5'-CCAACGGTTGGTGTGGTTGG-3')[66] with dibenzocyclooctyne-triethylene glycol (DBCO-TEG) 5' modifications were purchased from Eurogentec (Seraing, Belgium). Digestion

enzymes Exonuclease I (Exo I from E. Coli, 20 000 U mL^{-1}) and RecJf (30 000 U mL^{-1}) were purchased from New England Biolabs (Evry, France). Thrombin (33.6 kDa, from human plasma) was bought from Roche (Basel, Switzerland). Beta-lactoglobulin (βLG, food-grade, lot#: JE-001-0-415) was purchased from Davisco Foods International (Le Sueur, USA).

3.6.2. Instruments

Nuclear magnetic resonance (NMR) measurements were performed with a Bruker (Billerica, USA) Ultrashield 400 MHz. Attenuated total reflective Fourier transform infrared spectroscopy was performed with a Spectrum Two FTIR spectrometer PerkinElmer (Waltham, USA) with an L1050231 Universal attenuated total reflectance (ATR) accessory. UV-visible and fluorescence spectroscopy was performed with a Tecan Infinite M1000 Pro (Männedorf, Switzerland). Dynamic light scattering (DLS) measurements were conducted with a Malvern Zetasizer Nano ZS (Malvern Panalytical, Malvern, United Kingdom) (laser wavelength: 532 nm), an ALV NIBS/HPPS (ALV-Laser Vertriebsgesellschaft m-b.H., Langen, Germany) (laser wavelength: 633 nm) and an Anton Paar (Graz, Austria) Litesizer 500 (laser wavelength: 658 nm).

3.6.3. Poly(ferrocenylsilane) synthesis

The azide-functionalized anionic polyelectroyte $PFS^{-}/N_{3(20\ \%)}$ was prepared in several synthesis steps, parts of which have been previously published[58,67,68], as shown in Scheme 3.3 below.

Scheme 3.3. Reaction scheme of post-polymerization modification of poly(ferrocenylsilane).

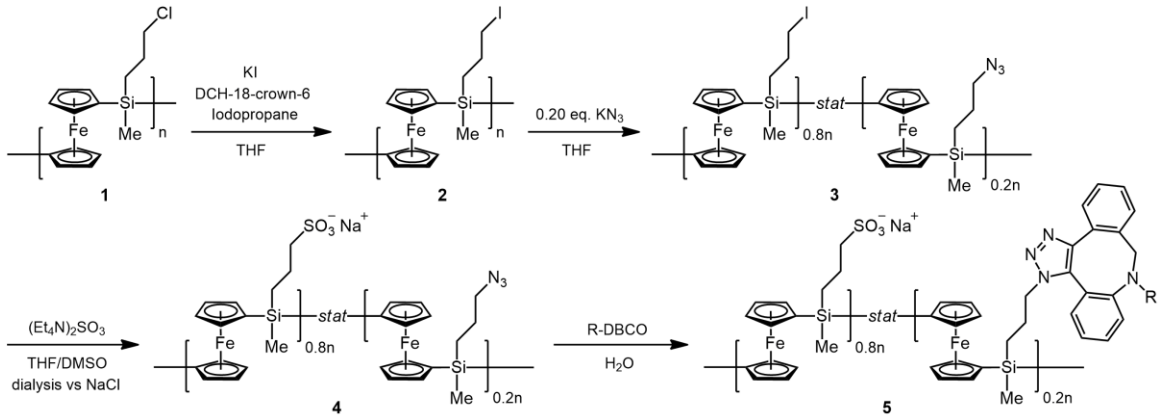

1) ***PFS-Cl***: Poly(ferrocenyl(3-chloropropyl)methylsilane) was synthesized via a previously published[67] procedure in a transition-metal-catalyzed ring-opening polymerization reaction from a precursor ferrocenylsilane containing methyl and chloropropyl-bearing [1] silaferrocenophane monomer side-chains. ^{1}H NMR was performed on the polymer product in benzene-d6 (Figure 8.1). δ: 0.55 ($SiCH_3$) 1.10 (1-CH_2) 1.80 (2-CH_2) 3.25 (3-CH_2) 4.05-4.55 (Fc). The peak at 0.40 ppm represents solvent residues.

2) ***PFS-I***: A mixture in THF containing PFS-Cl (compound 1 in Scheme 3.3), potassium iodide (KI, 1 equivalent (eq) respective to PFS repeat units), dicyclohexano-18-crown-6 (0.25 eq), and iodopropane (0.025 eq) was stirred at 45 °C for at least a week. The polymer was then precipitated in MeOH or EtOH, dried, and subsequently the reaction was continued with the same reagents at 45 °C until completion. The polymer was then precipitated, washed in MeOH and dried under vacuum. ^{1}H NMR was performed on the product in benzene-d6 (Figure 8.2). δ: 0.55 ($SiCH_3$) 1.02 (1-CH_2) 1.85 (2-CH_2) 2.95 (3-CH_2) 4.05-4.55 (Fc). The peak at 0.40 ppm is a solvent residue.

3) ***PFS-I/N$_3$ (20 %)***: PFS-I was dissolved in THF, then 0.2 eq potassium azide (KN_3) dissolved in DMSO was added. The THF:DMSO ratio in the mixture was set to 2:1. After overnight stirring at 45 °C, the resulting polymer was precipitated, washed and dried under vacuum. ^{1}H

NMR was performed in benzene-d6 (Figure 8.3). δ: 0.55 ($SiCH_3$) 0.95 (1-CH_2 (N_3)) 1.02 (1-CH_2 (I)) 1.60 (2-CH_2 (N_3)) 1.85 (2-CH_2 (I)) 2.85 (3-CH_2 (N_3)) 2.95 (3-CH_2 (I)) 4.05-4.50 (Fc). The peak at 0.40 ppm is a solvent residue.

4) ***PFS$^-N_{3\ (20\ \%)}$***: PFS-I/$N_{3\ (20\ \%)}$ was dissolved in THF, then the DMSO solution containing an excess of $(Et_4N)_2SO_3$ (see equation 8.1 and attached description in the Supplementary Information for synthesis of $(Et_4N)_2SO_3$) was added and the solvent ratio of THF:DMSO was set to 5:1. After stirring at 35 °C for 3 days, the mixture was transferred to a dialysis hose and dialyzed against ultrapure water, 3 times against 0.1 M NaCl solution, then against water. The resulting solution was freeze-dried then vacuum dried. ^{1}H NMR was performed in D_2O (Figure 8.4). δ: 0.55 ($SiCH_3$) 0.85 (1-CH_2 (N_3)) 0.95 (1-CH_2) 1.50 (2-CH_2 (N_3)) 1.78 (2-CH_2) 3.90-4.55 (Fc). The peaks at 1.10-1.40; 2.55 and 3.20-3.70 ppm are solvent residues. The 3-CH_2 peaks expected at 3.40 ppm are obscured by the solvent residue signal.

PFS-AuNP*:* 866 µL $PFS^-N_{3\ (20\ \%)}$ stock solution (10.4 mM) and 19 µL vitamin C stock solution (0.47 M) was added to 1.868 mL ultrapure water and the resulting mixture was placed under vigorous stirring for 15 minutes, to achieve full reduction of the PFS. 266 µL of 12.3 mM $KauCl_4$ solution was then added to the PFS-vitamin C solution, which immediately resulted in the color turning deep red, indicating the formation of gold nanoparticles. The solution was stirred for 30 minutes to age the AuNPs, then stored at 4 °C where it remained stable for several months.

5) ***PFS$^-$(m-dPEG$_{12}$-DBCO)$_{(20\ \%)}$****:* $PFS^-N_{3\ (20\ \%)}$ was dissolved in D_2O and 0.2 eq m-$DPEG_{12}$-DBCO, dissolved in D_2O, was added. The reaction was allowed to proceed overnight, then samples for NMR were taken directly from the reaction mixture. The remaining solution was transferred to a dialysis hose (benzoylated cellulose, cut-off: 14 kDa) and dialyzed against ultrapure water 3 times. Thereafter, the polymer was freeze-dried then dried under vacuum in

order to remove all remaining water from the sample. ^{1}H & ^{13}C NMR measurements were performed in DMSO-d6 (Figures 8.6 and 8.7). δ(H): 0.44 ($SiCH_3$); 0.95 (1-CH_2); 1.53 (2-CH_2 (N_3)); 1.71 (d + 2-CH_2); 2.10-2.19 I; 3.10-3.89 (H_2O); 4.02-4.25 (Fc); 5.20 (b); 6.69-8.03 (a+f).

3.6.4. Aptamer grafting

Aptamer-functionalized PFS-AuNP (*PFS^{-}(aptamer-DBCO)$_{(20\ \%)}$*): In a typical grafting procedure, 3.33 µL AuNP (3 mM PFS$^{-}N_{3\ (20\ \%)}$, 1 mM Au) was mixed with 18.08 µL water and 8.59 µL NaCl solution (58.22 mM). To this, 20 µL aptamer (100 µM), with a DBCO-TEG 5' end modification was added and the resulting mixture of aptamer-AuNPs was shaken at 250 rpm, 25 °C overnight.

Enzymatic digestion. In a typical experiment, a 50 µL mixture was prepared that contained either RecJf (225 U) or Exonuclease I (75 U) enzyme and a 1 x concentration of their respective activation buffer, as well as either free aptamer or aptamer-polymer conjugate with a 1 µM aptamer concentration. This mix was shaken at 250 rpm, 37 °C for 30 minutes to complete the enzymatic digestion. Once the digestion time expired, 5-5 µL of each sample was mixed with 25-25 µL of 1.2 x SYBR Gold fluorescent dye in a "stop" solution, meant to stop the enzymatic digestion reaction[69]. Aside from the SYBR Gold, this mixture contained 12 mM Tris-HCl (pH = 7.4), 3.75 mM EDTA and 48 % (v/v) formamide. Fluorescence readings were performed at 545 nm after excitation at 495 nm.

Enzymatic digestion method principle. Exonucleases of 5' → 3' (RecJf) and 3' → 5' (Exonuclease I) digestion activity were used for the testing of the Huisgen grafting of the aptamer to PFS or to PFS-AuNP. The premise of this experiment was explained previously and illustrated with Scheme 3.1.

3.6.5. Colloidal properties, biosensing

Stability tests of AuNPs. The colloidal properties and stability were assessed at (25.0±0.2) °C by dynamic light scattering (DLS) to obtain the hydrodynamic radius. The time-dependent stability in concentrated electrolyte was assessed with the ALV NIBS/HPPS particle sizer. In a typical measurement, a solution was prepared that contained 0.2 – 10 ppm (1.01-50.6 μM) AuNP, and 1 M NaCl. Immediately upon addition of the salt, the mixture was homogenized, and the hydrodynamic diameter was measured with time resolved DLS over at least 30 min.

Redox sensitivity tests. Two sets of mixtures were prepared for testing the redox sensitivity of the nanoparticles, one set with AuNPs and another with aptamer-AuNPs. Gold concentration in each sample was 10 μM. One sample of each set was measured as is. To the second sample, 50 μM $FeCl_3$ was added, and the aggregation was measured with DLS after 10 minutes. The third sample was similarly treated with 50 μM $FeCl_3$, but after 10 minutes, 100 μM vitamin C was also added. These samples were left to stand for another 10 minutes before measurement.

Thrombin interaction with aptamer-AuNPs. 50 μL of 10 μM thrombin-specific aptamer-AuNP (16.7 μM Au) and 16.7 μM Au without aptamer were annealed at 95 °C for 3 minutes, then cooled in ice for another 3 minutes. After the completion of the aptamer structuring steps, the following mixtures were prepared using a 10 x (meaning it had to be diluted tenfold to achieve working concentration) concentrated stock of the aptamer's activation buffer, composed of 200 mM Tris-HCl (pH = 7.5), 1.2 M NaCl, 10 mM $MgCl_2$ and 100 mM KCl, as shown in Table 3.1.

Table 3.1. Solutions prepared for thrombin interaction tests of aptamer-AuNPs.

	AuNP	**Apt-AuNP**	**AuNP + thrombin**	**Apt-AuNP + thrombin**
H_2O	30 µL	30 µL	3.3 µL	3.3 µL
Buffer (10 x)	10 µL	10 µL	10 µL	10 µL
Sample	10 µL	10 µL	10 µL	10 µL

After incubation at room temperature for 30 minutes, 26.7 µL thrombin (150 µM) was added to the "AuNP + thrombin" and "apt-AuNP + thrombin" samples and all four mixtures were incubated for an hour at 25 °C to complete the aptamer-thrombin interaction. Then 50-50 µL of 2 M NaCl solution was added to each sample and the nanoparticles were left to aggregate for an hour before DLS measurements.

3.7. Bibliography

1. Hosseinzadeh, L. & Mazloum-Ardakani, M. Advances in aptasensor technology. *Adv Clin Chem* **99**, 237–279 (2020).
2. Kou, X., Zhang, X., Shao, X., Jiang, C. & Ning, L. Recent advances in optical aptasensor technology for amplification strategies in cancer diagnostics. *Analytical and Bioanalytical Chemistry 2020 412:25* **412**, 6691–6705 (2020).
3. Hasegawa, H. *et al.* Methods for Improving Aptamer Binding Affinity. *Molecules 2016, Vol. 21, Page 421* **21**, 421 (2016).
4. Berkal, M. A. *et al.* Glyphosate–Exonuclease Interactions: Reduced Enzymatic Activity as a Route to Glyphosate Biosensing. *Macromol Biosci* 2200508 (2023).
5. Gopinath, S. C. B. Methods developed for SELEX. *Anal Bioanal Chem* **387**, 171–182 (2007).
6. Deng, B. *et al.* Aptamer binding assays for proteins: The thrombin example—A review. *Anal Chim Acta* **837**, 1–15 (2014).
7. Bini, A., Minunni, M., Tombelli, S., Centi, S. & Mascini, M. Analytical performances of aptamer-based sensing for thrombin detection. *Anal Chem* **79**, 3016–3019 (2007).
8. Jiang, Y. *et al.* Aptamer/AuNP Biosensor for Colorimetric Profiling of Exosomal Proteins. *Angewandte Chemie - International Edition* **56**, 11916–11920 (2017).

9. Bala, R. *et al.* Detection of organophosphorus pesticide – Malathion in environmental samples using peptide and aptamer based nanoprobes. *Chemical Engineering Journal* **311**, 111–116 (2017).
10. Bala, R., Sharma, R. K. & Wangoo, N. Development of gold nanoparticles-based aptasensor for the colorimetric detection of organophosphorus pesticide phorate. *Anal Bioanal Chem* **408**, 333–338 (2016).
11. Bai, W. *et al.* Gold nanoparticle-based colorimetric aptasensor for rapid detection of six organophosphorous pesticides. *Environ Toxicol Chem* **34**, 2244–2249 (2015).
12. Ping, J., He, Z., Liu, J. & Xie, X. Smartphone-based colorimetric chiral recognition of ibuprofen using aptamers-capped gold nanoparticles. *Electrophoresis* **39**, 486–495 (2018).
13. Song, K. M. *et al.* Gold nanoparticle-based colorimetric detection of kanamycin using a DNA aptamer. *Anal Biochem* **415**, 175–181 (2011).
14. Ma, Q., Wang, Y., Jia, J. & Xiang, Y. Colorimetric aptasensors for determination of tobramycin in milk and chicken eggs based on DNA and gold nanoparticles. *Food Chem* **249**, 98–103 (2018).
15. Chen, A. *et al.* High sensitive rapid visual detection of sulfadimethoxine by label-free aptasensor. *Biosens Bioelectron* **42**, 419–425 (2013).
16. Yan, Z. *et al.* A 'signal-on'" aptasensor for simultaneous detection of chloramphenicol and polychlorinated biphenyls using multi-metal ions encoded nanospherical brushes as tracers'. *Biosens Bioelectron* **74**, 718–724 (2015).
17. Abnous, K., Danesh, N. M., Ramezani, M., Emrani, A. S. & Taghdisi, S. M. A novel colorimetric sandwich aptasensor based on an indirect competitive enzyme-free method for ultrasensitive detection of chloramphenicol. *Biosens Bioelectron* **78**, 80–86 (2016).
18. Kim, Y. S. *et al.* A novel colorimetric aptasensor using gold nanoparticle for a highly sensitive and specific detection of oxytetracycline. *Biosens Bioelectron* **26**, 1644–1649 (2010).
19. Ramezani, M., Mohammad Danesh, N., Lavaee, P., Abnous, K. & Mohammad Taghdisi, S. A novel colorimetric triple-helix molecular switch aptasensor for ultrasensitive detection of tetracycline. *Biosens Bioelectron* **70**, 181–187 (2015).
20. Luo, Y. *et al.* A novel colorimetric aptasensor using cysteamine-stabilized gold nanoparticles as probe for rapid and specific detection of tetracycline in raw milk. *Food Control* **54**, 7–15 (2015).
21. Zhou, N. *et al.* Selection and identification of streptomycin-specific single-stranded DNA aptamers and the application in the detection of streptomycin in honey. *Talanta* **108**, 109–116 (2013).
22. Emrani, A. S. *et al.* Colorimetric and fluorescence quenching aptasensors for detection of streptomycin in blood serum and milk based on double-stranded DNA and gold nanoparticles. *Food Chem* **190**, 115–121 (2016).
23. Danesh, N. M., Ramezani, M., Emrani, A. S., Abnous, K. & Taghdisi, S. M. A novel electrochemical aptasensor based on arch-shape structure of aptamer-complimentary strand conjugate and exonuclease I for sensitive detection of streptomycin. *Biosens Bioelectron* **75**, 123–128 (2016).
24. Song, K. M., Jeong, E., Jeon, W., Cho, M. & Ban, C. Aptasensor for ampicillin using gold nanoparticle based dual fluorescence-colorimetric methods. *Anal Bioanal Chem* **402**, 2153–2161 (2012).
25. Wang, Y., Yang, F. & Yang, X. Colorimetric biosensing of mercury(II) ion using unmodified gold nanoparticle probes and thrombin-binding aptamer. *Biosens Bioelectron* **25**, 1994–1998 (2010).

26. Li, L., Li, B., Qi, Y. & Jin, Y. Label-free aptamer-based colorimetric detection of mercury ions in aqueous media using unmodified gold nanoparticles as colorimetric probe. *Anal Bioanal Chem* **393**, 2051–2057 (2009).
27. Wu, Y., Liu, L., Zhan, S., Wang, F. & Zhou, P. Ultrasensitive aptamer biosensor for arsenic(III) detection in aqueous solution based on surfactant-induced aggregation of gold nanoparticles. *Analyst* **137**, 4171–4178 (2012).
28. Cheng, R., Liu, S., Shi, H. & Zhao, G. A highly sensitive and selective aptamer-based colorimetric sensor for the rapid detection of PCB 77. *J Hazard Mater* **341**, 373–380 (2018).
29. Li, F. *et al.* Adenosine detection by using gold nanoparticles and designed aptamer sequences. *Analyst* **134**, 1355–1360 (2009).
30. Mao, Y. *et al.* A simple and sensitive aptasensor for colorimetric detection of adenosine triphosphate based on unmodified gold nanoparticles. *Talanta* **168**, 279–285 (2017).
31. Jo, M. *et al.* Development of single-stranded DNA aptamers for specific Bisphenol a detection. *Oligonucleotides* **21**, 85–91 (2011).
32. Lee, E. H., Lee, S. K., Kim, M. J. & Lee, S. W. Simple and rapid detection of bisphenol A using a gold nanoparticle-based colorimetric aptasensor. *Food Chem* **287**, 205–213 (2019).
33. Feng, J., Shen, Q., Wu, J., Dai, Z. & Wang, Y. Naked-eyes detection of Shigella flexneri in food samples based on a novel gold nanoparticle-based colorimetric aptasensor. *Food Control* **98**, 333–341 (2019).
34. Zhang, L. *et al.* Photodriven Regeneration of G-Quadruplex Aptasensor for Sensitively Detecting Thrombin. *Anal Chem* **92**, 7419–7424 (2020).
35. Zhao, V. X. T., Wong, T. I., Zheng, X. T., Tan, Y. N. & Zhou, X. Colorimetric biosensors for point-of-care virus detections. *Mater Sci Energy Technol* **3**, 237–249 (2020).
36. Liu, B., Zhuang, J. & Wei, G. Recent advances in the design of colorimetric sensors for environmental monitoring. *Environ Sci Nano* **7**, 2195–2213 (2020).
37. Zheng, Y., Wang, Y. & Yang, X. Aptamer-based colorimetric biosensing of dopamine using unmodified gold nanoparticles. *Sens Actuators B Chem* **156**, 95–99 (2011).
38. Chang, C. C. *et al.* Gold nanoparticle-based colorimetric strategies for chemical and biological sensing applications. *Nanomaterials* **9**, 1–24 (2019).
39. Mayer, K. M. & Hafner, J. H. Localized surface plasmon resonance sensors. *Chem Rev* **111**, 3828–3857 (2011).
40. Chen, Z. *et al.* Colorimetric detection of potassium ions using aptamer-functionalized gold nanoparticles. *Anal Chim Acta* **787**, 189–192 (2013).
41. Yang, C., Wang, Y., Marty, J. L. & Yang, X. Aptamer-based colorimetric biosensing of Ochratoxin A using unmodified gold nanoparticles indicator. *Biosens Bioelectron* **26**, 2724–2727 (2011).
42. Ma, X., Song, L., Zhou, N., Xia, Y. & Wang, Z. A novel aptasensor for the colorimetric detection of S. typhimurium based on gold nanoparticles. *Int J Food Microbiol* **245**, 1–5 (2017).
43. Liu, J. & Lu, Y. Preparation of aptamer-linked gold nanoparticle purple aggregates for colorimetric sensing of analytes. *Nat Protoc* **1**, 246–252 (2006).
44. Wei, H., Li, B., Li, J., Wang, E. & Dong, S. Simple and sensitive aptamer-based colorimetric sensing of protein using unmodified gold nanoparticle probes. *Chemical Communications* 3735–3737 (2007).
45. Liu, J. *et al.* Improving sensitivity of gold nanoparticle based fluorescence quenching and colorimetric aptasensor by using water resuspended gold nanoparticle. *Biosens Bioelectron* **52**, 265–270 (2014).

46. Huang, C. C., Huang, Y. F., Cao, Z., Tan, W. & Chang, H. T. Aptamer-modified gold nanoparticles for colorimetric determination of platelet-derived growth factors and their receptors. *Anal Chem* **77**, 5735–5741 (2005).
47. Xie, Y. *et al.* Sensitive colorimetric detection for lysozyme based on the capture of a fixed thiol-aptamer on gold nanoparticles. *New Journal of Chemistry* **43**, 4531–4538 (2019).
48. Borghei, Y. S. *et al.* Visual detection of cancer cells by colorimetric aptasensor based on aggregation of gold nanoparticles induced by DNA hybridization. *Anal Chim Acta* **904**, 92–97 (2016).
49. Wu, Y. *et al.* Cationic polymers and aptamers mediated aggregation of gold nanoparticles for the colorimetric detection of arsenic(III) in aqueous solution. *Chemical Communications* **48**, 4459–4461 (2012).
50. Li, X. *et al.* A simple highly sensitive and selective aptamer-based colorimetric sensor for environmental toxins microcystin-LR in water samples. *J Hazard Mater* **304**, 474–480 (2016).
51. Savin, R., Blanck, C., Benzaamia, N. O. & Boulmedais, F. Optimization of Nanohybrid Biosensors Based on Electro-Crosslinked Tannic Acid Capped Nanoparticles/Enzyme. *Molecules* **27**, 3309 (2022).
52. Mirau, P. A. *et al.* Structured DNA Aptamer Interactions with Gold Nanoparticles. *Langmuir* **34**, 2139–2146 (2018).
53. Sun, C., Zhao, S., Qu, F., Han, W. & You, J. Determination of adenosine triphosphate based on the use of fluorescent terbium(III) organic frameworks and aptamer modified gold nanoparticles. *Microchimica Acta* **187**, 1–9 (2020).
54. Xiao, Z. & Farokhzad, O. C. Aptamer-functionalized nanoparticles for medical applications: Challenges and opportunities. *ACS Nano* **6**, 3670–3676 (2012).
55. Zhao, W., Brook, M. A. & Li, Y. Design of Gold Nanoparticle-Based Colorimetric Biosensing Assays. *ChemBioChem* **9**, 2363–2371 (2008).
56. Zhao, W., Chiuman, W., Brook, M. A. & Li, Y. Simple and Rapid Colorimetric Biosensors Based on DNA Aptamer and Noncrosslinking Gold Nanoparticle Aggregation. *ChemBioChem* **8**, 727–731 (2007).
57. Raghavan, S. R., Fritz, G. & Kaler, E. W. Wormlike micelles formed by synergistic self-assembly in mixtures of anionic and cationic surfactants. *Langmuir* **18**, 3797–3803 (2002).
58. Song, J. *et al.* Poly(ferrocenylsilane) electrolytes as a gold nanoparticle foundry: “two-in-one” redox synthesis and electrosteric stabilization, and sensing applications. *Nanoscale* **9**, 19255–19262 (2017).
59. Feng, X., Hempenius, M. A. & Vancso, G. J. Metal Nanoparticle Foundry with Redox Responsive Hydrogels. *Macromol Chem Phys* **219**, 1800223 (2018).
60. Halmagyi, T., Hao, J., Hempenius, M. A. & Vancso, G. J. Poly(ferrocenylsilane) Hydrogels as a Foundry for Metal Nanoparticle Synthesis by Direct Reduction of Electrolytes via a Catalytic Route. *ACS Appl Nano Mater* **5**, 8868–8874 (2022).
61. Sui, X. *et al.* Poly(N -isopropylacrylamide)–poly(ferrocenylsilane) dual-responsive hydrogels: synthesis, characterization and antimicrobial applications. *Polym Chem* **4**, 337–342 (2012).
62. Song, J. *et al.* Poly(ferrocenylsilane) electrolytes as a gold nanoparticle foundry: ‘two-in-one’ redox synthesis and electrosteric stabilization, and sensing applications. *Nanoscale* **9**, 19255–19262 (2017).
63. Haiss, W., Thanh, N. T. K., Aveyard, J. & Fernig, D. G. Determination of size and concentration of gold nanoparticles from UV-Vis spectra. *Anal Chem* **79**, 4215–4221 (2007).

64. Holthoff, H., Egelhaaf, S. U., Borkovec, M., Schurtenberger, P. & Sticher, H. Coagulation rate measurements of colloidal particles by simultaneous static and dynamic light scattering. *Langmuir* **12**, 5541–5549 (1996).
65. Alibeik, S., Zhu, S. & Brash, J. L. Surface modification with PEG and hirudin for protein resistance and thrombin neutralization in blood contact. *Colloids Surf B Biointerfaces* **81**, 389–396 (2010).
66. Mir, M., Jenkins, A. T. A. & Katakis, I. Ultrasensitive detection based on an aptamer beacon electron transfer chain. *Electrochem commun* **10**, 1533–1536 (2008).
67. Hempenius, M. A., Brito, F. F. & Vancso, G. J. Synthesis and characterization of anionic and cationic poly(ferrocenylsilane) polyelectrolytes. *Macromolecules* **36**, 6683–6688 (2003).
68. Zhang, K., Zhang, M., Feng, X., Hempenius, M. A. & Vancso, G. J. Switching Light Transmittance by Responsive Organometallic Poly(ionic liquid)s: Control by Cross Talk of Thermal and Redox Stimuli. *Adv Funct Mater* **27**, 1–8 (2017).
69. Alkhamis, O., Yang, W., Farhana, R., Yu, H. & Xiao, Y. Label-free profiling of DNA aptamer-small molecule binding using T5 exonuclease. *Nucleic Acids Res* **48**, e120–e120 (2020).

4. Colloidal stability of poly(ferrocenylsilane)-stabilized amidine latex nanoparticles

This chapter details various works undertaken to further our understanding of the interaction of PFS polyelectrolytes and various nanoparticles in colloidal dispersion. This section is adapted from the following work: Nizar B. Alsharif, Tibor Gergo Halmagyi, Mark A. Hempenius, G. Julius Vancso, Corinne Nardin and Istvan Szilagyi: Dual functionality of ferrocene-based metallopolymers as radical scavengers and nanoparticle stabilizing agents, Nanoscale (2023)[1].

4.1. Introduction

Poly(ferrocenylsilane)s (PFSs) has proved to be a suitable material for the preparation of metallic nanoparticles due to its redox-sensitive nature, which is attributed to the ferrocene group present in the main chain that can be oxidized to ferrocenium[2,3]. The obtained PFS-nanoparticle systems often possess excellent redox sensitivity and reversible redox kinetics, while a color change response that accompanies the redox process enables the use of the PFS-functionalized metallic nanoparticles as building blocks in colorimetric detection[4]. Besides, the redox properties stimulated researchers to design PFS films on planar silicon, gold, or glassy carbon surfaces to develop electrochemical sensors exhibiting high sensitivity and stable responses to target molecules such as ascorbic acid (AA)[5,6]. Apart from the above-mentioned advantageous redox features utilized in sensing, there are two additional important potential uses of PFS, which are worthy of further exploration. These include their effect on the colloidal stability of particle dispersions and possible radical scavenging activity.

On the one hand, it was proved that PFS can serve as a stabilizer for gold particles[4]. Since PFS can be considered as a polymer of significant line charge density (i.e., a so-called polyelectrolyte), the explanation of the origin of surface forces induced by PFS adsorption seems straightforward. Accordingly, electrostatic repulsive forces between PFS-coated charged surfaces are predicted by the classical theory of Derjaguin, Landau, Verwey, and Overbeek (DLVO)[7–9], in terms of the repulsion by the overlapping electrical double layers. This theory also assumes the constant presence of attractive van der Waals forces, while non-DLVO attraction may occur via patch-charge[10,11] or bridging interactions[12,13]. In addition, partially adsorbed polymer chains dangling into the solution from the surface may establish steric repulsion between approaching particles[14–16]. Such interparticle forces were reported in various particle-polyelectrolyte systems in the past decades[12–16]. Beyond some pioneering works with

gold-PFS composites[4,17], the effect of PFS adsorption on the colloidal stability of dispersed nanoparticles has not been investigated. To tackle this issue, the effect of the pH, ionic strength, as well as the dose of $PFS^{-}COOH_{(15\,\%)}$ on p-AL composites was systematically investigated.

4.2. Colloidal characterization

4.2.1. Colloidal characterization of amidine latex particles

The pH-dependent zeta potential and hydrodynamic radius data of amidine latex (AL) particles were determined with laser doppler electrophoresis (LDE) and DLS, respectively (Figure 4.1 a). AL forms highly stable dispersions in acidic, neutral, and alkaline pH regimes, as evidenced by the nearly constant hydrodynamic radii (36.6±0.3) nm values. Despite the different principle of measurement, this value is in relatively good agreement with the TEM radius (34 nm) reported by the manufacturer in the dry state. As DLS measures hydrodynamic radius derived from the diffusion coefficient of the particles in a colloidal suspension, higher size values are expected compared to those achieved with microscopy. The zeta potential data shows that AL undergoes surface charge reduction as the pH is increased. This is explained by the progressive deprotonation of the positively charged amidine surface groups with increasing pH. The AL NPs still maintain significant positive surface charge even at pH 11, despite the likely large-scale deprotonation, preventing aggregation. Aqueous AL dispersions therefore owe their stability to strong DLVO-type repulsive forces. High surface charge giving rise to robust stability is typical for similar latex particle systems.[18–22]

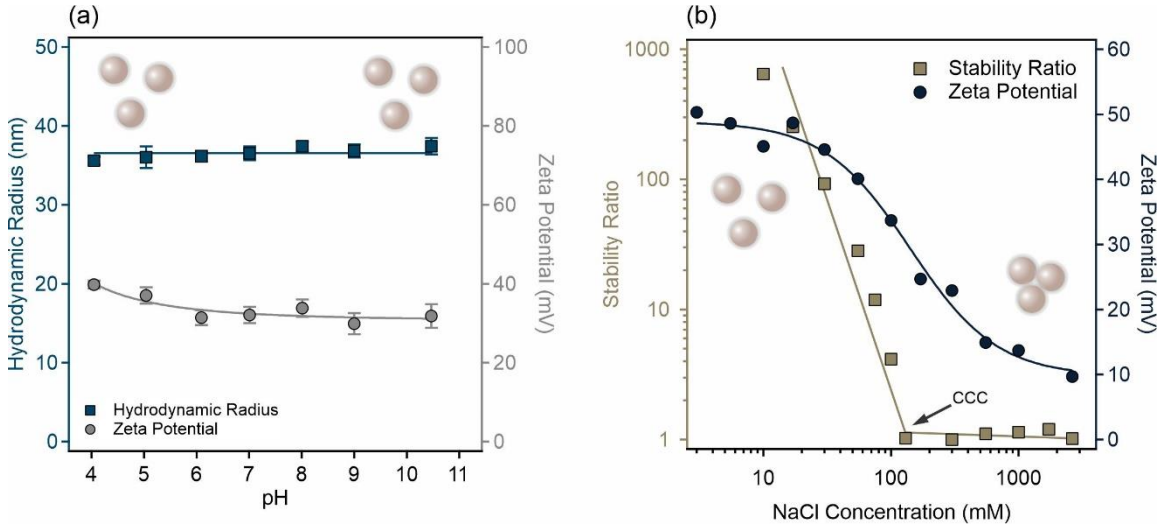

Figure 4.1. Characterization of colloidal amidine latex nanoparticles. (a) Hydrodynamic radius and zeta potential of AL as a function of pH. (b) Stability ratio and zeta potential values of AL at different NaCl concentrations at pH 4.0. All lines are for eye-guidance purposes, except in (a) where the hydrodynamic radius line is a linear fit. c_{AL} = 25 mg L^{-1}; ionic strength: 1.0 mM.

DLS measurements as a function of time have a scientific basis as a method for aggregation rate determination of colloids and especially nanoparticle dispersions.[23] DLS allows investigation of early stages of particle aggregation, allowing for the determination of interparticle forces playing a role in the stabilization of a given colloidal system[24]. In the time-resolved DLS experiments, we assessed the salt tolerance of AL dispersions in a wide ionic strength range (1 mM to 3 M), adjusted by NaCl. Figure 4.1 b shows that the expected gradual decrease of stability ratios – and, therefore, increasing aggregation rates – with increasing NaCl concentration does indeed occur, with total destabilization of the dispersion, or the critical coagulation concentration (CCC), at 130 mM NaCl, which is in line with values measured for similar systems in monovalent electrolyte solution[25–28].

At low c_{NaCl}, the stability ratio remains high, particle aggregation is slow, and the system is stable. This is in line with the zeta potential data in Figure 4.1 a, as high zeta potential values give rise to strong electrostatic repulsive forces and high stability ratios. On the other hand, at high salt levels approaching or surpassing the CCC, the low zeta potential results in fast aggregation, with stability ratio values close to 1.

The DLVO theory explains this phenomenon[7,18,19], as increasing the ionic strength of the solution leads to reduction of the width of the electrostatic double layer (EDL). The screening of the surface charges – and thus the decrease of the absolute value of the zeta potential – results in weakened repulsive electrostatic forces and a decrease of the kinetic stabilizing effect described by the theory as the repulsion brought on by the overlap of EDLs. As the EDLs become thinner or even disappear completely, this overlap becomes more difficult or even impossible, allowing for ever closer approach and eventual rapid aggregation of particles under the influence of van der Waals attractive forces.

4.2.2. Functionalization of amidine latex particles with anionic poly(ferrocenylsilane) polyelectrolyte

The surface of the positively charged AL NPs was modified by adsorption of anionic polyelectrolyte $PFS^{-}COOH_{(15\ \%)}$, with the intent of "flipping" the surface charge, producing negatively charged AL-$PFS^{-}COOH_{(15\ \%)}$ nanoparticles in a stable colloidal dispersion. The colloidal stability vs polyelectrolyte loading relationship was observed via time-dependent size and zeta potential measurements in AL NP samples with a range of $PFS^{-}COOH_{(15\ \%)}$ concentration. The zeta potential and stability ratio data are shown in Figure 4.2.

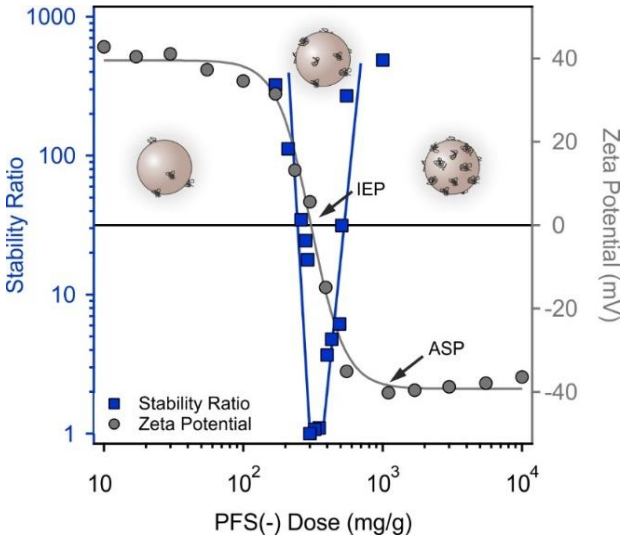

Figure 4.2. Effect of adsorption of different PFS-COOH$_{(15\ \%)}$ doses (mg PFS / g AL) on zeta potential and stability ratio of AL NPs. The lines are for eye guidance purposes only. c_{AL} = 25 mg L^{-1}; pH = 4.0 and ionic strength: 1.0 mM.

AL particles hold a high positive surface charge, preventing aggregation at low PFS-COOH$_{(15\ \%)}$ doses. Increasing the polyelectrolyte concentration leads to a decrease in the zeta potential and the stability ratio. Zeta potential plummets to zero as the charges of the AL NPs and the polyelectrolyte balance each other out at around 200 mg g^{-1} dose, or the isoelectric point (IEP). As a result, the stability ratio falls to one at this dose, leading to rapid aggregation driven by van der Waals forces and the lack of DLVO-type stabilizing interactions. Applying doses over the IEP leads to negative charges being dominant on the nanoparticle surface, increasing once again the absolute value of the zeta potential. This leads to the increase of the stability ratio up to 1000 mg g^{-1} dose, where the zeta potential reaches a constant value at the onset of the adsorption saturation plateau (ASP), at which the nanoparticle surface becomes saturated with PFS-COOH$_{(15\ \%)}$. At the ASP onset the loading is optimal, as the AL NPs possess a high negative surface charge, leading to maximal stabilization. Therefore, a PFS-COOH$_{(15\ \%)}$ dose of 800 mg g^{-1} (denoted as p-AL) was selected for further measurements.

As widely proven in literature on charged polymer-particle systems[29–33]non-DLVO-type forces (e.g. repulsive steric interactions, bridging and depletion attraction) play a role in the colloidal stability of such systems. Nevertheless, the data shown in Figure 4.2 do not underline the presence of such forces unambiguously, but rather point to the domination of DLVO-type interactions.

4.2.3. Charge and aggregation in poly(ferrocenylsilane)-amidine latex colloids: effect of pH and salt

To test the effect of PFS-$COOH_{(15\ \%)}$ loading on the AL NPs' colloidal stability, the pH-dependence of the zeta potential of p-AL nanoparticles. Figure 4.3 a shows that both the zeta potential and the hydrodynamic size remain constant over a wide pH range. The zeta potential was maintained at –(37.0±0.6) mV throughout the pH range 3-11, as the sulfonate groups (Scheme 4.1 in the Materials and Methods section) render the PFS a strong anionic polyelectrolyte. The average hydrodynamic radius of p-AL was (71.2±0.2) nm under these conditions. Previously we showed that the bare AL has a size of (36.6±0.3) nm (Figure 4.1 a). The increase in size can be attributed to two interfacial phenomena. First, the adsorbed PFS-$COOH_{(15\ \%)}$ polymeric chains extending into the bulk around AL led to an increase in the hydrodynamic sphere and thus, the observed hydrodynamic radius of the particles become larger. Second, during the adsorption of PFS-$COOH_{(15\ \%)}$, the process goes through a transient stage at the charge neutralization point for a very short period of time, essentially creating a local IEP, leading to limited aggregation of some particles, giving rise to an increase in the hydrodynamic radius of p-AL compared to the bare counterpart[34]. However, one cannot distinguish between these scenarios based on the available experimental data.

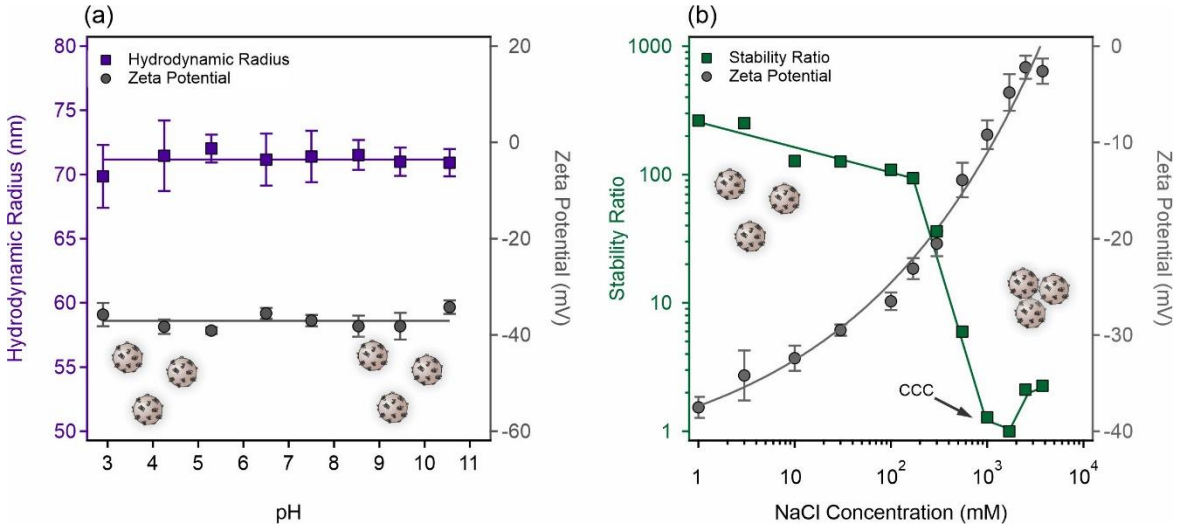

Figure 4.3. (a) The dependence of the hydrodynamic radius and zeta potential data of p-AL on the dispersion pH. The lines are linear fits to average the radius and potential values. (b) Zeta potential and stability ratio data of p-AL at different ionic strengths at pH 4.0. The lines are for eye-guidance purposes only. $c_{p\text{-}AL}$ = 25 mg L^{-1}; ionic strength: 1 mM.

In addition, the effect of ionic strength on the colloidal stability of p-AL was assessed in the range of 1 mM - 3 M NaCl at pH 4.0. Figure 4.3 b shows that the increased NaCl concentration resulted in a gradual screening of the surface charge, leading to a slow decrease in the magnitude of zeta potential, reaching zero around 3 M NaCl concentration. The trend in the stability ratios was in line with the surface charge features. Accordingly, at low salt levels (less than 100 mM), where the p-AL still maintained high zeta potential values, only slight changes were observed in the stability ratio values indicating the absence of significant aggregation.

The CCC is located at around 1 M NaCl, which is almost one order of magnitude higher than that determined for bare AL earlier (Figure 4.1 b). The presence of $PFS^{-}COOH_{(15\,\%)}$ on the AL NPs improves colloidal stability significantly, indicating the presence of non-DLVO forces providing further stabilization even at ionic strengths where electrostatic interactions are screened. Such high CCC was rarely reported in similar polymer-particle systems and confirms

our theory that steric repulsion between PFS layers contributes to the stabilization of p-AL particles[14–16]. These findings are also in line with our results on PFS-AuNP and aptamer-AuNP systems, where the anionic polyelectrolyte $PFS^{-}N_{3(20\ \%)}$ works either alone or in concert with the surface-grafted aptamer to provide steric stabilization to the AuNPs[4].

4.2.4. Interaction of ascorbic acid with poly(ferrocenylsilane)-amidine latex composites

As shown earlier, the redox properties of surface-bound PFS polymers change upon the addition of redox-active molecules such as ascorbic acid (AA) or $FeCl_3$[4]. These redox reactions are suspected to alter the zeta potential of p-AL NPs. We tested the impact of the presence of a range of AA concentrations on the stability and the surface charge of p-AL (Figure 4.4.).

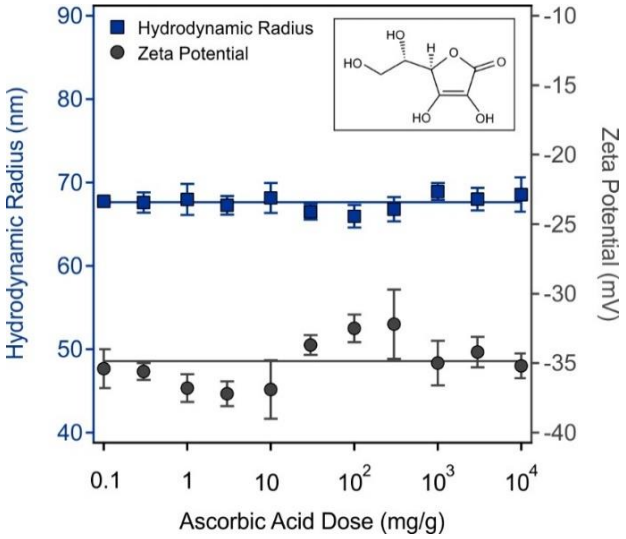

Figure 4.4. Hydrodynamic radius and zeta potential data of p-AL at different ascorbic acid doses (mg AA/g AL). The structure of AA is shown in the inset. The solid lines are linear fits to determine the mean values. cp-AL = 25 mg L^{-1}; pH = 4.0; ionic strength: 1.0 mM.

Contrary to our expectations, AA had no effect on either property since the obtained values correspond to those determined for p-AL under identical experimental conditions in Figure 4.3 a. For the hydrodynamic radius, an average value of (67.6±0.3) nm was calculated, which is barely smaller than the one determined for p-AL's (71.2±0.2) nm. Given the precision of ± 5 mV in the zeta potential measurements, the AA dose-dependent values can be considered the same within the experimental error yielding an average zeta potential of (-34.9±0.5) mV. Therefore, it is likely that no redox reaction occurred between $PFS^{-}COOH_{(15\ \%)}$ and AA. As AA possesses no charge at pH 4.0, its adsorption does not lead to a significant change in the zeta potential. Possible immobilization of AA likely took place via hydrogen bonding between hydroxyl groups of the AA and the azide functional group on the $PFS^{-}COOH_{(15\ \%)}$ or amidine groups located on the p-AL surface.

4.3. Conclusion

A thorough investigation of the colloidal properties of the p-AL nanozyme system is presented. At optimal pH and ionic strength, adsorption of negatively charged $PFS^{-}COOH_{(15\ \%)}$ onto the oppositely charged latex nanoparticles took place and resulted in charge neutralization followed by charge reversal, as the $PFS^{-}COOH_{(15\ \%)}$ dose was increased. Significant electrostatic repulsion was observed at high and low $PFS^{-}COOH_{(15\ \%)}$ concentration values, while van der Waals forces dominated around the charge neutralization point. The obtained p-AL composite, i.e., AL particles with $PFS^{-}COOH_{(15\ \%)}$ layer on the surface, exhibited excellent stability against salt-induced aggregation, as evidenced by the remarkable increase in the critical coagulation concentration. The addition of AA to the p-AL dispersions did not change the charge and size of the particles and thus, no evidence was found either for the redox reaction between $PFS^{-}COOH_{(15\ \%)}$ and AA or for AA adsorption on p-AL.

4.4. Materials and Methods

4.4.1. Materials

Amidine-functionalized polystyrene latex beads (mean diameter by transmission electron microscopy (TEM): 0.068 μm, coefficient of variation in diameter: 12.5%, solid concentration: 4% w/v in dispersion, density: 1.055 g mL^{-1} and surface charge density: 4.8 μC cm^{-2}) were purchased from Fischer Scientific (USA). Methanol (AnalaR NORMAPUR), NaOH (AnalaR NORMAPUR, ≥99.3%), HCl (AnalaR NORMAPUR, 37 w/w%), ascorbic acid (AA), and NaCl (99.9%) were purchased from VWR™ (Hungary). The 2,2-diphenyl-1-picrylhydrazyl (DPPH) radical (95%) was obtained from Alfa Aesar (USA). Hellmanex® III cleaning agent was purchased from Hellma (Germany). Polyvinyl difluoride (PVDF)-based 0.1 μm syringe filters (MILLEX-VV, Germany) were used to filter ultrapure water obtained from a VWR™ Puranity TU 3 UV/UF+ system.

During the synthesis of $(Et_4N)_2SO_3$ reagent, 0.215 mL Me_2SO_3 (2.53 mmol) and 2.1 mL Et_4NOH (35 w/w in water, 5.0 mmol) were mixed in 2 mL DMSO at room temperature for 4 hours. Slight precipitation of the product was observed during this time. The residual solvents were then evaporated from the DMSO, and the material was used as is in the synthesis of water-soluble anionic PFS^- polymers.

4.4.2. Preparation of carboxyl-functionalized poly(ferrocenylsilane)

The carboxyl-functionalized $PFS^-COOH_{(15\,\%)}$ was prepared in a multi-step procedure (1-5) as shown in Scheme 4.1, as detailed below.

Scheme 4.1. Schematic illustration of the preparation route of PFS^{-}COOH$_{(15\ \%)}$. Details of steps 2), through 5) are described in the text.

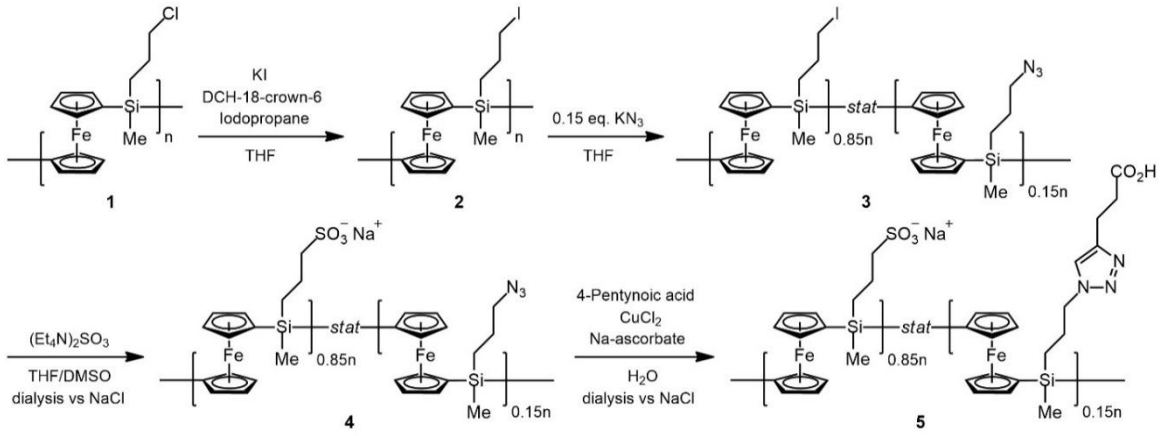

2) ***PFS-I***: A solution of PFS-Cl (compound 1 in Scheme 4.1, 241.8 mg; 0.793 mmol repeat units), KI (120.0 mg; 0.724 mmol), dicyclohexano-18-crown-6 (78.4 mg; 0.210 mmol), and iodopropane (2 mL; 19.6 mmol) in THF was stirred at 45 °C for a week. The polymer was precipitated in MeOH, dried, and stirred with the same reagents at 45 °C until the completion of the halogen exchange. The polymer was then precipitated and washed in MeOH and dried. Successful iodide substitution was confirmed by 1H NMR in benzene-d6 (see Figure 8.2).

3) ***PFS-I/N$_3$*** **(15 %)**: PFS-I (244.7 mg; 0.618 mmol repeat units) was dissolved in 10 mL THF, then KN_3 (2.5 mg; 0.031 mmol) dissolved in 5 mL DMSO was added. The reaction was left to proceed at 45 °C overnight. The resulting polymer was then precipitated and washed in MeOH followed by drying.

4) ***PFS^{-}/N$_3$*** **(15 %)**: PFS-I/N_3 (15 %; 96.2 mg; 0.251 mmol) was dissolved in 20 mL THF, then the 2 mL DMSO containing $(Et_4N)SO_3$ and an additional 2 mL DMSO solvent were added to set the solvent ratio of THF:DMSO to 5:1. The reaction was left to proceed at 35 °C over 3 days. At the endpoint, the product, now insoluble in THF, concentrated in the DMSO phase. Thereafter, the mixture was transferred to a dialysis hose (benzoylated cellulose, cut-off: 14

kDa) and dialyzed against ultrapure water, then 3 times against 0.1 M NaCl solution, then against water again. The resulting solution was directly used in the subsequent step.

5) **PFS^{-}COOH$_{(15\ \%)}$**: PFS^{-}/N_3 (15 %; 118.9 mg; 0.310 mmol repeating units) was dissolved in water, and 4-pentynoic acid (152.7 mg; 1.56 mmol), $CuCl_2$ (30 mg; 0.223 mmol) and sodium ascorbate (64.0 mg; 0.363 mmol) was added. The reaction was left to proceed at 35 °C. The resulting mixture was dialyzed against ultrapure water, then 3 times against 0.1 M NaCl solution, then against water again. The solvent was evaporated, and the polymer was finally dried under vacuum.

4.4.3. Light scattering

Zeta potential and hydrodynamic radius (R_h) values were determined in light scattering measurements to assess the colloidal stability of the particle dispersions at (25.0±0.2) °C. The zeta potential was measured by electrophoretic light scattering using a Litesizer^{TM} 500 (Anton Paar, Austria) device (40 mW semiconductor laser diode operating at 658 nm wavelength and 200 V voltage was applied). First, the electrophoretic mobility values were recorded and converted to zeta potentials using the Smoluchowski equation[35]. The 2.0 mL samples were left to equilibrate for 2 hours at room temperature prior to the measurements, which were executed in omega-shaped plastic cuvettes (Anton Paar). The zeta potential values were reported as an average of 5-8 runs with approximately ±5 mV accuracy.

The pH-dependent surface charging of AL and p-AL was probed by measuring the zeta potentials at constant ionic strength (1 mM) throughout the pH range of 3-11. In these experiments, 25 mg L^{-1} acidic (pH 3) and alkaline (pH 11) dispersions of the relevant materials were prepared. Then, by mixing various volumes of the two stocks, a series of secondary dispersions, the pH of which gradually changed from 4 to 11, was obtained. This procedure helped to maintain constant ionic strength and material concentration, while altering the pH in

the range of interest. Besides, the same particle concentration was used in all other light scattering measurements, in which pH 4.0 was set in the samples.

The hydrodynamic radius values of the particles were determined with dynamic light scattering (DLS) using an ALV-NIBS/HPPS (Germany) particle sizer equipped with a 2.5 mW HeNe (632.8 nm wavelength) laser source. The intensity of the light was collected at a scattering angle of 173°. The cumulant fit was applied to analyze the autocorrelation function and to obtain the decay rate constants, which were converted to translational diffusion coefficient values to calculate the hydrodynamic radii with the Stokes-Einstein equation[36,37].

In time-resolved DLS, the determination of apparent aggregation rate constants (k_{app}) was possible using the following equation[23]:

$$k_{app} = \frac{1}{R_h(0)} . (\frac{dR_h(t)}{dt})_{t \to 0} \quad \text{(Equation 4.1)}$$

where $R_h(0)$ is the hydrodynamic radius of non-aggregated monomer particles, $\frac{dR_h(t)}{dt}$ is the rate of change of the hydrodynamic radii, i.e., the slope of the radii-time plots. This protocol enables to investigate early stages of particle aggregation, while it is not suitable to follow cluster formation of aggregated particles. The stability ratio (W) provides a measure of colloidal stability and can be obtained as[38]

$$W = \frac{k_{app(fast)}}{k_{app}} \quad \text{(Equation 4.2)}$$

where $k_{app(fast)}$ is the apparent aggregation rate constant in rapidly aggregating samples, e.g., at 1.0 M ionic strength, at which attractive interactions are dominant and electrostatic forces are screened. Note that the stability ratio is directly proportional to the stability of a colloidal dispersion. Measurements in highly stable dispersions yield high or not even measurable stability ratio values, whereas they are close to unity in unstable samples. The time-resolved DLS measurements were initiated immediately upon the addition of the desired

volume of the aggregating agents, NaCl or $PFS^{-}COOH_{(15\,\%)}$. The stability ratio data are subject to about 10% measurement error.

4.5. Bibliography

1. Alsharif, N. B. *et al.* Dual functionality of ferrocene-based metallopolymers as radical scavengers and nanoparticle stabilizing agents. *Nanoscale* (2023).
2. Halmagyi, T., Hao, J., Hempenius, M. A. & Vancso, G. J. Poly(ferrocenylsilane) Hydrogels as a Foundry for Metal Nanoparticle Synthesis by Direct Reduction of Electrolytes via a Catalytic Route. *ACS Appl Nano Mater* **5**, 8868–8874 (2022).
3. You, J., Manners, I. & Dou, H. In Situ Preparation of Composite Redox-Active Micelles Bearing Pd Nanoparticles for the Reduction of 4-Nitrophenol. *Langmuir* **37**, 9089–9097 (2021).
4. Song, J. *et al.* Poly(ferrocenylsilane) electrolytes as a gold nanoparticle foundry: 'two-in-one' redox synthesis and electrosteric stabilization, and sensing applications. *Nanoscale* **9**, 19255–19262 (2017).
5. Cui, K., Song, Y. & Wang, L. Electrochemical and electrocatalytic behaviors of poly(ferrocenylsilane)/DNA modified glass carbon electrode. *Electrochem commun* **10**, 1712–1715 (2008).
6. Sui, X., Feng, X., Song, J., Hempenius, M. A. & Vancso, G. J. Electrochemical sensing by surface-immobilized poly(ferrocenylsilane) grafts. *J Mater Chem* **22**, 11261–11267 (2012).
7. Trefalt, G., Szilagyi, I. & Borkovec, M. Poisson–Boltzmann description of interaction forces and aggregation rates involving charged colloidal particles in asymmetric electrolytes. *J Colloid Interface Sci* **406**, 111–120 (2013).
8. Montes Ruiz-Cabello, F. J., Oncsik, T., Rodríguez-Valverde, M. A., Maroni, P. & Cabrerizo-Vilchez, M. Specific Ion Effects and pH Dependence on the Interaction Forces between Polystyrene Particles. *Langmuir* **32**, 11918–11927 (2016).
9. Diao, Y. *et al.* Reconciling DLVO and non-DLVO Forces and Their Implications for Ion Rejection by a Polyamide Membrane. *Langmuir* **33**, 8982–8992 (2017).
10. Leong, Y. K. Interparticle forces arising from an adsorbed strong polyelectrolyte in colloidal dispersions: Charged patch attraction. *Colloid Polym Sci* **277**, 299–305 (1999).
11. Popa, I., Papastavrou, G. & Borkovec, M. Charge regulation effects on electrostatic patch-charge attraction induced by adsorbed dendrimers. *Physical Chemistry Chemical Physics* **12**, 4863–4871 (2010).
12. Motta, R. J. B. *et al.* Polyphosphates can stabilize but also aggregate colloids. *Physical Chemistry Chemical Physics* **22**, 15–19 (2019).
13. Wang, D., Tejerina, B., Lagzi, I., Kowalczyk, B. & Grzybowski, B. A. Bridging interactions and selective nanoparticle aggregation mediated by monovalent cations. *ACS Nano* **5**, 530–536 (2011).
14. Huang, H. & Ruckenstein, E. Effect of steric, double-layer, and depletion interactions on the stability of colloids in systems containing a polymer and an electrolyte. *Langmuir* **22**, 4541–4546 (2006).
15. Fritz, G., Schädler, V., Willenbacher, N. & Wagner, N. J. Electrosteric Stabilization of Colloidal Dispersions. *Langmuir* **18**, 6381–6390 (2002).

16. Einarson, M. B. & Berg, J. C. Electrosteric Stabilization of Colloidal Latex Dispersions. *J Colloid Interface Sci* **155**, 165–172 (1993).
17. Halmagyi, T., Hao, J., Hempenius, M. A. & Vancso, G. J. Poly(ferrocenylsilane) Hydrogels as a Foundry for Metal Nanoparticle Synthesis by Direct Reduction of Electrolytes via a Catalytic Route. *ACS Appl Nano Mater* (2022).
18. Smith, A. M., Maroni, P. & Borkovec, M. Attractive non-DLVO forces induced by adsorption of monovalent organic ions. *Physical Chemistry Chemical Physics* **20**, 158–164 (2018).
19. Cao, T., Borkovec, M. & Trefalt, G. Heteroaggregation and Homoaggregation of Latex Particles in the Presence of Alkyl Sulfate Surfactants. *Colloids and Interfaces* **4**, 52 (2020).
20. Sugimoto, T., Nishiya, M. & Kobayashi, M. Electrophoretic mobility of carboxyl latex particles: effects of hydrophobic monovalent counter-ions. *Colloid Polym Sci* **295**, 2405–2411 (2017).
21. Hakim, A., Nishiya, M. & Kobayashi, M. Charge reversal of sulfate latex induced by hydrophobic counterion: effects of surface charge density. *Colloid Polym Sci* **294**, 1671–1678 (2016).
22. Alsharif, N. B. *et al.* Design of hybrid biocatalysts by controlled heteroaggregation of manganese oxide and sulfate latex particles to combat reactive oxygen species. *J Mater Chem B* **9**, 4929–4940 (2021).
23. Holthoff, H., Egelhaaf, S. U., Borkovec, M., Schurtenberger, P. & Sticher, H. Coagulation Rate Measurements of Colloidal Particles by Simultaneous Static and Dynamic Light Scattering. *Langmuir* **12**, 5541–5549 (1996).
24. Xu, S. & Sun, Z. Progress in coagulation rate measurements of colloidal dispersions. *Soft Matter* **7**, 11298 (2011).
25. Trompette, J.-L. & Lahitte, J.-F. Influence of the Counterion Nature on the Stability Sequence of Hydrophobic Latex Particles. *J Phys Chem B* **123**, 3859–3865 (2019).
26. Ehrl, L. *et al.* Role of Counterion Association in Colloidal Stability. *Langmuir* **25**, 2696–2702 (2009).
27. Oncsik, T., Trefalt, G., Borkovec, M. & Szilagyi, I. Specific Ion Effects on Particle Aggregation Induced by Monovalent Salts within the Hofmeister Series. *Langmuir* **31**, 3799–3807 (2015).
28. Omija, K., Hakim, A., Masuda, K., Yamaguchi, A. & Kobayashi, M. Effect of counter ion valence and pH on the aggregation and charging of oxidized carbon nanohorn (CNHox) in aqueous solution. *Colloids Surf A Physicochem Eng Asp* **619**, 126552 (2021).
29. Iselau, F. *et al.* Formation and relaxation kinetics of starch–particle complexes. *Soft Matter* **12**, 9509–9519 (2016).
30. Vasti, C., Borgiallo, A., Giacomelli, C. E. & Rojas, R. Layered double hydroxide nanoparticles customization by polyelectrolyte adsorption: mechanism and effect on particle aggregation. *Colloids Surf A Physicochem Eng Asp* **533**, 316–322 (2017).
31. Vásárhelyi, L. *et al.* Stability of Boron Nitride Nanosphere Dispersions in the Presence of Polyelectrolytes. *Langmuir* **37**, 5399–5407 (2021).
32. Hajdú, A. *et al.* Enhanced stability of polyacrylate-coated magnetite nanoparticles in biorelevant media. *Colloids Surf B Biointerfaces* **94**, 242–249 (2012).
33. Feng, L. & Adachi, Y. Brownian flocculation of negatively charged latex particles with low charge density polycation at various ionic strengths. *Colloids Surf A Physicochem Eng Asp* **454**, 128–134 (2014).
34. Hierrezuelo, J., Szilagyi, I., Vaccaro, A. & Borkovec, M. Probing Nanometer-Thick Polyelectrolyte Layers Adsorbed on Oppositely Charged Particles by Dynamic Light Scattering. *Macromolecules* **43**, 9108–9116 (2010).
35. Delgado, A. V., González-Caballero, F., Hunter, R. J., Koopal, L. K. & Lyklema, J. Measurement and Interpretation of Electrokinetic Phenomena (IUPAC Technical Report). *Pure and Applied Chemistry* **77**, 1753–1805 (2005).

36. Hassan, P. A., Rana, S. & Verma, G. Making sense of Brownian motion: Colloid characterization by dynamic light scattering. *Langmuir* **31**, 3–12 (2015).
37. Glaubitz, C., Rothen-Rutishauser, B., Lattuada, M., Balog, S. & Petri-Fink, A. Designing the ultrasonic treatment of nanoparticle-dispersions *via* machine learning. *Nanoscale* **14**, 12940–12950 (2022).
38. Takeshita, C., Masuda, K. & Kobayashi, M. The effect of monovalent anion species on the aggregation and charging of allophane clay nanoparticles. *Colloids Surf A Physicochem Eng Asp* **577**, 103–109 (2019).

5. Preparation of gold nanoparticle-poly(ferrocenylsilane)-gold composite electrodes for antioxidant detection

This chapter contains the results of electrochemistry experiments. The original goal of this project was to develop an electrografted PFS-based electrochemical aptasensor. The electrografting of PFS-propyl-methylimidazolium chloride (PFS-MID^+) was performed according to a procedure published previously[1]. Subsequently, gold nanoparticles were electrochemically deposited onto the electrodes, and the redox sensitivity of the system was assessed using ascorbic acid as model target via an electrochemical oxidation method. The outcomes of this research show promise for future experiments with PFS-based electrochemical sensors for redox-active species.

5.1. Introduction

Electrodes modified with polymer layers have been a target of intense research in several fields of research. Redox active polymers have widely been used for a variety of applications such as sensing[1–6] and electrocatalysis[7–9], including environmental applications such as electrochemical CO_2 reduction (CO2R)[10,11]. Vancso et al. have previously reported the post-polymerization modification and subsequent electrografting of a poly(ferrocenylsilane) poly(ionic liquid) (PIL) onto gold electrodes via electrochemical reduction of the Au surface[1].

Metal and especially noble metal electrodes are ubiquitous in electrocatalysis and in electrochemical sensing. Both CO2R[12,13] and oxygen reduction reaction (ORR)[14,15] can be achieved using gold nanoparticle decorated electrodes. MNPs have also been used for the electrochemical sensing of a variety of targets including DNA[16], dopamine[17,18], organic pollutants[19], H_2O_2[20] and more[21–23]. John et al. have summarized the state of the art for conductive polymer-metal nanoparticle composite electrochemical sensors in 2021[24] and have found that a staggering variety of targets can be detected with such systems at sensitivities competitive with other methods.

The present work aims to add to this field and expand our understanding of the materials chemistry of poly(ferrocenylsilane)-gold nanoparticle composite electrodes and to describe the possible application of such systems. As a standard representative analyte, ascorbic acid was chosen for demonstration purposes..

5.2. Synthesis and characterization

5.2.1. Electrochemical grafting methylimidazolium-poly(ferrocenylsilane) layers on Au and Au/Si substrates

Methlyimidazolium-poly(ferrocenylsilane) (PFS-MID$^+$) layers were electrochemically grafted onto gold foils and to gold-coated silica wafers via a method adapted from literature[1]. In brief, 5 mg mL^{-1} PFS-MID$^+$ was dissolved in ionic liquid 1-ethyl-3-methylimidazolium ethyl sulfate, and the substrate (either gold or gold / silicon) was immersed in the resulting poly(ionic liquid) (PIL) solution. We first performed cyclic voltammetry (CV) to determine the potential of deposition, as seen on Figure 5.1 a. The experiments were performed in a three-electrode cell, with Pt wires as both counter-and pseudo-reference electrodes (CE and RE, respectively), and the substrate as working electrode (WE).

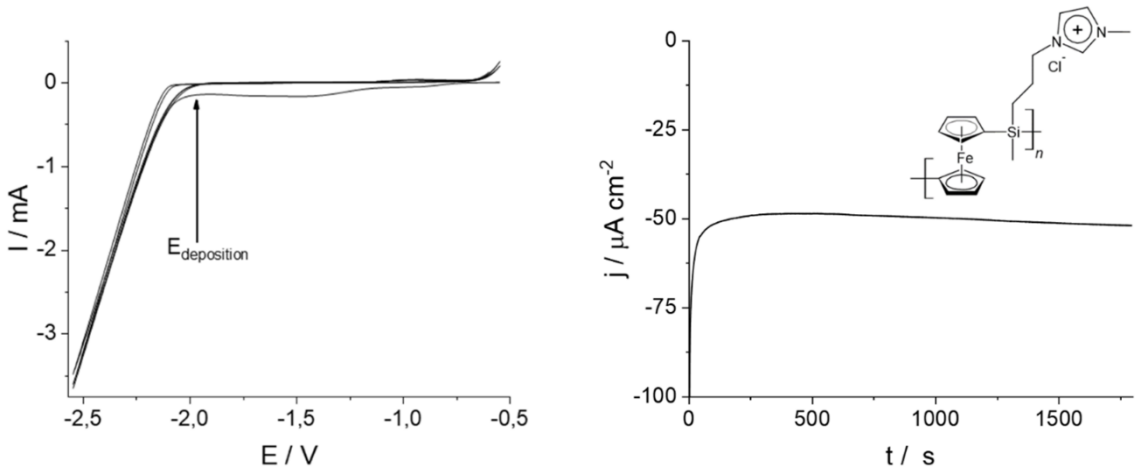

Figure 5.1. Cyclic voltammogram of Au substrate in PFS-MID$^+$ PIL solution (a). Electrografting of PFS-MID$^+$ on Au substrate at E = -2.2 V (b). Inset in (b) shows the formula of PFS-MID$^+$. In all cases, WE: Au, CE: Pt, RE: Pt, and $c_{PFS\text{-}MID+}$ = 5 mg mL^{-1}.

Note that the experiment shown in Figure 5.1 a was repeated for every deposition to precisely determine the deposition potential, which remained in all cases at (-2.2 ± 0.2) V vs Pt. Results of typical chronoamperometric grafting experiments on an Au/Si substrate are shown in Figure 5.1 b. The deposition current remained at a stable -50 µA value throughout the entire duration of the 30 minutes period, with only a minor increase. This indicates uniform layer formation

during the experiment, with a constant rate of deposition. According to literature[25], the mechanism by which this deposition occurs is via reduction of the gold surface. As Equation 5.1 shows, the formation of gold anions results in PFS-gold complexes, essentially creating a new phase of this mixed material on the surface.

$$Au + ne^- \rightarrow [PFS - MID^+Au^-] + nX^- \text{ (Equation 5.1[25])}$$

5.2.2. Profilometric characterization of grafted methylimidazolium-poly(ferrocenylsilane) layers on Au/Si substrate

While the gold foil surfaces are undefined, the Au/Si wafer is flat enough so that 2 dimensional profilometry could be used to characterize the PFS-MID$^+$ layers grown on these substrates. A 0.25 µm x 0.25 µm square sized sample was examined before and after electrografting, and results of these experiments are shown on Figure 5.2.

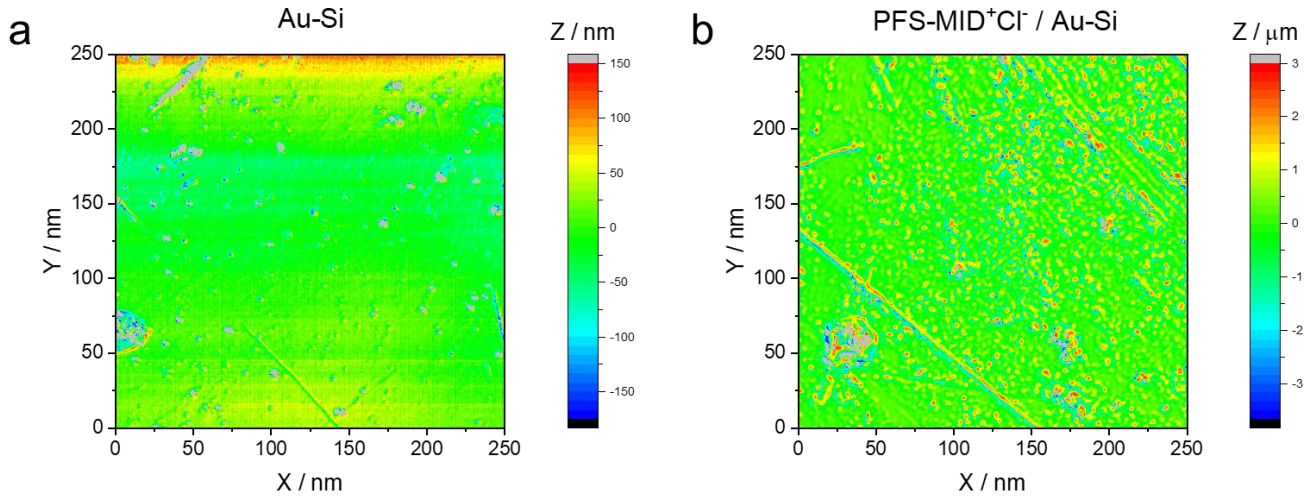

Figure 5.2. Profilometric characterization results of bare Au/Si wafer (a) and PFS-MID$^+$ electrografted Au/Si wafer (b).

The bare Au-Si wafer is flat and homogeneous, with maximum 150 nm roughness in places (Figure 5.2 a). In contrast, after electrografting the roughness is increased by an order of

magnitude (from 150 nm to 5 μm maximum deviation), indicating the spontaneous formation of polymer particulates on the substrate. Interestingly, the layers also seem to be anisotropic, with lines of polymer forming on the surface. This is possibly due to the influence of stirring and solvent viscosity on surface morphology, or alternatively irregularities on the subtrate surface act as orienting features. The polymer layer can be assumed to cover the entire surface, although formation of the aforementioned particulates results in uneven layer thickness.

5.2.3. Electrodeposition of gold nanoparticles

Gold nanoparticle deposition on PFS-MID$^+$ electrografted Au-foil and Au/Si substrates was performed according to a literature method modified to fit our system[26]. AuNPs deposition proceeded via chronoamperometry (CA) in a 0.1 M NaCl and 1 mM $KAuCl_4$ electrolyte in a three-electrode cell with a Pt CE and a Ag/AgCl RE at -400 mV for 1800 seconds. As Figure 5.3 shows, the gold deposition was successful. Over the electrodeposition, the gold substrate progressively turned brown, with stirring and even cell geometry influencing the homogeneousness of the AuNP layers. The as-prepared electrodes are denoted as AuNP / PFS / Au and AuNP / PFS / Au/Si, depending on the electrode substrate.

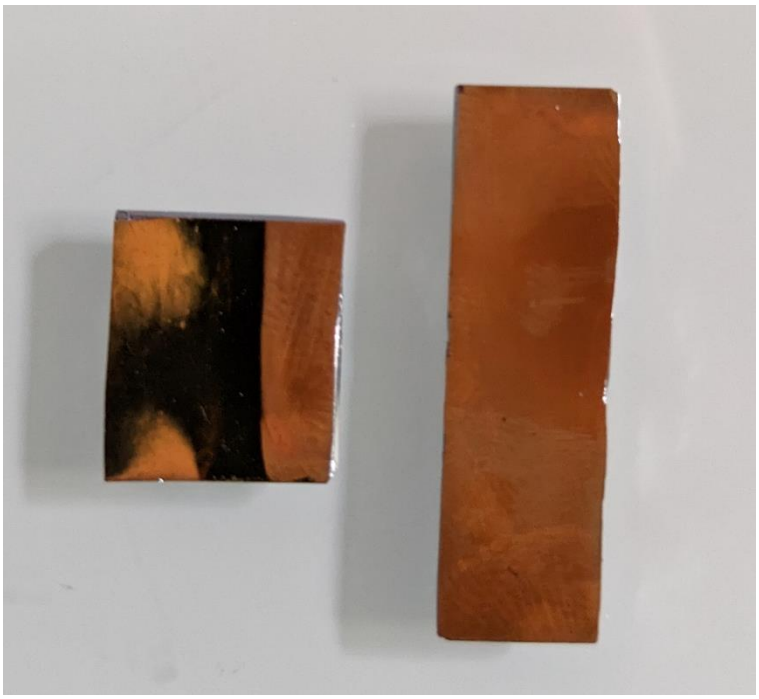

Figure 5.3. AuNP / PFS / Au/Si samples after gold nanoparticle deposition over 1800 s.

5.2.4. Electrochemical characterization

All samples were characterized with cyclic voltammetry in 0.1 M NaCl electrolyte in a three-electrode cell with a Pt CE and an Ag/AgCl RE. Results are shown on Figure 5.4.

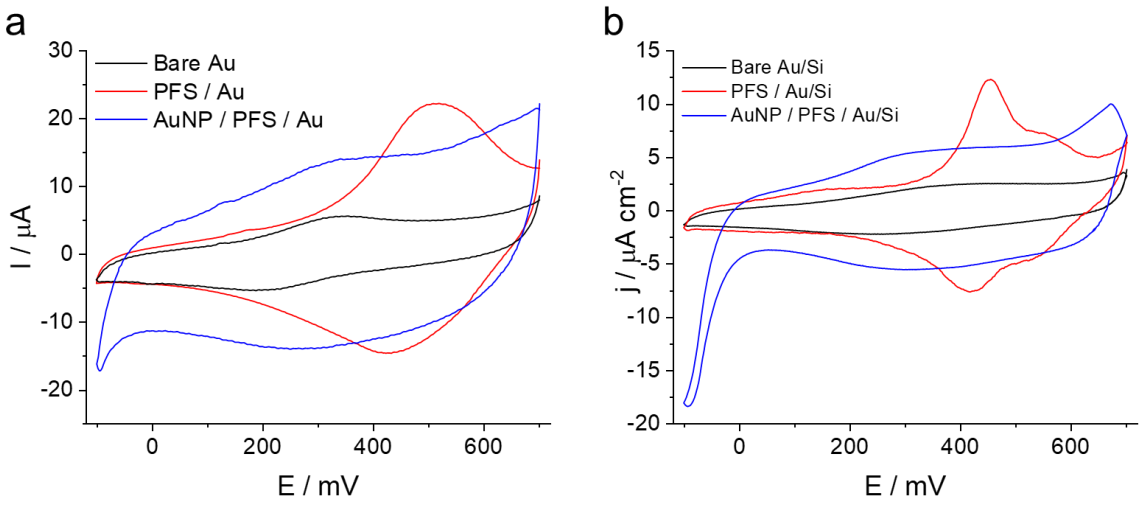

Figure 5.4. Cyclic voltammograms of samples deposited on gold foil (a) and on Au/Si wafer (b). Sample was used as WE, Pt wire as CE and Ag/AgCl as RE. Electrolyte was 0.1 M NaCl in all cases. Sweep rate: 50 mV s^{-1}.

Electrochemical activity in the -100 - +700 mV range increased which is consistent with previous electrochemical experiments on similar PFS layers. The dual redox peak characteristic of PFS only appears on the layer deposited on the gold-silicon wafer (Figure 5.4 b), but a single pair of peaks is also present at 400-500 mV in the case of the gold foil electrodes (Figure 5.4 a). Regardless of the number of peaks, the PFS-MID^+ layer dominates electroactivity in both cases, indicating full coverage of the substrate.

The gold nanoparticle-deposited AuNP / PFS / Au sample also exhibits increased electroactivity compared to the bare gold foil as seen on the cyclic voltammogram (Figure 5.4 a, blue curve) with currents between -20 and +20 µA vs the -5-+5 µA values of the bare gold. However, the AuNP / PFS / Au curve lacks the characteristic peak of the PFS. Instead, these samples exhibit cyclic voltammograms of similar shape to those of the bare gold foil electrodes, and the greater electroactivity can be attributed to the greater active surface provided by the

nanoparticles. This indicates that the AuNPs cover the electrode well enough to significantly influence its electroactivity.

Similar conclusions can be drawn regarding the AuNP / PFS / Au/Si sample insofar as its electroactivity is improved compared to the bare Au/Si electrode (-5 to +5 μA cm^{-2} vs -2 to +2 μA cm^{-2}). However, this electrode, in addition to the disappearance of the PFS redox peaks at 400-500 mV, also exhibits lower stability at more negative potential values, with an onset potential of either oxygen reduction or electrode surface degradation present at 0 V.

5.3. Ascorbic acid sensing

5.3.1. Ascorbic acid sensing experiments with poly(ferrocenylsilane-gold and gold nanoparticle-poly(ferrocenylsilane)-gold electrodes

We examined the ascorbic acid oxidation activity of samples deposited on gold foil substrates with cyclic voltammetry. The goal was to determine whether the PFS redox activity could be used for ascorbic acid (vitamin C) detection and if so, what potential should be used. The results are shown on Figure 5.5.

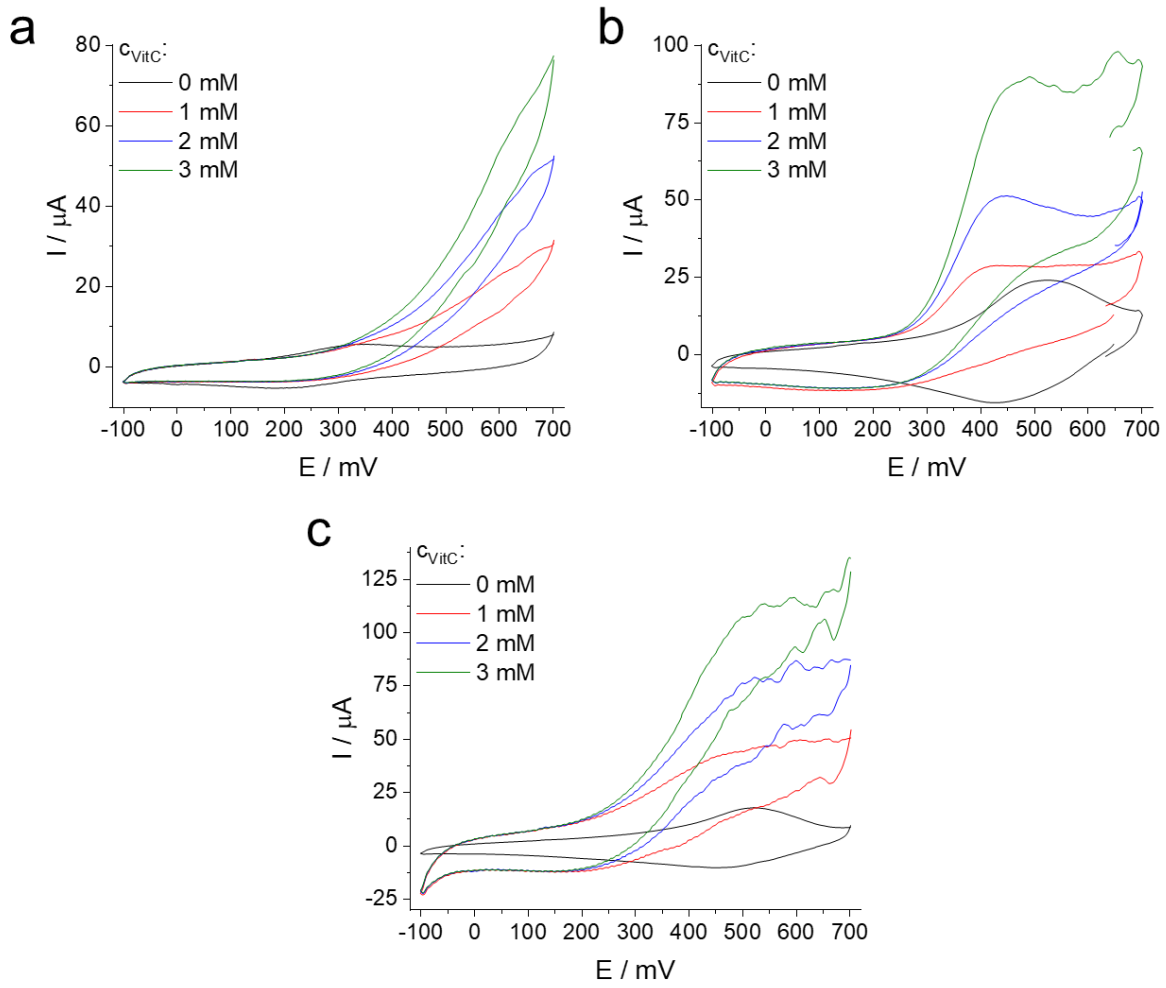

Figure 5.5. Cyclic voltammograms of ascorbic acid concentration-dependent response of bare gold foil samples (a), PFS-MID$^+$ grafted gold foil (b) and AuNP-deposited AuNP / PFS / Au samples (c). Sample was used as WE, Pt wire as CE and Ag/AgCl as RE. Electrolyte was 0.1 M NaCl in all cases. Sweep rate: 50 mV s^{-1}.

The bare gold foil sample (Figure 5.5 a) exhibits increased electroactivity in the 400-700 mV potential range upon ascorbic acid addition, but no new redox peaks appear. For the PFS / Au samples (Figure 5.5 b), the characteristic redox peak of the polymer shifts from 500 to 400-450 mV upon introduction of vitamin C to the system. At the same time, the reduction peak at -420 mV disappears completely, as the reversible oxidation of the polymer is overshadowed by the

irreversible ascorbic acid oxidation. This effect is even more pronounced in the case of the AuNP / PFS / Au samples (Figure 5.5 c), although significant noise was also present in these samples.

We also performed chronoamperometric titration measurements at -450 mV on these samples to determine the low ascorbic acid concentration response of the modified electrodes. In each step, 2 µM ascorbic acid was added to the electrolyte, and current response was monitored. The results of these experiments are shown on Figure 5.6.

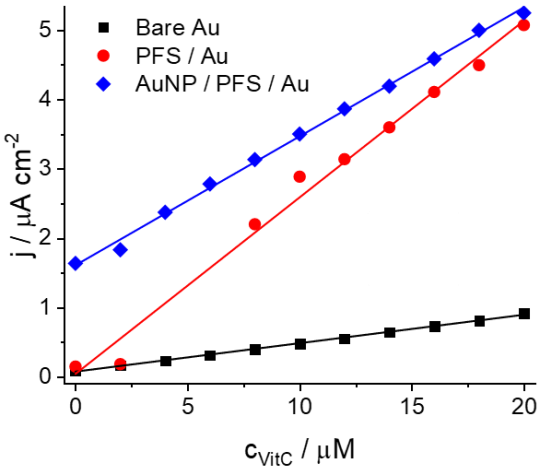

Figure 5.6. Chronoamperometric titration results on samples with gold foil substrate.

The bare gold substrate has a linear response in the entire concentration range, but its electroactivity is low (current density response: 0.041 µA cm^{-2} $µM^{-1}$), in agreement with the data in Figure 5.5 a. This finding is also in line with results from previous literature[25]. The PFS-grafted electrodes exhibited very noisy signals at low ascorbic acid concentration, which made detection impossible, hence the missing points below 8 µM concentration. Beyond this point however, this sample exhibited higher response than the bare gold, as well as the steepest current density (j) vs ascorbic acid concentration (c_{VitC}) slope of the three samples at a current density response of 0.255 µA cm^{-2} $µM^{-1}$, about 6.2 times greater than that of the bare gold foil.

The highest electroactivity, in accordance with our findings in Figure 5.5, was that of the AuNP / PFS / Au samples. The response of this sample remained the highest over the entire concentration range, although this is mainly due to the comparatively high current density without ascorbic acid. This high „zero current" also provided a better signal-to-noise ratio, making it significantly easier to detect signals at lower ascorbic acid concentrations. The current density response of the AuNP / PFS / Au samples was 0.186 $\mu A\ cm^{-2}\ \mu M^{-1}$, significantly lower than that of the PFS / Au, but still 4.5 times greater than the value for the bare gold foil. Regardless, at higher concentrations the PFS / Au sample's electroactivity approaches that of the AuNP / PFS / Au. These findings indicate that gold nanoparticle deposition is a promising method to increase the electroactivity and sensitivity of this system.

5.3.2. Ascorbic acid sensing experiments with poly(ferrocenylsilane) / Au/Si electrodes

Similar experiments were performed on samples deposited onto Au/Si substrates. The results of the cyclic voltammetry tests of ascorbic acid response are shown on Figure 5.7.

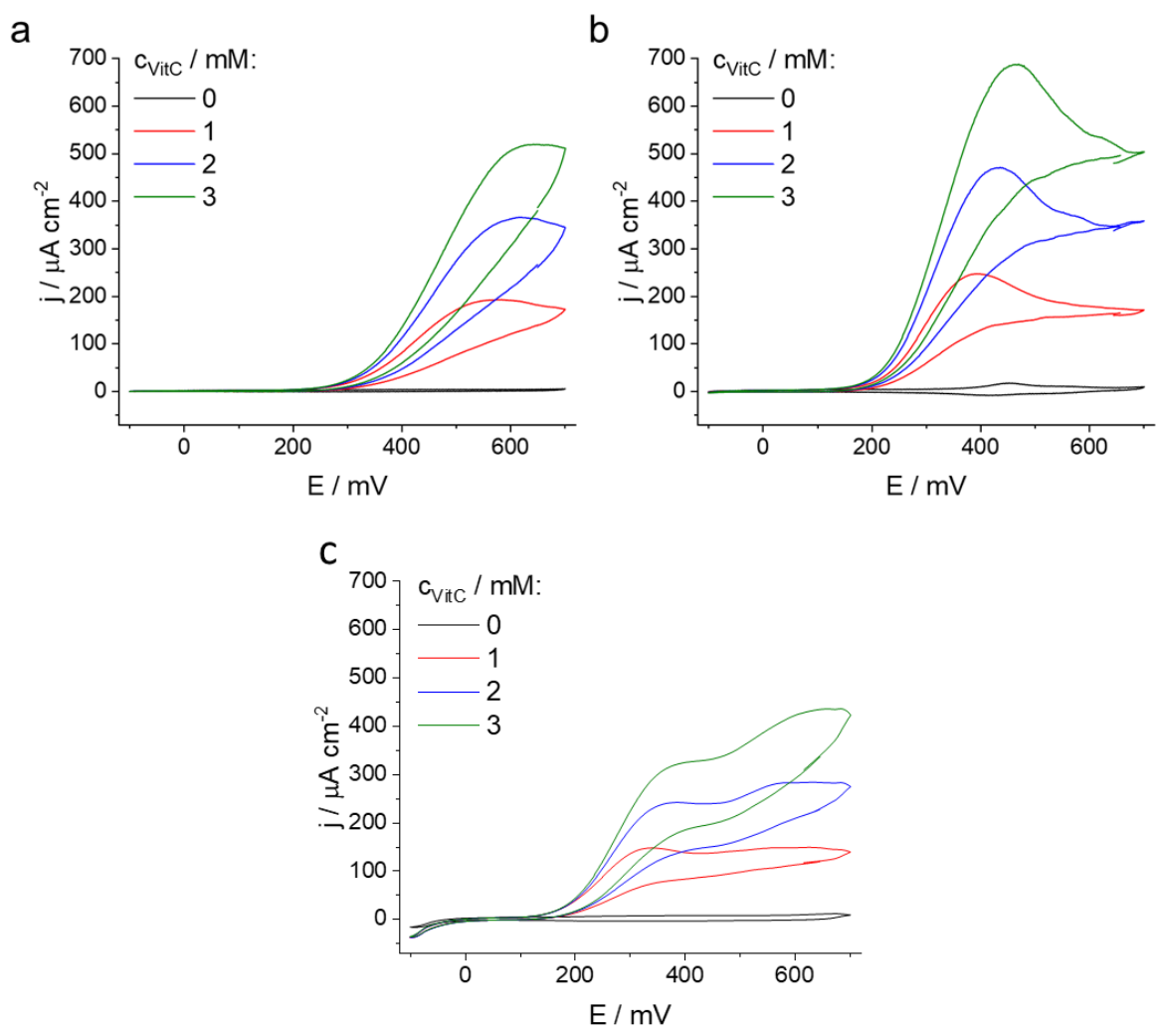

Figure 5.7. Cyclic voltammograms of ascorbic acid concentration-dependent response of bare Au/Si samples (a), PFS-MID^{+} grafted Au/Si (b) and AuNP / PFS / Au/Si (c). Sample was used as WE, Pt wire as CE and Ag/AgCl as RE. Electrolyte was 0.1 M NaCl in all cases. Sweep rate: 50 mV s^{-1}.

As Figure 5.7 shows, addition of ascorbic acid significantly increases electrochemical response of all samples in the 250 – 700 mV potential range. The shape of the CVs is characteristic of the irreversible oxidation of ascorbic acid, with a single oxidation peak at around 580 mV and an onset potential of 250 mV. The onset potential of ascorbic acid oxidation

in the case of PFS / Au/Si samples (Figure 5.7 b) is lower, at around 150 mV, than that of the blank electrodes (Figure 5.7 a, 220 mV) indicating the increased electroactivity brought on by the grafting of the redox-active polymer. Similarly, the overpotential required for the oxidation is also decreased, indicated by the shift of the oxidation peak to 420-450 mV. Peak current densities are also higher than those of the bare Au/Si samples (700 μA cm^{-2} at 3 mM ascorbic acid concentration, compared to 500 μA cm^{-2} in the case of the bare Au/Si), indicating better sensitivity.

In contrast, the case of AuNP / PFS / Au/Si samples (Figure 5.7 c) is curious. The onset potential of ascorbic acid oxidation is decreased even more, to about 110-120 mV, but the peak currents of oxidation do not even reach 500 μA cm^{-2} at 3 mM ascorbic acid concentration, falling behind the performance of both the bare and the PFS-grafted electrodes. In addition, the shape of these voltammograms is also different from those of the previous samples, with the appearance of a new irreversible redox peak at around 300 mV.

Chronoamperometric titration could not be performed on the AuNP / PFS / Au/Si samples. Despite multiple tries with different samples of various AuNP layer thicknesses, the chronoamperometric signal was consistently too noisy to evaluate. The chronoamperometric titration results with the other samples (Bare Au/Si and PFS / Au/Si) are shown in Figure 5.8. Oddly, these results do not corroborate the previous finding of improved sensitivity upon PFS grafting on Au/Si substrates, possibly due to the low signal-to-noise ratio of the potentiostat in this current range.

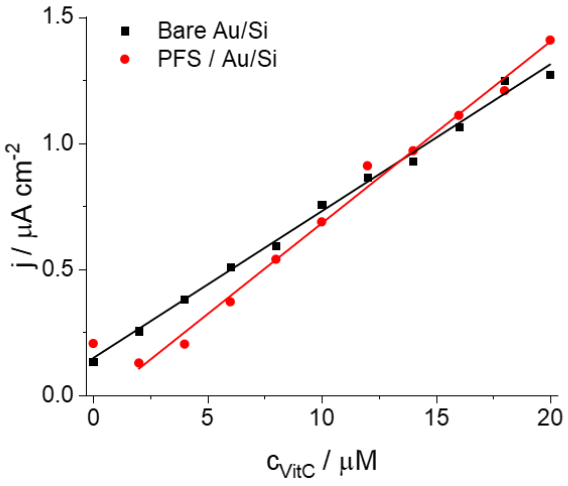

Figure 5.8. Chronoamperometric titration results on samples with Au/Si wafer substrate.

As seen, the bare Au/Si wafer has similar sensitivity to the PFS-grafted samples, even outperforms those at low ascorbic acid concentrations, despite similar initial current densities. Although the current density response of the PFS / Au/Si sample (0.072 µA cm^{-2} $µM^{-1}$) is better than that of the bare Au/Si sample (0.058 µA cm^{-2} $µM^{-1}$), the polymer-coated electrode only outperforms the bare one at ascorbic acid concentrations over 14 µM.

In contrast, both the PFS / Au and the AuNP / PFS / Au samples consistently outperform the blank gold foil even at 2 µM concentration (Figure 5.6). In addition, current density responses of both the AuNP / PFS / Au and the PFS / Au sample are significantly greater, although lower than those found in literature for similar systems[1].

5.4. Conclusion

In this chapter, we have adapted results from previous literature for electrografting of cationic polyelectrolyte poly(ferrocenylsilane)-methylimidazolium chloride (PFS-MID^{+}) onto gold and gold-silicone substrates. We characterized the surface topography of samples on Al-Si substrates with 2D profilometry, and employed various electrochemical techniques for testing

electroactivity of the deposited layers. We also electrodeposited gold nanoparticles on samples with gold foil substrate. We tested ascorbic acid sensitivity of the various samples, and have found that, in line with previous literature[25], poly(ferrocenylsilane) coated electrodes are more sensitive than bare gold. Additionally, gold nanoparticle deposition on the PFS-coated gold foil electrodes yields increased current densities in the investigated ascorbic acid concentration range. When compared with the colloidal sensing method presented before[27], this electrochemical method – and similar methods presented previously in the literature[1] – have superior sensitivity towards ascorbic acid, with a 2 μM limit of detection versus the 10 μM exhibited by the colloidal method[27].

If this project is to continue in the future, the gold foil samples show greater promise as electrosensor than the Au/Si electrodes owing to the better sensitivity and electroactivity increases upon PFS grafting and AuNP deposition. Further research requires the gold nanoparticle deposition to be optimized.

5.5. Materials and Methods

5.5.1. Materials

Dicyclohexano-18-crown-6 (98 %), 1-iodopropane (99 %), dimethyl sulfoxide (DMSO, 99.9 %), sodium chloride (NaCl, 99.5 %), 1-methylimidazole, 1-ethyl-3-methylimidazolium ethyl sulfate (95 %) and dialysis hoses (benzoylated cellulose, cut-off: 14 kDa) were purchased from Sigma-Aldrich (Saint-Quentin-Fallavier, France). Tetrahydrofuran (THF, anhydrous) and methanol (MeOH, technical), were procured from VWR (Rosny-sous-Bois, France).

All electrochemical experiments were performed on an Autolab PGSTAT204 potentiostat-galvanostat from Metrohm (Villebon-sur-Yvette, France).

5.5.2. Poly(ferrocenylsilane) synthesis

The methylimidazolium-functionalized cationic polyelectrolyte PFS-MID$^+$Cl$^-$ was synthesized in accordance with previously published literature[25]. Scheme 5.1 shows the conversion of PFS-I to PFS-MID$^+$Cl$^-$.

Scheme 5.1. Reaction scheme showing conversion of PFS-I to PFS-MID$^+$Cl$^-$. Steps 1) through 4) are described below.

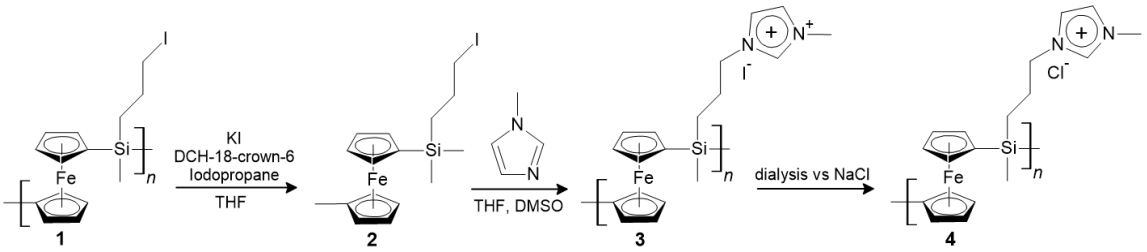

1) ***PFS-Cl***: Poly(ferrocenyl(3-chloropropyl)methylsilane) was synthesized via a previously published procedure[28] in a transition-metal-catalyzed ring-opening polymerization reaction from a precursor ferrocenylsilane containing methyl and chloropropyl-bearing [1] silaferrocenophane monomer side-chains. ^{1}H NMR was performed on the polymer product in benzene-d6 (Figure 8.1). δ: 0.55 ($SiCH_3$) 1.10 (1-CH_2) 1.80 (2-CH_2) 3.25 (3-CH_2) 4.05-4.55 (Fc). The peak at 0.40 ppm represents solvent residues.

2) ***PFS-I***: A mixture in THF containing PFS-Cl, potassium iodide (KI, 1 equivalent (eq) respective to PFS repeat units), dicyclohexano-18-crown-6 (0.25 eq), and iodopropane (0.025 eq) was stirred at 45 °C for at least a week. The polymer was then precipitated in MeOH or EtOH, dried, and subsequently the reaction was continued with the same reagents at 45 °C until completion. The polymer was then precipitated, washed in MeOH and dried under vacuum. ^{1}H NMR was performed on the product in benzene-d6 (Figure 8.2). δ: 0.55 ($SiCH_3$) 1.02 (1-CH_2) 1.85 (2-CH_2) 2.95 (3-CH_2) 4.05-4.55 (Fc). The peak at 0.40 ppm is a solvent residue.

3) ***PFS-MID$^+$I$^-$***: PFS-I was dissolved in a 1:2 THF:DMSO mixture, and 3 eq (relative to monomer repeat unit amount) 1-methylimidazole was added. After stirring for 24 h at 60 °C, the THF was removed by vacuum distillation and the product-DMSO solution was used in the subsequent step.

4) ***PFS-MID$^+$Cl$^-$***: PFS-MID$^+$I$^-$ dissolved in DMSO was transferred to a dialysis hose and dialysed against ultrapure water, then 4 times against 0.1 M NaCl, then against ultrapure water again. After freeze drying, an orange particulate product was retained. This material is referred to as PFS-MID$^+$ throughout the chapter.

5.5.3. Electrodeposition of methylimidazolium-poly(ferrocenylsilane)

Poly(ferrocenylsilane) methylimidazolium chloride was electrografted to gold foil and gold-silicone substrates via a method adapted from literature[25]. The polyelectrolyte was dissolved at a 5 mg mL^{-1} concentration in ionic liquid 1-ethyl-3- methylimidazolium ethyl sulfate at 80 °C. This mixture was used for electrografting in a standard three-electrode cell, where the Au foil or Au/Si wafer substrate was used as working electrode (WE), and platinum wires were used as counter (CE) and pseudo-reference electrode (RE). A cyclic voltammogram was first taken in each synthesis in order to determine the onset potential of gold reduction on the substrate surface. Electrografting was subsequently done via chronoamperometry at this potential, normally between -2 and -2.4 V vs Pt wire. 1800 s deposition time was used, after which the sample was removed from the electrografting solution and was washed with acetonitrile to remove the ungrafted polymer, then with water to remove the acetonitrile. The electrodes were dried under nitrogen flow and used in subsequent experiments.

5.5.4. Electrochemical deposition of gold nanoparticles

Gold nanoparticles were deposited from a 1 mM $KAuCl_4$ solution. 0.1 M NaCl electrolyte was added, and a classical three-electrode cell was immersed. The working electrode was the substrate (Au foil with PFS-MID+ coating), the counter electrode a platinum wire and the reference electrode Ag/AgCl. Chronoamperometric deposition of gold nanoparticles proceeded over 1800 s at –400 mV. After the AuNP deposition was finished, the electrode – denoted AuNP / PFS / Au – was removed from the solution, washed with ultrapure water, and dried under air flow.

5.5.5. Characterization

5.5.5.1. Electrochemical characterization of electrodes with cyclic voltammetry.

The electrochemical activity of all samples on gold foil (Au, PFS / Au and AuNP / PFS / Au) and on gold-silicone wafer (Au/Si and PFS / Au/Si) was characterized with cyclic voltammetry. A three-electrode cell (WE: sample, CE: Pt wire, RE: Ag/AgCl) was immersed in a 0.1 M NaCl solution and left to equilibrate over at least 10 minutes. After this, the potential was cycled 3 times between -100 and +700 mV with a sweep rate of 50 mV s^{-1}.

Similar experiments were performed with the addition of 1-3 mM ascorbic acid to determine sensing activity of different electrodes before chronoamperometric titration.

5.5.5.2. Electrochemical sensing of ascorbic acid with chronoamperometric titration

The chronoamperometric titration method for ascorbic acid sensing was adapted from literature[25]. In brief, a three-electrode cell (WE: sample, CE: Pt wire, RE: Ag/AgCl) was immersed in a 0.1 M NaCl electrolyte and left to equilibrate over at least 10 minutes. Chronoamperometric titration proceeded at -450 mV vs Ag/AgCl. 1 mM ascorbic acid solution, also containing 0.1 M NaCl, was used to increase ascorbic acid concentration in the electrolyte by 2 μM each step up to 20 μM. The increase in current was interpreted as the signal.

5.6. Bibliography

1. Feng, X., Sui, X., Hempenius, M. A. & Vancso, G. J. Electrografting of stimuli-responsive, redox active organometallic polymers to gold from ionic liquids. *J Am Chem Soc* **136**, 7865–7868 (2014).
2. Karimian, N., Zavar, M. H. A., Chamsaz, M., Turner, A. P. F. & Tiwari, A. On/off-switchable electrochemical folic acid sensor based on molecularly imprinted polymer electrode. *Electrochem commun* **36**, 92–95 (2013).
3. Shoji, R., Takeuchi, T. & Kubo, I. Atrazine Sensor Based on Molecularly Imprinted Polymer-Modified Gold Electrode. *Anal Chem* **75**, 4882–4886 (2003).
4. Espenscheid, M. W. *et al.* Sensors from polymer modified electrodes. *Journal of the Chemical Society, Faraday Transactions 1: Physical Chemistry in Condensed Phases* **82**, 1051–1070 (1986).
5. Barsan, M. M., Ghica, M. E. & Brett, C. M. A. Electrochemical sensors and biosensors based on redox polymer/carbon nanotube modified electrodes: A review. *Anal Chim Acta* **881**, 1–23 (2015).
6. Adhikari, B. & Majumdar, S. Polymers in sensor applications. *Prog Polym Sci* **29**, 699–766 (2004).
7. Qian, L., Gao, Q., Song, Y., Li, Z. & Yang, X. Layer-by-layer assembled multilayer films of redox polymers for electrocatalytic oxidation of ascorbic acid. *Sens Actuators B Chem* **107**, 303–310 (2005).
8. Podlovchenko, B. I. & Andreev, V. N. Electrocatalysis on polymer-modified electrodes. *Russian Chemical Reviews* **71**, 837–851 (2002).
9. Malinauskas, A. Electrocatalysis at conducting polymers. *Synth Met* **107**, 75–83 (1999).
10. Köleli, F., Röpke, T. & Hamann, C. H. The reduction of CO2 on polyaniline electrode in a membrane cell. *Synth Met* **140**, 65–68 (2004).
11. Wei, X. *et al.* Highly Selective Reduction of CO2 to C2+ Hydrocarbons at Copper/Polyaniline Interfaces. *ACS Catal* **10**, 4103–4111 (2020).
12. Rogers, C. *et al.* Synergistic Enhancement of Electrocatalytic CO2 Reduction with Gold Nanoparticles Embedded in Functional Graphene Nanoribbon Composite Electrodes. *J Am Chem Soc* **139**, 4052–4061 (2017).
13. Trindell, J. A., Clausmeyer, J. & Crooks, R. M. Size Stability and H2/CO Selectivity for Au Nanoparticles during Electrocatalytic CO2 Reduction. *J Am Chem Soc* **139**, 16161–16167 (2017).
14. Hernández, J., Solla-Gullón, J. & Herrero, E. Gold nanoparticles synthesized in a water-in-oil microemulsion: electrochemical characterization and effect of the surface structure on the oxygen reduction reaction. *Journal of Electroanalytical Chemistry* **574**, 185–196 (2004).
15. Hernández, J., Solla-Gullón, J., Herrero, E., Aldaz, A. & Feliu, J. M. Electrochemistry of Shape-Controlled Catalysts: Oxygen Reduction Reaction on Cubic Gold Nanoparticles. *Journal of Physical Chemistry C* **111**, 14078–14083 (2007).
16. Castañeda, M. T., Alegret, S. & Merkoçi, A. Electrochemical Sensing of DNA Using Gold Nanoparticles. *Electroanalysis* **19**, 743–753 (2007).
17. Yusoff, N., Pandikumar, A., Ramaraj, R., Lim, H. N. & Huang, N. M. Gold nanoparticle based optical and electrochemical sensing of dopamine. *Microchimica Acta 2015 182:13* **182**, 2091–2114 (2015).
18. Yu, D., Zeng, Y., Qi, Y., Zhou, T. & Shi, G. A novel electrochemical sensor for determination of dopamine based on AuNPs@SiO2 core-shell imprinted composite. *Biosens Bioelectron* **38**, 270–277 (2012).

19. Zahran, M., Khalifa, Z., Zahran, M. A. H. & Abdel Azzem, M. Recent advances in silver nanoparticle-based electrochemical sensors for determining organic pollutants in water: a review. *Mater Adv* **2**, 7350–7365 (2021).
20. Chen, S., Yuan, R., Chai, Y. & Hu, F. Electrochemical sensing of hydrogen peroxide using metal nanoparticles: a review. *Microchimica Acta 2012 180:1* **180**, 15–32 (2012).
21. Białas, K., Moschou, D., Marken, F. & Estrela, P. Electrochemical sensors based on metal nanoparticles with biocatalytic activity. *Microchimica Acta* **189**, 1–20 (2022).
22. Luo, X., Morrin, A., Killard, A. J. & Smyth, M. R. Application of Nanoparticles in Electrochemical Sensors and Biosensors. *Electroanalysis* **18**, 319–326 (2006).
23. Tang, S. *et al.* A novel label-free electrochemical sensor for Hg2+ based on the catalytic formation of metal nanoparticle. *Biosens Bioelectron* **59**, 1–5 (2014).
24. John, A. *et al.* Electrochemical sensors using conducting polymer/noble metal nanoparticle nanocomposites for the detection of various analytes: a review. *Journal of Nanostructure in Chemistry 2021 11:1* **11**, 1–31 (2021).
25. Feng, X., Sui, X., Hempenius, M. A. & Vancso, G. J. Electrografting of stimuli-responsive, redox active organometallic polymers to gold from ionic liquids. *J Am Chem Soc* **136**, 7865–7868 (2014).
26. Lin, T.-H. & Hung, W.-H. Electrochemical Deposition of Gold Nanoparticles on a Glassy Carbon Electrode Modified with Sulfanilic Acid. *J Electrochem Soc* **156**, D45 (2009).
27. Song, J. *et al.* Poly(ferrocenylsilane) electrolytes as a gold nanoparticle foundry: 'two-in-one' redox synthesis and electrosteric stabilization, and sensing applications. *Nanoscale* **9**, 19255–19262 (2017).
28. Hempenius, M. A., Brito, F. F. & Vancso, G. J. Synthesis and characterization of anionic and cationic poly(ferrocenylsilane) polyelectrolytes. *Macromolecules* **36**, 6683–6688 (2003).

6. Poly(ferrocenylsilane) coatings for biocorrosion protection

This chapter details our findings gathered over the course of a project with the aim of developing a protective iodopropyl-poly(ferrocenylsilane) (PFS-I) layer against biocorrosion to act against the redox activity of bacteria using the redox sensitivity of PFS. As described in the Materials and Methods chapter, we have spin-coated iodopropyl-poly(ferrocenylsilane) (PFS-I) from THF onto mechanically polished type 304L steel, prior to incubation with *Desulfovibrio vulgaris* over 6 weeks. The effects of bacterial colonization at different sampling times on bare and PFS-I (Scheme 6.1) covered steel are detailed below. A manuscript detailing these results is also in preparation and will be submitted for peer-review.

6.1. Introduction

Biocorrosion or microbially influenced corrosion (MIC) is the ability of certain microorganisms, most frequently bacteria, to colonize and deteriorate certain surfaces. This usually occurs via enzymatic activity or due to the chemical effects of bacterial metabolites[1]. While the exact magnitude of the economic impact of biocorrosion is unknown, it is certainly significant due to the deterioration of industrial infrastructure[2,3].

One of the most significant species causing biocorrosion is the group of sulfate reducing bacteria (SRB) in marine environments and in oil pipelines[2,4]. SRB microbes utilize the high sulfate content of these environments to generate sulfides via their metabolism. In biocorrosion, SRB supply the electrons for this reduction reaction via the oxidation of metal surfaces[2,4,5].

Like most other MIC-active bacteria, SRB act through the formation of a biofilm on the surface of metal substrates[4,5]. Accordingly, protection against the corrosive effects of these bacteria is focused on preventing the formation of biofilms[6,7]. This can be achieved in a variety of ways. The incorporation of bactericidal materials in the protective coating such as antibiotics, enzymes and silver nanoparticles is a widely researched approach. Surface morphology and chemical structure can also be tuned to give the coating biocidal properties[8,9] or to decrease the adherence of bacteria to the surface[7].

Polymers have been subjects of intense research for biocorrosion protection. From the aforementioned surface morphology tuning to employing metal nanoparticles[10] immobilized by the polymer, a wide variety of methods exist to successfully employ polymers to mitigate the effects of biocorrosion. Antibiotics can also be incorporated in the polymer to be released when in contact with the biofilm (antibiotic-releasing polymers), irreversibly immobilized on the polymer (polymeric antibiotics) or the polymer can be modified with functional groups – mostly quaternary ammonium and other cationic groups – that yield biocidal properties (antibiotic

polymers)[11]. Polymeric materials such as chitosan and other chitin derivatives[9,12] have been targeted by researchers for their potential anti-microbial properties.

Redox active moieties have also been employed for antibacterial applications, notably, antioxidants[13]. In the present work, we examined whether the reversible redox activity of a polymer, PFSs in this case study, can efficiently prevent biocorrosion. We utilized a PFS with an iodopropyl side-chain (PFS-I, Scheme 6.1) to create a water-insoluble, redox active protective polymer layer on steel surfaces. We employed these layers to protect against *Desulfovibrio vulgaris* SRB influenced biocorrosion.

Scheme 6.1. Iodopropyl-poly(ferrocenylsilane) (PFS-I) polymer used as a protective layer against *Desulfovibrio vulgaris* corrosive biofilms on steel. Note the redox active iron centre of the ferrocene unit in the main chain.

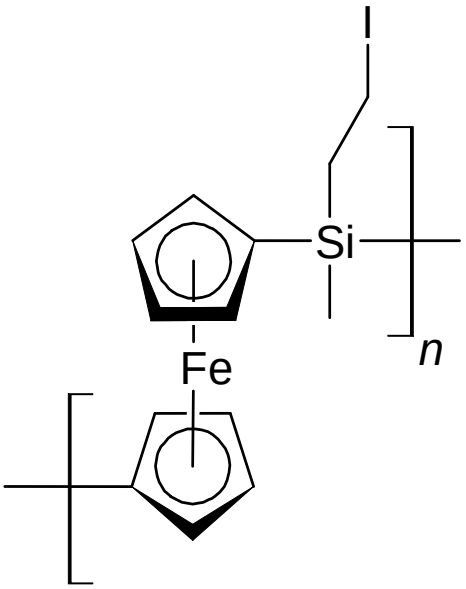

6.2. Synthesis and characterization

6.2.1. Profilometric characterization of spin-coated layers

1 mm line profiles were taken of both the coated and the bare parts of all samples at 5-5 points, in triplicate for each point. The standard deviation of the surface height from its average value was calculated and the average standard deviation was taken as the roughness of a sample. Before coating, the surface roughness was measured as (0.56 ± 0.05) µm, whereas after coating with an average loading of (88 ± 5) µg cm^{-2} PFS-I, it decreased to (0.35 ± 0.05) µm as the polymer filled in the valleys and scratches on the steel surface. Figure 6.1 shows 3-3 profiles taken on bare steel (Figure 6.1 a-c) and on PFS-I coated steel (Figure 6.1 d-f).

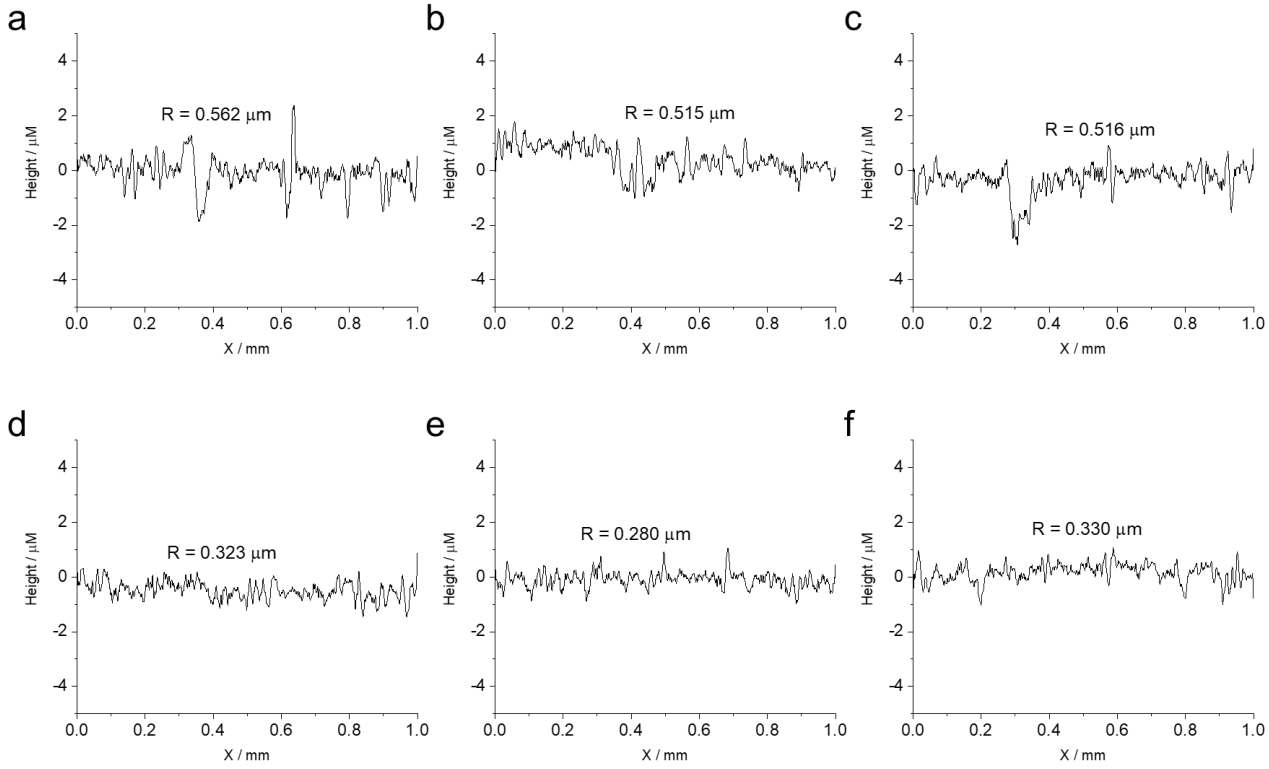

Figure 6.1. Line profiles of bare steel samples (a-c) and PFS-I coated samples (d-f) before bacterial treatment. The roughness(R) values are indicated for each profile. Note that final roughness values were calculated from measurements taken at five-five points on three separate samples after baseline correction, the ones included here serve only to illustrate the decreased roughness of PFS-I coated samples.

As seen on Figure 6.1 a-c, some scratches are still present on the bare steel samples despite the thorough mechanical polishing to a mirror sheen. However, after the deposition of the PFS-I coating, all but the largest such scratches are evened out, therefore the roughness of the coated samples is much lower. These measurements were used as basis of comparison for profilometric data acquired after incubation with bacteria.

6.3. Incubation with bacteria

6.3.1. Fluorescence microscopy on samples incubated with *Desulfovibrio vulgaris*

Over the course of the bacterial incubation with *Desulfovibrio vulgaris*, samples were taken at 48 hours, 3 weeks and 6 weeks. Fluorescence microscopy was used on samples treated with NaOCl and then stained with Syto 9 green fluorescent dye. Figure 6.2 shows pictures taken of samples after 48 hours on the bare steel part (Figure 6.2 a), the boundary (Figure 6.2 b) and on the PFS-coated part (Figure 6.2 c).

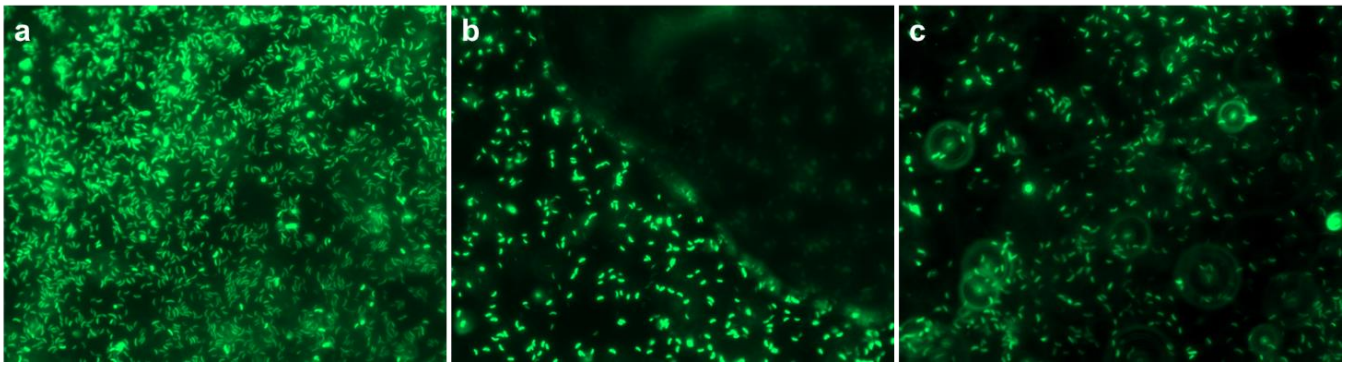

Figure 6.2. Fluorescence microscopy images of samples after 48 hours incubation with bacteria. Steel surface (a), boundary (b), and PFS-I coating (c).

As seen, bacteria proliferate on the steel surface after 48 hours of incubation (Figure 6.2 a), but a visible and immediate cutoff exists on the boundary with the PFS-I coating (Figure 6.2 b). On the coated part, bacterial colonization is slower. This is not the case after 3 weeks, as seen on Figure 6.3.

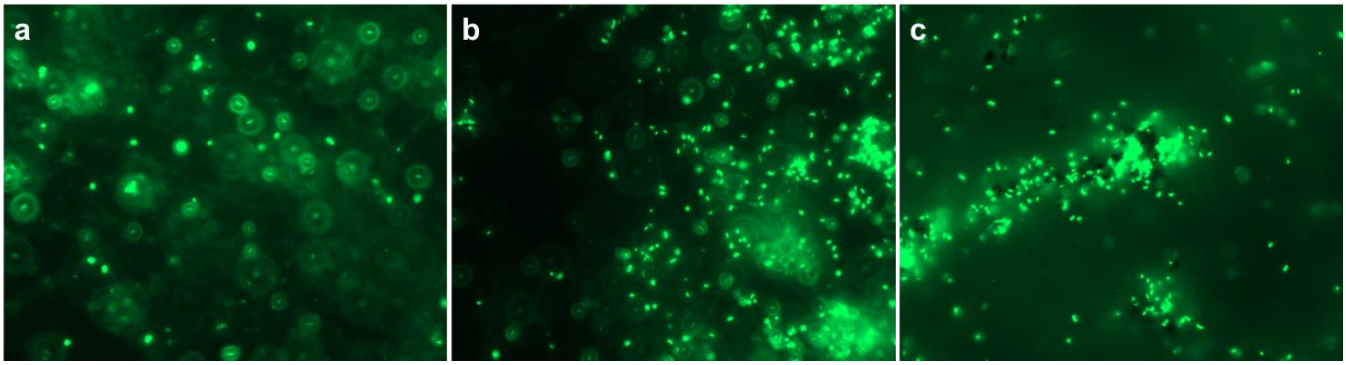

Figure 6.3. Fluorescence microscopy images of samples after 3 weeks of incubation with bacteria. Steel surface (a), boundary (b), and PFS-I coating (c).

Bacterial colonization of the bare steel part (Figure 6.3 a) is less widespread, and most bacteria are in the supernatant, as evidenced by the „halo" artifact produced by these out-of-focus bacteria. The boundary is still sharply visible (Figure 6.3 b), but in this case the dark part is the steel, as the bacteria seem to have „moved" to the PFS-I coated part. On the coating (Figure 6.3 c), FeS particles formed, possibly from interaction between *D. vulgaris* and the ferrocene in the poly(ferrocenylsilane) main chain. These particles, which are heavily colonized by bacteria, are not seen on the bare steel. Note that this tendency is opposite to that observed after 48 h, as the bacterial biofilm seemingly „migrated" from the bare steel surface to the PFS-I coating. Similar phenomena were observed after 6 weeks, as seen on Figure 6.4.

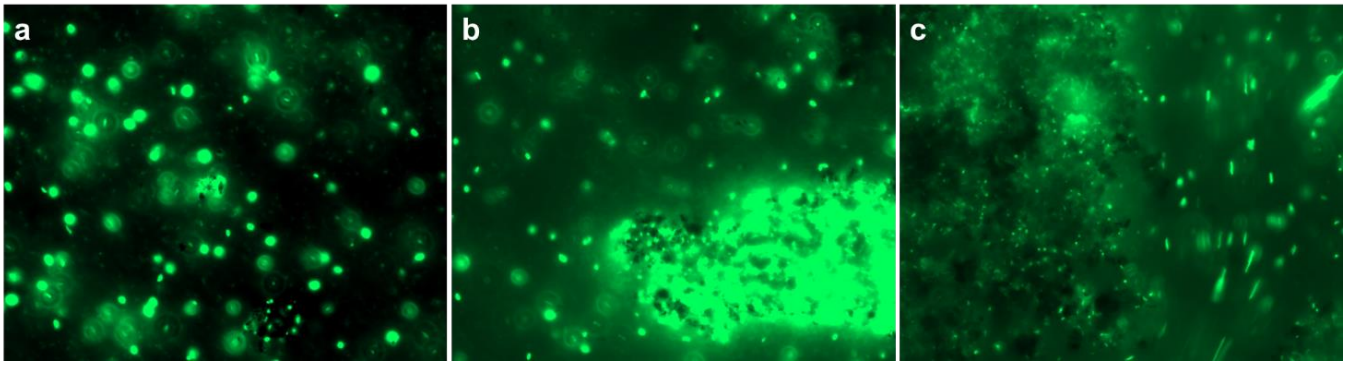

Figure 6.4. Fluorescence microscopy images of samples after 6 weeks of bacterial treatment. Steel surface (a), boundary (b), and PFS-I coating (c).

After 6 weeks, bacterial colonization of the bare steel surface has almost completely ceased (Figure 6.4 a). The steel-PFS-I boundary is clearly visible from the presence of heavily colonized FeS particles (Figure 6.4 b). Colonization of the coated part is limited to these particles, and *D. vulgaris* bacteria move freely, suspended in the supernatant between the FeS particles (Figure 6.4 c). The results indicate that the „migration" of the biofilm from the steel to the PFS-I observed at 3 weeks (Figure 6.3) is permanent. The results indicate that bacteria preferentially colonize the PFS-I surface as biofilm formation on the bare steel is hindered if the polymer is present on another part of the same sample. Once a significant colony develops on the polymer layer however, the bacteria can utilize the iron content of the ferrocene units of the main chain (see Scheme 6.1), „feeding" off the polymer, possibly without damaging the underlying steel layer.

These findings point to an interaction between *D. vulgaris* and the PFS-I coating resulting in the formation of the aforementioned FeS particles, but neither confirm nor disprove biocorrosion of the steel surface. In any case, the disappearance of bacterial colonies from the bare steel in favor of the PFS-I coating is a positive development, potentially limiting biocorrosion.

6.3.2. Profilometric characterization of samples incubated with *D. vulgaris*

Line profiles of bacteria-treated samples were taken with a method identical to blank samples described above. Figure 6.5 shows 3-3 profiles for both bare steel and PFS-I coated samples after 3 weeks of incubation. Note that PFS-I coated samples were washed with THF prior to profilometric measurements so corrosion, which would increase surface roughness through the deepening of surface scratches, can be followed. This way, all profiles are to be compared with the bare steel results for the blank samples.

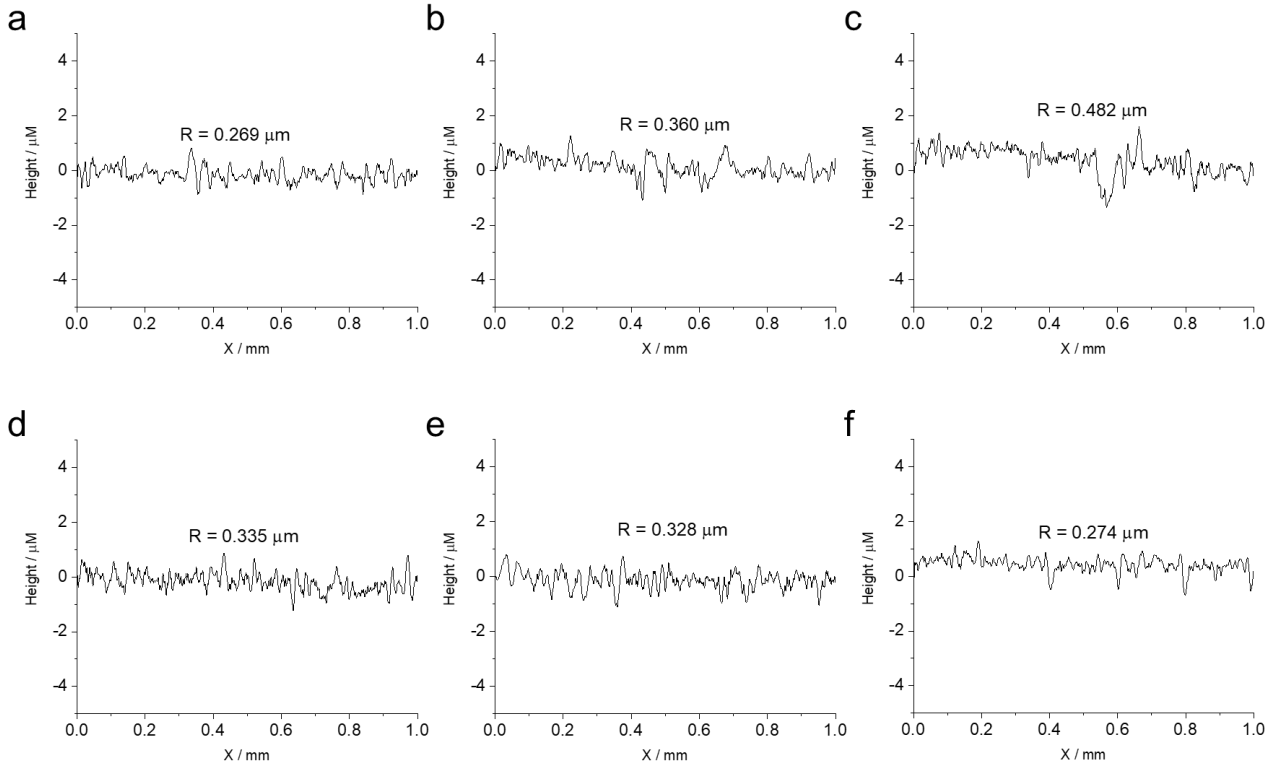

Figure 6.5. Line profiles of bare steel samples (a-c) and PFS-I coated samples (d-f) after 3 weeks of bacterial treatment. The roughness (R) values are indicated for each profile. Note that final roughness values were calculated from measurements taken at five-five points on three

separate samples after baseline correction, the ones included here serve only to illustrate the difference between the roughness of bare steel and PFS-I coated samples.

As Figure 6.5 shows, values for bare steel samples (Figure 6.5 a-c) have decreased, while those for the PFS-I coated surfaces remained unchanged. Analysis of the full dataset gives the same result, as the steel surface roughness was calculated as (0.35 ± 0.04) μm, only 63 % of that before the treatment. Similar phenomena were observed on the PFS-I coated samples, their roughness is almost identical to that of bare steel samples at (0.33 ± 0.004) μm. As biocorrosion is expected to increase roughness as bacteria convert the iron on the surface into FeS particles, decreased roughness indicates that no significant biocorrosion occurred. The decreased R values can come from leftover (dead) bacterial residues after treatment. This shows that despite the growth of bacterial colonies on the surface, as observed with fluorescence microscopy (Figures 6.2-6.5), and even the appearance of FeS precipitates on the PFS-I layer, after a thorough washing the PFS surface remained essentially untouched, free from bacterial residues.

Similar experiments were performed after 6 weeks of *D. vulgaris* incubation, the results of which are presented on Figure 6.6 below.

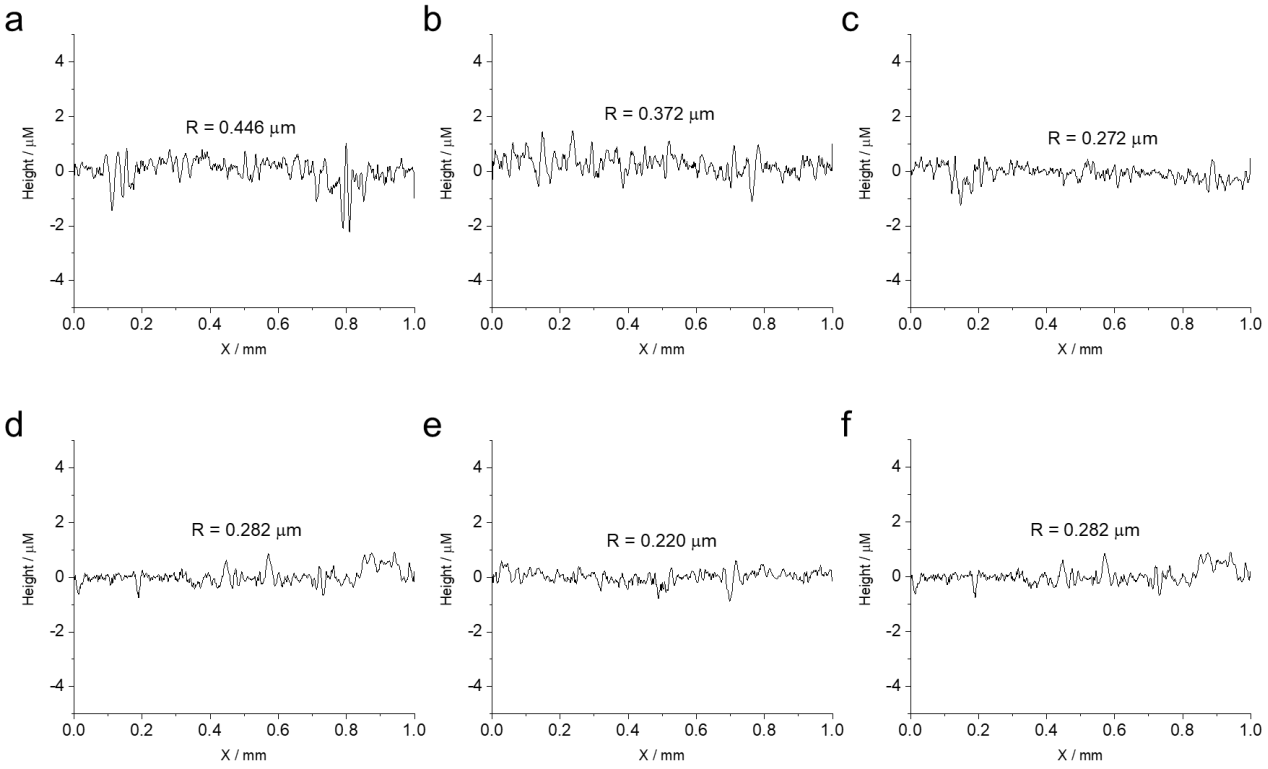

Figure 6.6. Line profiles of bare steel samples (a-c) and PFS-I coated samples (d-f) after 3 6 weeks of bacterial treatment. The roughness (R) values are indicated for each profile. Note that final roughness values were calculated from a higher number of samples after baseline correction, the ones included here serve only to illustrate the difference between the roughness of bare steel and PFS-I coated samples.

After 6 weeks of incubation, the roughness of bare steel samples was (0.46 ± 0.01) µm, significantly higher than the (0.35 ± 0.04) µm measured at 3 weeks. This indicates biocorrosion of the surface, even though fluorescence microscopy shows low amounts of bacteria on the bare steel surface at 6 weeks. As these bacteria have unlimited access to the underlying steel substrate, biocorrosion is eventually bound to occur, hence the increased roughness. In contrast, the PFS-I coated samples exhibit a roughness of (0.26 ± 0.01) µm, lower than the (0.33 ± 0.004) µm value after 3 weeks of treatment. We can therefore say that despite significant FeS particle

buildup on the PFS-I coated surfaces (Figure 6.4 b, c) indicating bacterial oxidation of the polymer layer itself, *D. vulgaris* activity does not extend to the underlying steel surface. Over all profilometric experiments, it can be stated that PFS-I protected surfaces exhibit lower roughness that remains constant over the course of the bacterial incubation, while the roughness of bare steel varies and is more susceptible to the presence of bacterial colonies. This supports our theory that the PFS-I coating is resistant to the corrosive activity of *D. vulgaris*, as the reversible oxidation of the ferrocene centres does not deteriorate the polymer itself, despite widespread colonization of the PFS-I surface.

6.3.3. Bacterial incubation of poly(ferrocenylsilane)s without substrate

Our findings in the previous section established the unique behavior of D. vulgaris bacteria in contact with PFS layers deposited on steel. Three different samples of PFS-I were immersed in an identical bacterial growth medium as that for the previously described PFS-I/steel samples. In addition, a water-soluble anionic polyelectrolyte poly(ferrocenylsilane), $PFS^{-}N_{3\ (20\ \%)}$, was also tested as to whether it promotes bacterial growth. We performed bacterial growth tests and measured the absorbance of the solution, which is correlated with the amount of bacteria present therein. The results of these experiments are shown on Figure 6.7.

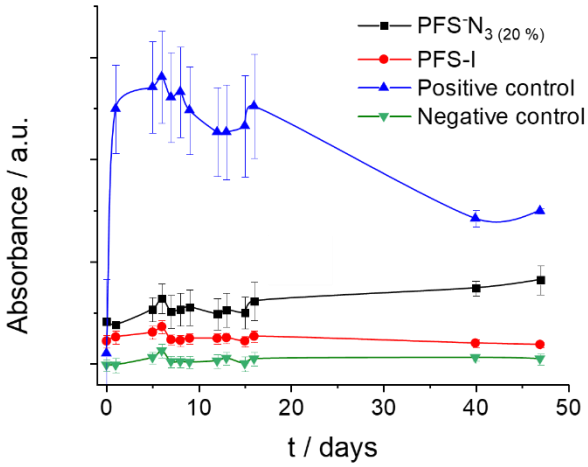

Figure 6.7. Results of *D. vulgaris* growth studies without steel substrate over 47 days. Positive control of bacterial growth is shown in blue, while negative control without bacteria is in green. The lines are for eye guidance purposes only.

As Figure 6.7 shows, both the water-soluble (black) and the insoluble (red) PFSs show hindered bacterial growth without the steel substrate, although the water-soluble PFS exhibits a longer growth period than the positive control and reaches about 60 % of the absorbance of the positive control by the end of the testing period. The easier accessibility of the dissolved polyelectrolyte compared to the solid PFS-I particles might be the reason for this, as the bacteria could oxidise the ferrocene centres of the PFS-$N_{3\ (20\ \%)}$ at a greater rate.

It is evident that *D. vulgaris*, which proliferated on PFS-I-coated steel surfaces, does not favor the same PFS-I without the underlying metal substrate. The catalytic activity of PFS-based materials has been shown previously[14], where the reversible Fc^{+}/Fc redox pair may act as a catalyst for complex electron-transfer reactions. This might be the case on the PFS-I/steel system, where electrons of the bulk steel are transferred at a greater rate to the electroactive *Desulfovibrio* biofilm[15] if the intermediate PFS-I layer is present. At the same time, the ferrocene centres of the polymer may help with the recovery of electrons on the metal-polymer

interface, hence the apparent protection of the steel surface. This however is not the case with the particulate PFS-I, where, in addition to the absence of a bulk metal as an electron source, bacteria only have access to the ferrocene centres on the surface of the polymer particles, with the majority of the polymer chains remaining hidden to the biofilm.

6.4. Conclusion

In this chapter we presented a method for the preparation of iodopropyl-poly(ferrocenylsilane) (PFS-I) layers for promoting biocorrosion resistant properties against *Desulfovibrio vulgaris* on steel substrates. We deposited the layers via spin-coating and utilized profilometry and fluorescence microscopy for the characterization of the sample surfaces before and after the biocorrosion experiments. We have concluded that the bacteria colonize the PFS-I layer preferentially compared to the blank steel, but no corrosion of the underlying steel layer occurs over at least six weeks. We have also noticed the growth of FeS particles on the surface of the PFS-I layer, the iron for which is possibly sourced from the ferrocene centres of the polymer. Furthermore, we have tested bacterial proliferation without steel in the presence of water-soluble and water-insoluble PFS moieties. In these tests we found that, while the bacteria grew slower with both polymers than with the positive control, the water-soluble $PFS^{-}N_{3\ (20\ \%)}$ is easier to access, promoting some bacterial growth. On the other hand, PFS-I without the steel substrate does not promote the growth of bacteria, showing that the interaction of steel, PFS-I and *D. vulgaris* is necessary for the development of the biofilm on the polymer surface, but this biofilm does not damage the underlying metal.

6.5. Materials and Methods

6.5.1. Materials

Dicyclohexano-18-crown-6 (98 %), 1-iodopropane (99 %), and sodium chloride (NaCl, 99.5 %), were purchased from Sigma-Aldrich (Saint-Quentin-Fallavier, France)**.** Tetrahydrofuran (THF, anhydrous), potassium chloride (KCl, 99.5 %) and methanol (MeOH, technical), were procured from VWR (Rosny-sous-Bois, France).

6.5.2. Poly(ferrocenylsilane) synthesis

The poly(ferrocenylsilanes) used in this study were prepared in a multi-step procedure shown on Scheme 6.2.

Scheme 6.2. Reaction steps used to prepare the polymers presented in this chapter. Steps 1) through 4) are detailed below.

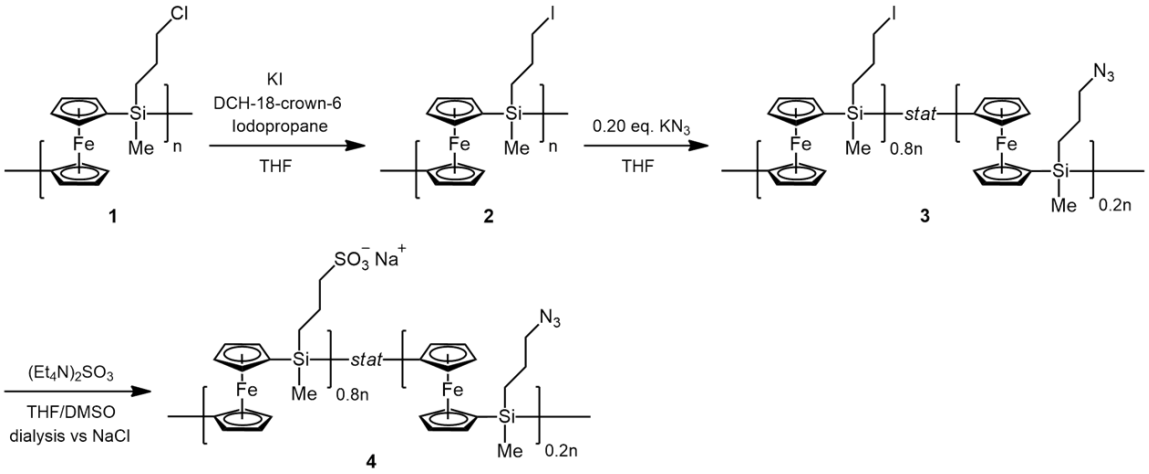

1) ***PFS-Cl***: Poly(ferrocenyl(3-chloropropyl)methylsilane) was synthesized via a previously published[16] procedure in a transition-metal-catalyzed ring-opening polymerization reaction from a precursor ferrocenylsilane containing methyl and chloropropyl-bearing [1] silaferrocenophane monomer side-chains. ^{1}H NMR was performed on the polymer product in

benzene-d6 (Figure 8.1). δ: 0.55 ($SiCH_3$) 1.10 (1-CH_2) 1.80 (2-CH_2) 3.25 (3-CH_2) 4.05-4.55 (Fc). The peak at 0.40 ppm represents solvent residues.

2) ***PFS-I***: A mixture in THF containing PFS-Cl, potassium iodide (KI, 1 equivalent (eq) respective to PFS repeat units), dicyclohexano-18-crown-6 (0.25 eq), and iodopropane (0.025 eq) was stirred at 45 °C for at least a week. The polymer was then precipitated in MeOH or EtOH, dried, and subsequently the reaction was continued with the same reagents at 45 °C until completion. The polymer was then precipitated, washed in MeOH and dried under vacuum. ^{1}H NMR was performed on the product in benzene-d6 (Figure 8.2). δ: 0.55 ($SiCH_3$) 1.02 (1-CH_2) 1.85 (2-CH_2) 2.95 (3-CH_2) 4.05-4.55 (Fc). The peak at 0.40 ppm is a solvent residue.

3) ***PFS-I/N_3 (20 %)***: PFS-I was dissolved in THF, then 0.2 eq potassium azide (KN_3) dissolved in DMSO was added. The THF:DMSO ratio in the mixture was set to 2:1. After overnight stirring at 45 °C, the resulting polymer was precipitated, washed and dried under vacuum. ^{1}H NMR was performed in benzene-d6 (Figure 8.3). δ: 0.55 ($SiCH_3$) 0.95 (1-CH_2 (N_3)) 1.02 (1-CH_2 (I)) 1.60 (2-CH_2 (N_3)) 1.85 (2-CH_2 (I)) 2.85 (3-CH_2 (N_3)) 2.95 (3-CH_2 (I)) 4.05-4.50 (Fc). The peak at 0.40 ppm is a solvent residue.

4) ***PFS$^-$$N_3$ (20 %)***: PFS-I/N_3 (20 %) was dissolved in THF, then the DMSO solution containing an excess of $(Et_4N)_2SO_3$ (see equation 8.1 and attached description in the Supplementary Information for synthesis of $(Et_4N)_2SO_3$) was added and the solvent ratio of THF:DMSO was set to 5:1. After stirring at 35 °C for 3 days, the mixture was transferred to a dialysis hose and dialyzed against ultrapure water, 3 times against 0.1 M NaCl solution, then against water. The resulting solution was freeze-dried then vacuum dried. ^{1}H NMR was performed in D_2O (Figure 8.4). δ: 0.55 ($SiCH_3$) 0.85 (1-CH_2 (N_3)) 0.95 (1-CH_2) 1.50 (2-CH_2 (N_3)) 1.78 (2-CH_2) 3.90-4.55 (Fc). The peaks at 1.10-1.40; 2.55 and 3.20-3.70 ppm are solvent residues. The 3-CH_2 peaks expected at 3.40 ppm are obscured by the solvent residue signal.

6.5.3. Biocorrosion sample preparation

Preparation of PFS-I coatings on steel surfaces. PFS-I was dissolved in THF at a 30 mg mL^{-1} concentration, and this solution was then used for spin-coating. A 3 cm x 3 cm piece of mechanically polished steel (type 304L) was vacuum-fixed onto the spin-coater's rotor and 3 cycles of static spin-coating were performed. Each cycle lasted 30 s, with a 2000 rpm (revolutions per minute) maximum spin velocity and 1000 rpm s^{-1} acceleration / deceleration rate. An average PFS-I loading of (88 ± 5) µg cm^{-2} was achieved this way. The coated steel samples were cut, and half of each sample was washed several times with THF to remove the PFS-I coating from that part. This was necessary so that biocorrosion activity could be compared between the coated and the washed parts. Samples were subsequently used in the profilometry and biocorrosion experiments.

Profilometry measurements on steel samples. Roughness was measured with optical profilometry apparatus on both the PFS-I coated and the bare steel surface of each sample. Five points were selected for the coated and the non-coated parts each, and surface morphology was measured in a 1 mm line at every point. The standard deviation of the surface height from the average was then taken as the roughness in that line. This was then averaged to yield a mean roughness of a sample. Samples before the biocorrosion measurements were measured this way and so were samples after 3 and 6 weeks of incubation with *D. vulgaris*.

6.5.4. Biocorrosion experiments

Desulfovibrio medium. Three solutions, coded A, B and C, were prepared. Solution A contained 0.5 g K_2HPO_4, 1-1 g of NH_4Cl, Na_2SO_4 and yeast extract, 2-2 g of $MgSO_4$ x 7 H_2O and Na-lactate, 0.1 g $CaCl_2$ x 2 H_2O and 0.5 mL 0.1 % (w/v) Na-resazurin solution in 980 mL

distilled water. Solution B consisted of 0.5 g $FeSO_4$ x 7 H_2O dissolved in 10 mL distilled water, and solution C contained 0.1 g of Na-thioglycolate and 0.1 g of ascorbic acid in 10 mL water.

Solution A was brought to a boil and subsequently cooled back to room temperature under nitrogen gas bubbling. Solutions B and C were then added, and the pH was adjusted to 7.8 with NaOH. 5-5 mL of mixture was distributed into the culture tubes under N2 atmosphere and autoclaved at 121 °C for 15 min.

Biocorrosion culture tests. *Desulfovibrio vulgaris* was introduced to the tubes and the PFS-coated steel samples were submerged in the solution. The tubes were placed in an autoclave at 37 °C and samples were taken at 48 h, as well as 3 and 6 weeks. For each sample, the bacteria that developed on the steel sample surface were treated with NaOCl,. The samples were then observed with fluorescence microscopy.Bacterial growth tests without steel substrate were performed in an analogous manner to that described above, but in this case either a given amount of solid PFS-I particles was submerged in the growth medium, or a given amount of $PFS^{-}N_{3\,(20\,\%)}$ solution was added to it. Lacking the solid substrate of the previous tests, bacterial proliferation in these systems was followed by measuring the absorbance of the growth medium. This absorbance increases in correlation with the growth of bacteria, thus measuring absorbance yields information on the relative proliferation of bacteria in different systems.

Fluorescence microscopy measurements. One sample (half bare steel, half PFS-I coated) was selected at each measurement step. After the NaOCl treatment described above, bacteria on the sample surface were treated with SYTO 9 green fluorescent nucleic acid stain and placed under a fluorescent microscope. Irradiation with green light induced fluorescence in the SYTO 9 – bacterial DNA complexes, making the bacteria clearly visible. Images were taken on the steel surface, the PFS-I coating, and on the boundary between the two. Relative proliferation of bacteria was assessed based on the intensity of fluorescence.

6.6. Bibliography

1. Beech, I. B. & Gaylarde, C. C. Recent advances in the study of biocorrosion: an overview. *Revista de Microbiologia* **30**, 117–190 (1999).
2. Procópio, L. Microbially induced corrosion impacts on the oil industry. *Arch Microbiol* **204**, 1–6 (2022).
3. Narenkumar, J. *et al.* Impact and Role of Bacterial Communities on Biocorrosion of Metals Used in the Processing Industry. *ACS Omega* **4**, 21353–21360 (2019).
4. Hamilton, W. A. Sulphate-reducing bacteria and anaerobic corrosion. *Ann. Rev. Microbiol* **39**, 195–217 (1985).
5. Hamilton, W. A. Sulphate-Reducing Bacteria and Their Role in Biocorrosion. *Biofouling and Biocorrosion in Industrial Water Systems* 187–193 (1991).
6. Khatoon, Z. *et al.* Bacterial biofilm formation on implantable devices and approaches to its treatment and prevention. *Heliyon* **4**, e01067 (2018).
7. Jansen, B. & Kohnen, W. Prevention of biofilm formation by polymer modification. *J Ind Microbiol* **15**, 391–396 (1995).
8. Boulmedais, F. *et al.* Polyelectrolyte multilayer films with pegylated polypeptides as a new type of anti-microbial protection for biomaterials. *Biomaterials* **25**, 2003–2011 (2004).
9. Iqbal, M. H. *et al.* Bactericidal and bioinspired chitin-based anisotropic layer-by-layer brushed-nanocoating. *Appl Mater Today* **32**, 101816 (2023).
10. Palza, H. Antimicrobial Polymers with Metal Nanoparticles. *International Journal of Molecular Sciences 2015, Vol. 16, Pages 2099-2116* **16**, 2099–2116 (2015).
11. Chen, A., Peng, H., Blakey, I. & Whittaker, A. K. Biocidal Polymers: A Mechanistic Overview. (2017) doi:10.1080/15583724.2016.1223131.
12. Rasheed, P. A. *et al.* Controlling the biocorrosion of sulfate-reducing bacteria (SRB) on carbon steel using ZnO/chitosan nanocomposite as an eco-friendly biocide. *Corros Sci* **148**, 397–406 (2019).
13. Ong, K. S., Mawang, C. I., Daniel-Jambun, D., Lim, Y. Y. & Lee, S. M. Current anti-biofilm strategies and potential of antioxidants in biofilm control. *Expert Rev Anti Infect Ther* **16**, 855–864 (2018).
14. Halmagyi, T., Hao, J., Hempenius, M. A. & Vancso, G. J. Poly(ferrocenylsilane) Hydrogels as a Foundry for Metal Nanoparticle Synthesis by Direct Reduction of Electrolytes via a Catalytic Route. *ACS Appl Nano Mater* **5**, 8868–8874 (2022).
15. Cordas, C. M., Guerra, L. T., Xavier, C. & Moura, J. J. G. Electroactive biofilms of sulphate reducing bacteria. *Electrochim Acta* **54**, 29–34 (2008).
16. Hempenius, M. A., Brito, F. F. & Vancso, G. J. Synthesis and characterization of anionic and cationic poly(ferrocenylsilane) polyelectrolytes. *Macromolecules* **36**, 6683–6688 (2003).

7. Conclusions and Outlook

In this doctoral thesis, we demonstrated the versatile nature of poly(ferrocenylsilane) (PFS) metallopolymers through the synthesis and characterization of a variety of functional (bio)interfaces. PFSs are a fascinating family of polymers with a main chain of alternating ferrocene and silane units. The iron center of the ferrocene can be reversibly oxidized and reduced in a Fe^{III}/Fe^{II} redox couple, thus all repeat units of the polymers possess one redox active unit. On the other hand, the side-chains of the silane units can be changed in post-polymerization modification reactions, potentially yielding PFSs with vastly different physical and chemical properties. The starting point of our investigations was in all cases a PFS with a chloropropyl side-chain, denoted as PFS-Cl. The chloride group of this polymer was then changed to a more reactive – and therefore more malleable – iodopropyl moiety in a nucleophilic substitution reaction. From this polymer, denoted as PFS-I, we could synthesize a range of ionic, water-soluble PFSs through a variety of chemical modifications. Both anionic and cationic groups were introduced in the PFS side-chains, yielding anionic and cationic polyelectrolytes, respectively. In addition, PFS-I itself was utilized in the preparation of a biocorrosion-protective thin film on steel substrates. A more detailed explanation of the results presented in this thesis can be found below.

In **Chapter 1** of present work a short introduction of the properties and applications of poly(ferrocenylsilanes) was presented and the contents of the subsequent chapters were briefly summarized.

Chapter 2 provides a detailed description of previous literature in fields relevant to this thesis. Prior art was collected on the materials chemistry of stimulus responsive polymers, colloidal stability and stabilization notably regarding polyelectrolytes and nanoparticles, and biocorrosion protection of metal surfaces with polymeric and redox-responsive materials. This

chapter also outlines the relevance of these topics to present work and the possible avenues for further research.

After the first two introductory chapters, the next four detail our investigations on utilizing the versatility of PFSs for the preparation of (bio)interfaces and their various applications. Solubility in polar solvents was achieved via anionic sulfonate (*Chapter 3, 4*) and carboxylate (*Chapter 4*) and cationic methylimidazolium (*Chapter 5*) groups, whereas the PFS-I platform can be utilized in nonpolar solvent (*Chapter 6*). The introduction of different side-chains in the same polymer was explored to give multiple functionalities to PFS. The introduction of azide groups next to ionic groups makes the PFS click-capable, enabling the facile connection of biomolecules to the polymer, and through precise tuning of the ratio of azide-substituted side-chains, polymer solubility in water can also be preserved (*Chapter 3*). The stabilization of colloidal nanoparticles with PFSs was also explored (*Chapter 3, 4*).

In **Chapter 3**, poly(ferrocenylsilanes) were co-modified with azide and sulfonate side groups to yield a click-capable anionic polyelectrolyte. This polymer, denoted as PFS-$N_{3(20\ \%)}$ due to its content of 20 % azide and 80 % sulfonate side groups, was then used for the synthesis and stabilization of gold nanoparticles, and the resulting composite was denoted as PFS-AuNP. Thrombin-specific oligonucleotide aptamers were subsequently grafted to the polymer via a strain-promoted azide-alkyne cycloaddition (SPAAC) reaction and the successful grafting was confirmed through a novel enzymatic digestion method. In this method, two exonuclease enzymes with opposite directional activity (Exonuclease I and RecJf) were utilized to digest the aptamer, the 5' end of which was modified with a cyclic alkyne. If the SPAAC reaction was successful, this end became inaccessible, and RecJf digestion failed. As the digestion could be monitored via fluorescence spectroscopy, it was possible to confirm the grafting of the aptamer to the polymer. Successful grafting gave rise to an aptamer-polymer-gold nanoparticle complex,

denoted as aptamer-AuNP. The colloidal stability of aptamer-AuNPs was assessed through dynamic light scattering (DLS) experiments. The aptamer-AuNP shows an order of magnitude greater stability in high ionic strength environments than the PFS-AuNP due to the electrosteric stabilization effects exerted by both the metallopolymer and the aptamer. The functionality of the grafted aptamers was also confirmed with DLS measurements. As the aptamer-target interaction leads to the collapse of the secondary structure of the oligonucleotide, the steric stabilization effect diminishes, making the nanoparticles more susceptible to aggregation. We exploited this effect to confirm the sensitivity of the aptamer-AuNPs towards thrombin with a limit of detection (LOD) of 0.5 μM. This interaction is also selective to thrombin as confirmed by control experiments with beta-lactoglobulin. This chapter is thus the first report describing functional grafting and subsequent characterization of an aptamer to poly(ferrocenylsilane) polyelectrolyte-stabilized gold nanoparticles.

Chapter 4 contains our investigations on the electrosteric stabilizing effect of PFS polyelectrolytes adsorbed on amidine latex (AL) nanoparticles. The synthesis and characterization of an anionic PFS polyelectrolyte containing 85 % sulfonate and 15 % carboxylate side groups denoted as $PFS^{-}_{COOH(15\,\%)}$ is described. This polymer was then adsorbed on AL nanoparticles with a positive initial surface charge, resulting in charge reversal and the formulation of PFS-amidine latex particles of a negative surface charge, denoted as p-AL. Laser doppler electrophoresis (LDE) and DLS were employed to monitor the zeta potential and the hydrodynamic size of particles, respectively. The colloidal stability and surface charge of the PFS-AL system was monitored at different PFS doses and it was observed that stability is high at very low or very high PFS concentrations, while around the charge reversal or isoelectric point (IEP) the nanoparticles aggregated, their stability ratio plummeting to zero. The minimum PFS concentration required to achieve maximum negative surface charge, the adsorption

saturation plateau, was also determined. The colloidal stability of p-AL particles was also investigated in high ionic strength environments and the critical coagulation concentration (CCC) of the p-AL particles was found to be almost an order of magnitude higher than that of bare AL particles, highlighting the electrosteric stabilization effect of anionic PFS polyelectrolytes. The effect of the metallopolymer's redox activity on p-AL stability was also investigated through reacting the composite with ascorbic acid (AA). The hydrodynamic size and the zeta potential of the particles remained constant regardless of ascorbic acid concentration, showing no interaction between the PFS and AA. In conclusion, this chapter summarizes our investigations on the excellent electrosteric stabilization properties of anionic poly(ferrocenylsilane) polyelectrolytes.

Chapter 5 summarizes our work on the synthesis and characterization of AuNP-PFS-gold electrodes as well as their application in electrochemical detection of antioxidants. A cationic polyelectrolyte poly(ferrocenylsilane) was synthesized via the introduction of methylimidazolium chloride (MID^+Cl^-) groups on the side-chains of the polymer. The product, denoted as PFS-MID^+Cl^- was subsequently electrochemically grafted to gold foil and gold/silicon substrates (denoted simply as Au and Au/Si, respectively) through the electrochemical reduction of gold atoms on the electrode surface, resulting in the formation of a PFS-MID^+Au^- complex macroscopically understood as the strong electrostatic immobilization of the polymer on the surface. We developed on existing literature by electrochemically depositing gold nanoparticles on the PFS-grafted electrodes. The electrochemical behavior of these nanocomposite electrodes was characterized via cyclic voltammetry as well as chronoamperometric titration sensing of ascorbic acid (AA). It was found that both the polymer grafting and the AuNP deposition modifies and increases the electroactivity of the electrodes, and all samples had a significantly greater sensitivity towards

AA than the bare Au and Au/Si electrodes. This chapter thus summarizes of our experiments centered on the synthesis and characterization of a novel AuNP-PFS-gold nanocomposite electrode.

In **Chapter 6**, we describe thin film deposition of iodopropyl-poly(ferrocenylsilane) (PFS-I) on steel surfaces, and this polymer layer's performance in protection against microbially influenced corrosion (MIC) by *Desulfovibrio vulgaris* sulfate reducing bacteria (SRB). We synthesized PFS-I via nucleophilic substitution of PFS-Cl and deposited the polymer from tetrahydrofuran (THF) onto mechanically polished steel substrates. We characterized the surfaces before and after deposition via profilometry and examined biofilm formation and biocorrosion by *D. vulgaris* employing both profilometry and fluorescence microscopy techniques. It was found that while the bacteria proliferate on the PFS, presumably due to the redox activity of the polymer providing the SRB with electrons to be used in their metabolism, the underlying steel layer was not damaged, as its roughness remained constant over the 6 weeks of bacterial treatment. This chapter is therefore a summary of our investigations on the biocorrosion protective properties of a redox active polymer PFS-I.

In conclusion, the redox activity, stimuli responsiveness and facile modification of PFSs opens the door to a variety of applications. In the future, these applications could be further explored through either the optimization of PFS synthesis and modification methods described in present work or in other literature, or through the development of novel PFS systems. As the range of possible PFS side-chain modifications is essentially infinite, the possibilities of applying this family of polymers for the preparation of functional (bio)interfaces are virtually endless and are limited only by imagination.

8. Supplementary Information

Synthesis of $(Et_4N)_2SO_3$. According to equation 8.1, a 1:2 mixture of dimethyl sulfite and tetraethylammonium hydroxide was prepared in DMSO and stirred for at least 5 h at room temperature. The successful reaction was indicated by the appearance of a white precipitate. The solution was concentrated under vacuum to remove residual solvents and the $(Et_4N)_2SO_3$ in DMSO was directly used in subsequent synthesis steps.

$$Me_2SO_3 + 2\ Et_4NOH \rightarrow (Et_4N)_2SO_3 + 2\ MeOH \quad \text{(Equation 8.1)}$$

NMR data. Poly(ferrocenylsilane) synthesis steps were verified with ^{1}H NMR (in benzene-d6 of in D_2O, depending on solubility). The strain-promoted azide-alkyne cycloaddition was also followed with ^{13}C NMR in D_2O. The annotation of relevant atoms for all spectra is shown on Scheme 8.1.

Scheme 8.1. m-dPEG$_{12}$-DBCO (a) and PFS Huisgen product (b) with NMR-relevant atoms marked.

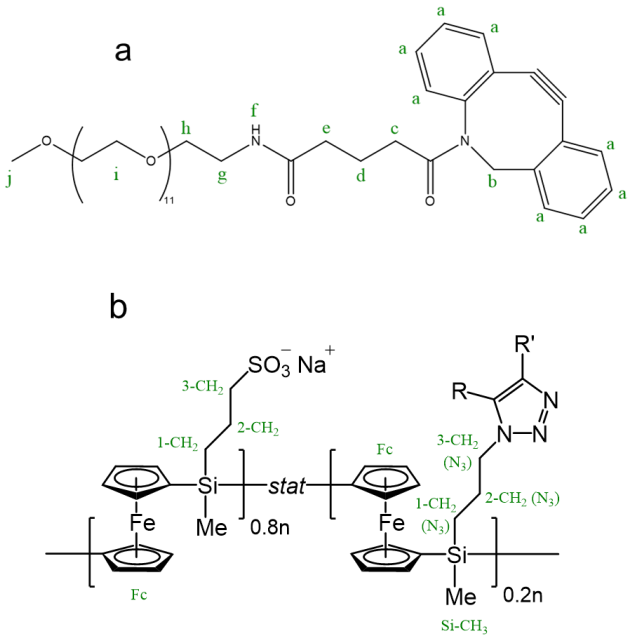

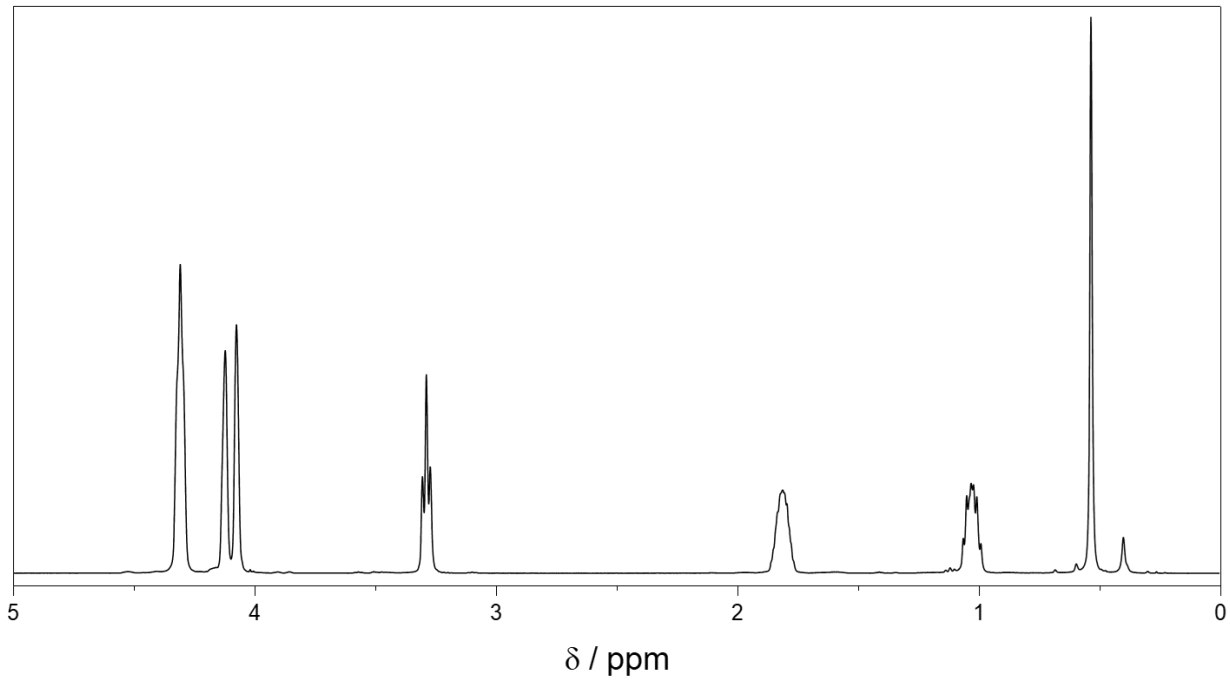

Figure 8.1. ^{1}H NMR spectrum of PFS-Cl in benzene-d6

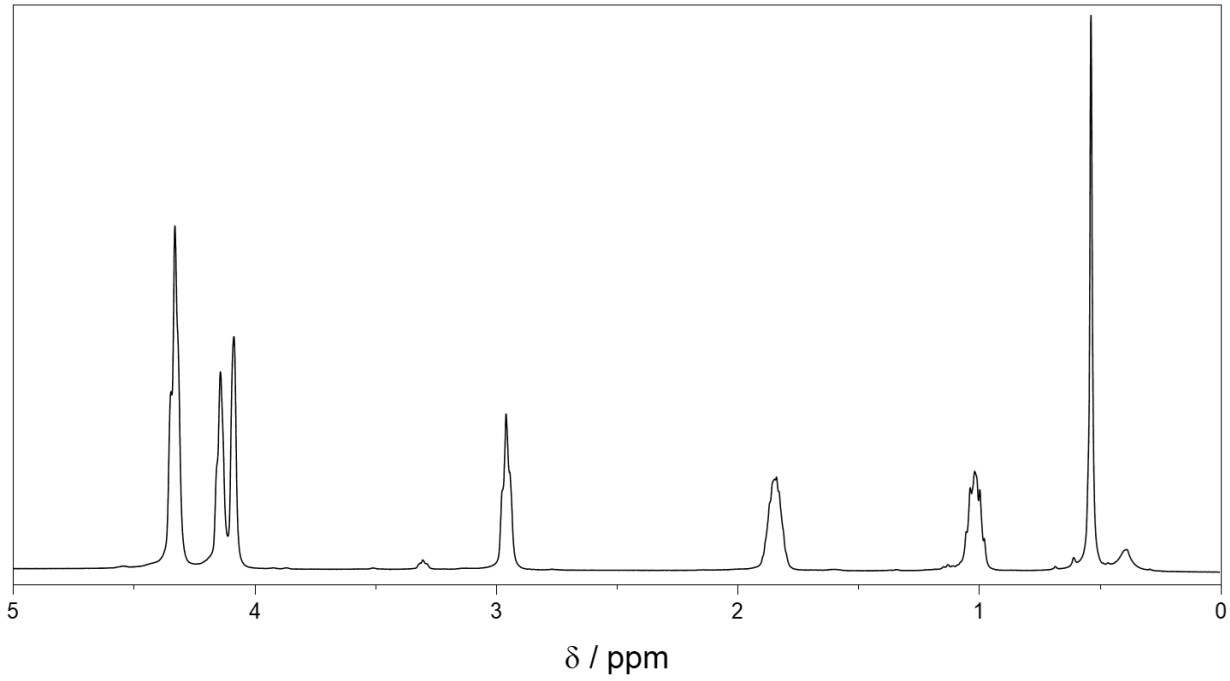

Figure 8.2. ^{1}H NMR spectrum of PFS-I in benzene-d6.

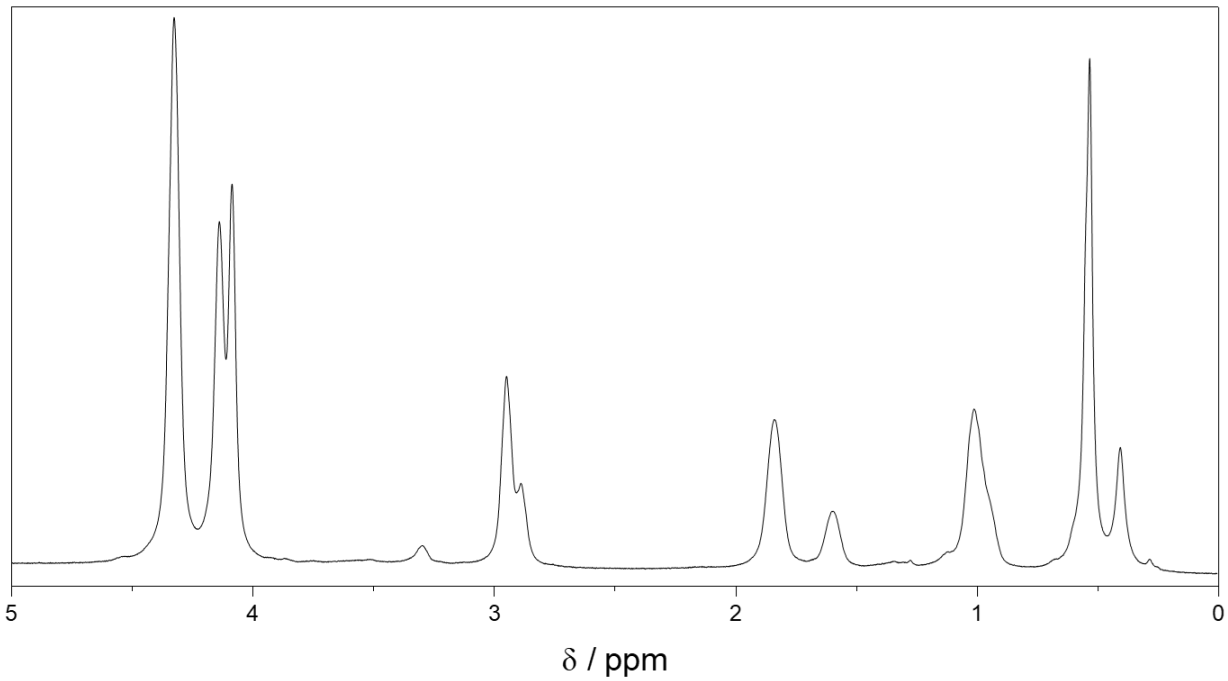

Figure 8.3. ^{1}H NMR spectrum of PFS-I/$N_{3(20\,\%)}$ in benzene-d6.

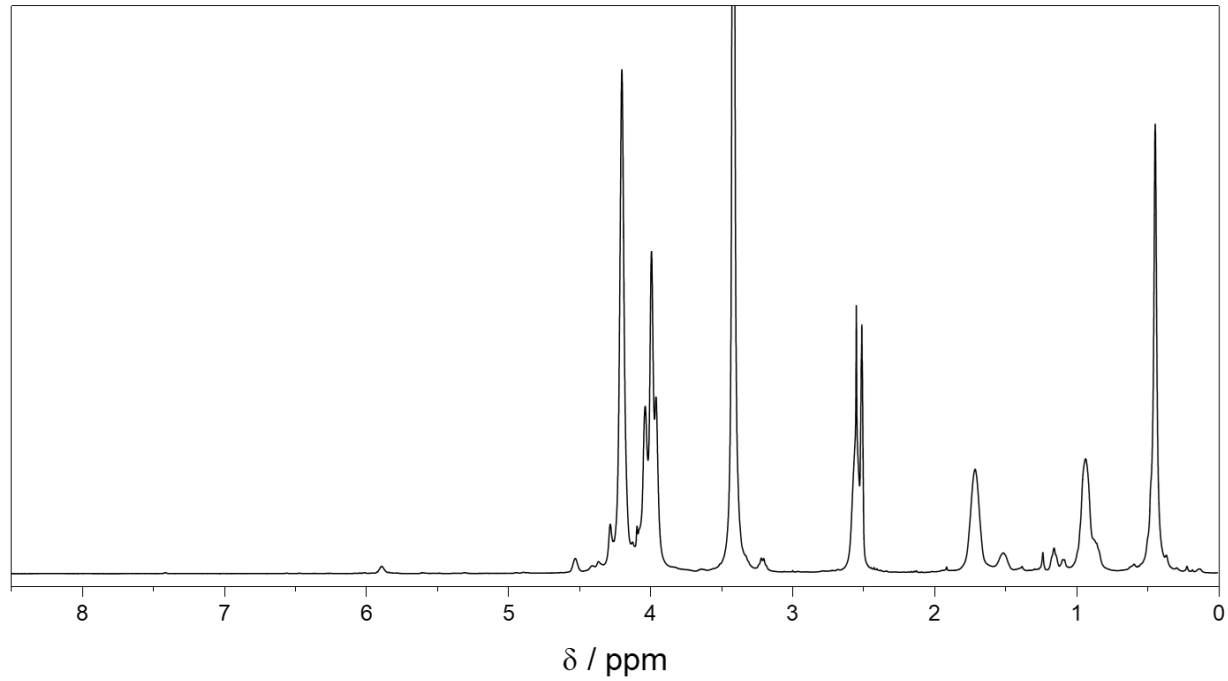

Figure 8.4. ^{1}H NMR spectrum of PFS^{-}/$N_{3(20\,\%)}$ in D_2O.

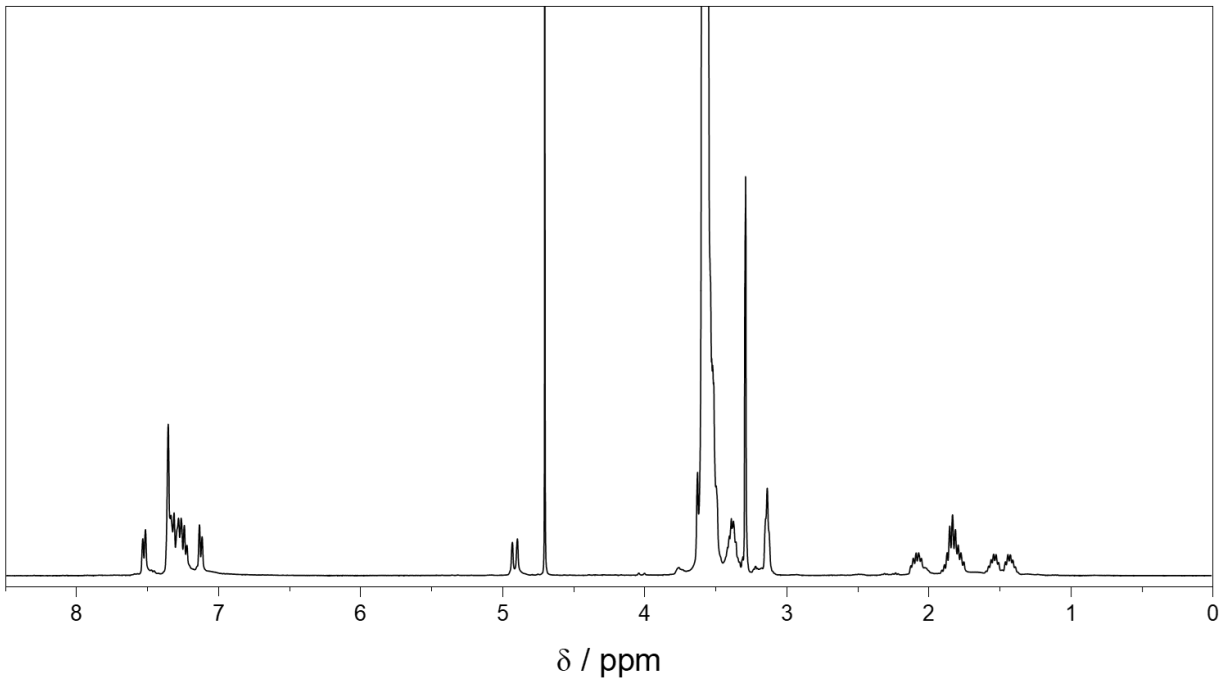

Figure 8.5. ^{1}H NMR spectrum of m-dPEG$_{12}$-DBCO in DMSO-d6. δ: 1.44 (c); 1.55 (c); 1.70 (d); 1.84 (e+d); 2.21 (e); 2.51 (DMSO); 3.09 (g); 3.30 (h); 3.34 (H_2O); 3.43 (j); 3.51 (i); 5.03-5.06 (b); 7.31-7.56 (a); 7.64 (f).

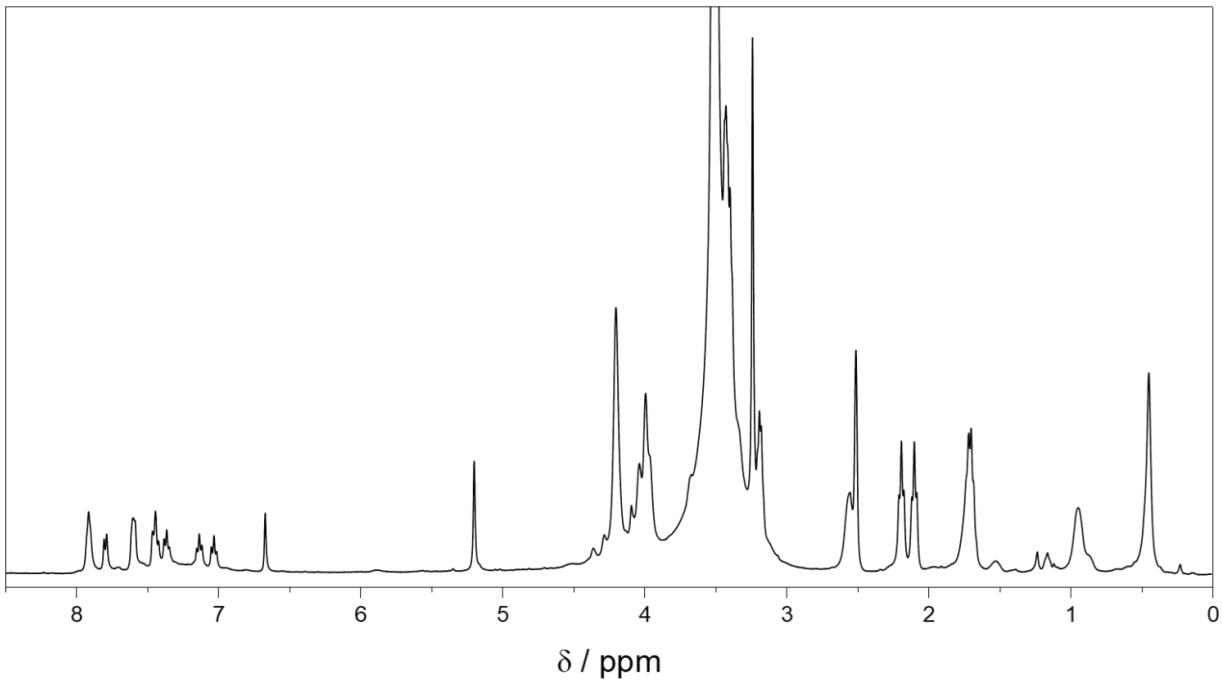

Figure 8.6. ^{1}H NMR spectrum of $PFS^{-}/_{N3\ (20\ \%)}$ + m-dPEG$_{12}$-DBCO click reaction mixture in DMSO-d6.

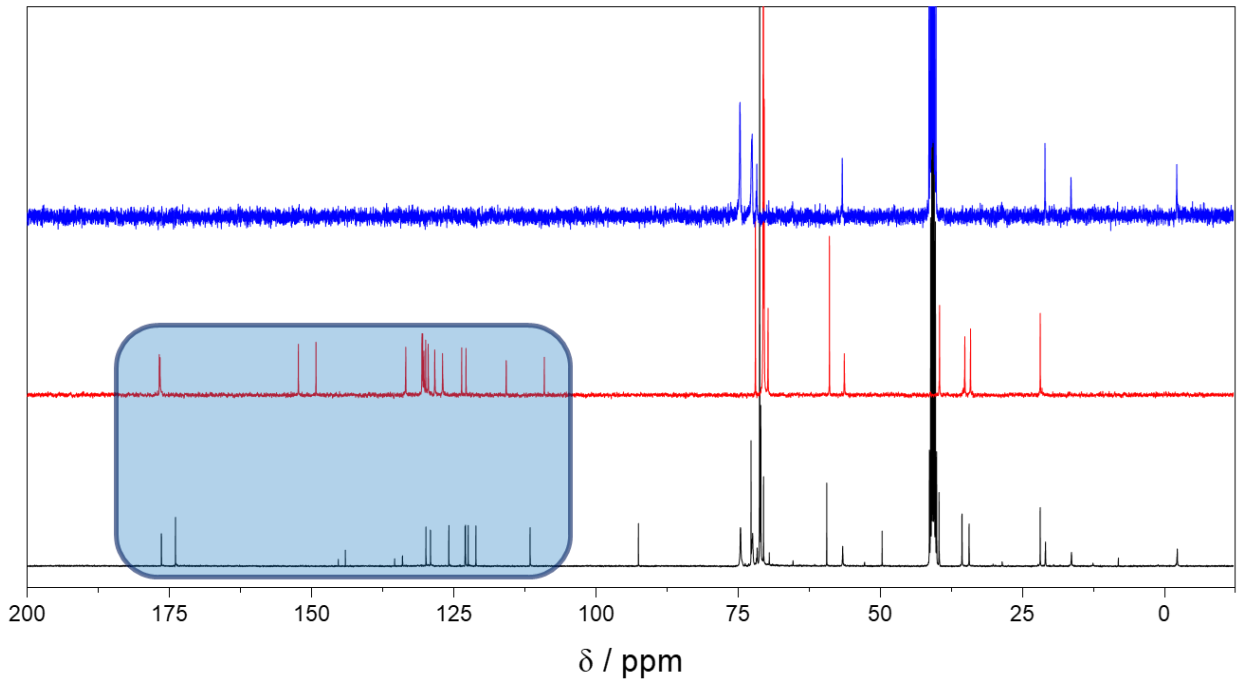

Figure 8.7. Comparison of 13C NMR spectra of reaction mixture ($PFS^{-}/N_{3\ (20\ \%)}$ + m-dPEG12-DBCO click reaction) (black), m-dPEG$_{12}$-DBCO (red) and $PFS^{-}/_{N3\ (20\ \%)}$ (blue) in DMSO-d6. The blue highlight indicates changes in alkene/aromatic region (100-180 ppm).

Buffer stability. In order to ascertain the feasibility of utilizing our model system for thrombin detection, it was necessary to characterize nanoparticle stability in the aptamer's activation buffer (see composition in Materials and Methods section of Chapter 3). As shown on Figure 8.8, the hydrodynamic radius has remained constant for over 4000 s in the case of both the PFS-AuNP and the aptamer-AuNPs, indicating that the system is stable in this buffer at the nanoparticle concentration used for other experiments (0.33 ppm or 1.67 μM Au).

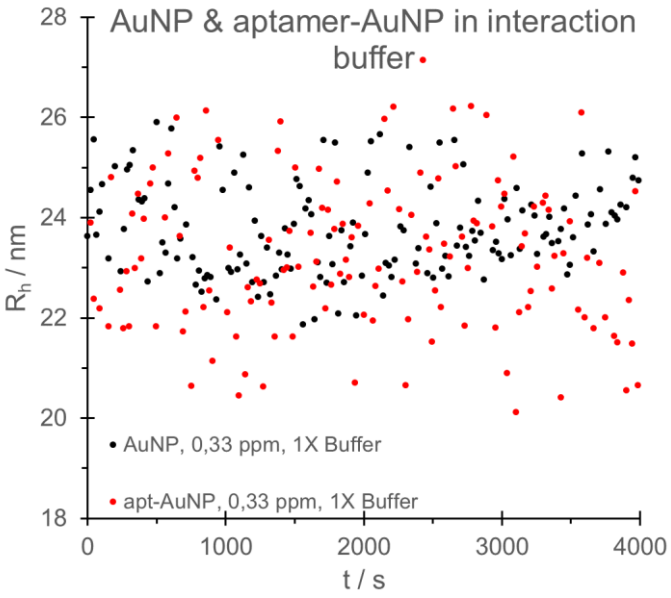

Figure 8.8. Stability of PFS-AuNPs (black) and aptamer-PFS-AuNPs (red) in 1 x interaction buffer. c_{Au} = 0.33 ppm (1.67 µM).

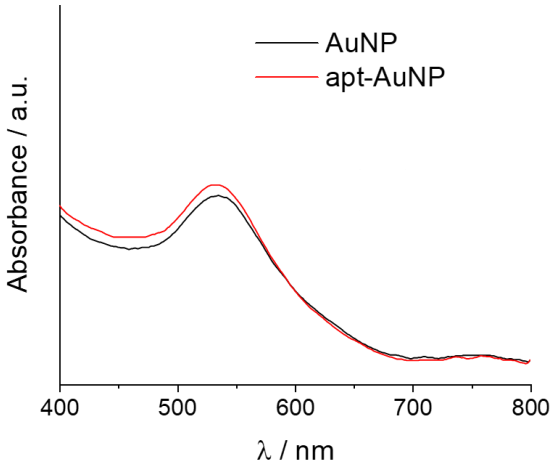

Figure 8.9. UV-vis spectra of gold nanoparticles before and after aptamer grafting. In both cases, c_{Au} = 40 µM in water.

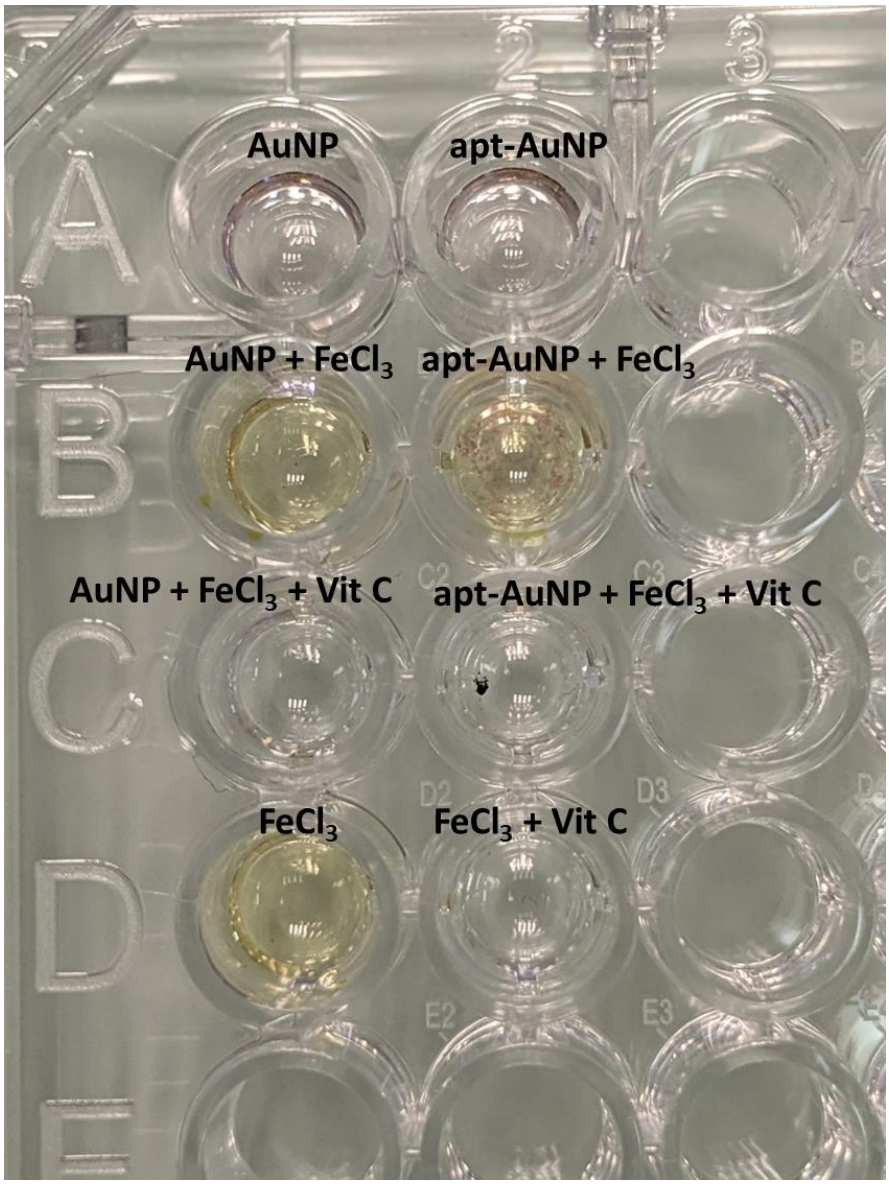

Figure 8.10. Photographs of different mixtures prepared for the redox activity tests.

9. Acknowledgements

I arrived in France on the summer of 2020 driven as much by curiosity and a wish for adventure as by an intention to learn and grow better as a scientist. I spent a wonderful three years there, even with the pandemic lockdowns and the complications of my doctoral studies. I learned the ins and outs of material chemistry of polymers, colloid science as well as a plethora of measurement and characterization methods that will aid me greatly during my future career. I also learned French, a language I previously considered completely impenetrable, but which turned out to be rather enjoyable to study.

My first supervisor, Professor **Corinne Nardin** helped me greatly in the process of settling into my new life in France. From finding accomodation to translating official documents – tax papers and even the COVID-19 lockdown orders –, she assisted me all through the duration of my stay in the country. Her aid during the months of "couvre-feu" that we had to endure was indispensable. I seriously doubt that I could have navigated the labyrinth of French life – and the paperwork! – if not for Professor Nardin's constant help and patience. I would like to thank Corinne for all she did for me and my professional advancement during the three years I spent in Pau.

I got to know Professor **G. Julius Vancso** a year before I moved to Pau, in 2019. I went to the Netherlands on an Erasmus+ scholarship for a single semester, with no great expectations. I came away with a paper ready to be published, a PhD offer in the pipeline, and friendships that formed in the lab with his students and which endure ever since. I would like to thank Julius for giving me this opportunity. His strict but fair guidance during my PhD (and during my stay in Twente before that) made me a better researcher. He taught me the importance of stringent control of all experimental results, and showed the difference between writing an article and writing a well-written one.

I should not omit Associate Professor **Mark A. Hempenius** from this list of acknowledgements either. He is a brilliant chemist, and most of what I know about experimental work with PFSs I learned from him.

I would also like to thank **Mohamed Amine Berkal**, with whom we worked together on the aptamer project, following protocols that he made and perfected. My other colleagues at UPPA, especially at IPREM, also helped me greatly with my research and I am grateful for that.

The Biocolloids Research Group at the University of Szeged also needs to be mentioned. Group leader Professor **Istvan Szilágyi** and his then-PhD student, now doctor **Nizar B. Alsharif** were instrumental in my research on colloidal stability as much with their detailed explanations on the subject as with their patient help with the experiments themselves.

Finally, I want to thank my family – **my mother, sisters, brothers-in-law**... – as well as my girlfriend, **Krisztina Anna Karádi** for their infinite patience and support during these three years.